



HAL
open science

Synthesis and design of optical nanoresonators for the visible wavelengths

Véronique Many

► **To cite this version:**

Véronique Many. Synthesis and design of optical nanoresonators for the visible wavelengths. Material chemistry. Université de Bordeaux, 2018. English. NNT : 2018BORD0325 . tel-02968585

HAL Id: tel-02968585

<https://theses.hal.science/tel-02968585>

Submitted on 16 Oct 2020

HAL is a multi-disciplinary open access archive for the deposit and dissemination of scientific research documents, whether they are published or not. The documents may come from teaching and research institutions in France or abroad, or from public or private research centers.

L'archive ouverte pluridisciplinaire **HAL**, est destinée au dépôt et à la diffusion de documents scientifiques de niveau recherche, publiés ou non, émanant des établissements d'enseignement et de recherche français ou étrangers, des laboratoires publics ou privés.

THÈSE PRÉSENTÉE
POUR OBTENIR LE GRADE DE
DOCTEUR DE
L'UNIVERSITÉ DE BORDEAUX

ÉCOLE DOCTORALE DES SCIENCES CHIMIQUES
SPÉCIALITÉ : Physico-Chimie de la Matière Condensée

Par Véronique MANY

**Synthesis and design of optical nanoresonators for
the visible wavelengths**

Soutenue le : 10 décembre 2018

Membres du jury :

Mme Alexa COURTY
M. Miguel CORREA-DUARTE
M. Benjamin ABECASSIS
M. Mario MAGLIONE
Mme Mona TREGUER
M. Serge RAVAINÉ
M. Etienne DUGUET

Professeur, Sorbonne Université
Professeur, Université de Vigo
Chargé de Recherche, CNRS
Directeur de recherche, CNRS
Professeur, Université de Bordeaux
Professeur, Université de Bordeaux
Professeur, Université de Bordeaux

Rapporteur
Rapporteur
Examineur
Président
Directeur de thèse
Directeur de thèse
Membre invité

To my beloved mom,

peryappa, ayya

and to you Madhav

Remerciements

Les travaux de thèse décrits dans ce manuscrit ont été réalisés à l'Institut de Chimie de la Matière Condensée de Bordeaux et au Centre de Recherche Paul Pascal, sous la direction de Mona Treguer-Delapierre, Etienne Duguet et Serge Ravaine. Je tiens à remercier en premier lieu Mario Maglione (ICMCB) et Cécile Zakri (CRPP) pour m'avoir accueillie au sein de ces deux laboratoires.

J'exprime toute ma gratitude à Alexa Courty et Miguel Correa-Duarte d'avoir accepté de rapporter cette thèse, ainsi qu'à Benjamin Abecassis pour avoir participé au jury de thèse et à Mario Maglione pour l'avoir présidé. Je les remercie sincèrement pour l'intérêt qu'ils ont manifesté envers ces travaux.

Je remercie très sincèrement mes directeurs de thèse Mona Treguer-Delapierre, Etienne Duguet et Serge Ravaine. Merci pour tout, notamment pour votre disponibilité malgré vos emplois du temps chargés, votre soutien, votre confiance, vos conseils et la liberté de travail que vous m'avez laissée pendant ces trois années. Je vous remercie aussi pour votre perfectionnisme et votre rigueur, qui au final, m'ont toujours poussée à aller de l'avant. Au final, oui, on peut toujours faire mieux (avec modération quand même).

Cette thèse, financée par le LabEx AMADEus, s'inscrit dans le cadre d'une étude sur les métamatériaux. Dans ce cadre, je remercie toutes les personnes avec qui j'ai eu l'opportunité de collaborer. Je remercie Philippe Richetti, Alexandre Baron et Romain Dézert pour leurs simulations qui m'ont été d'une grande aide tout au long de cette thèse. Merci à Philippe Barois pour m'avoir éclairée et fait partager ses connaissances notamment sur les mesures de SLS. Merci à Quentin pour toutes les mesures sur les matériaux fabriqués à partir des dodécapodes d'or. J'aimerais remercier, de manière générale, toute l'équipe pour votre partage de connaissance, votre disponibilité, votre motivation ainsi que pour votre accueil chaleureux. Je remercie aussi l'équipe du LOF, Sara de Cicco, Jean-Baptiste Salmon et Jacques Leng pour la fabrication des matériaux par voie microfluidique, pour votre investissement et votre motivation.

Dans le cadre de cette thèse, j'ai collaboré avec P. Torchio et Kékéli, de l'institut IM2NP pour des projets annexes concernant les cellules photovoltaïques. Je les remercie pour m'avoir offert l'opportunité de travailler dans leur projet et m'avoir fait découvrir leurs recherches. Bonne continuation Kékéli pour la suite.

Je remercie les membres du pôle de microscopie électronique de PLACAMAT, mais aussi Isabelle Ly, pour le microscope du CRPP ainsi que Theresa Hungria du Centre de MicroCaractérisation Raimond Castaing.

Merci aussi aux membres des services gestion, informatique, bibliothèque, service collectif et accueil, pour nous permettre d'avancer au quotidien au sein de l'ICMCB. Merci plus particulièrement à Sandrine, Stéphane, Carole, Alexandre F., Liva et Abder pour leur attention, leur convivialité et leur gentillesse à mon égard !

Merci aux stagiaires qui ont participé à ce projet : Fabien Soubie, Guillermo Siliezar, Jérémy Pargade, Runyu Liang, Arvind Mehra, Cécile Huez. Merci pour votre investissement,

votre motivation, et bon courage pour la suite de vos études ! Thanks to Vikas too, who was supervised by Philippe and Virginie in CRPP, thanks for your involvement and help for the project!

Je souhaite aussi remercier l'ensemble des membres du groupe 5. Les permanents : Stéphane, MHD, Graziella et Glenna. Un grand merci aussi à toi Lydia, pour toute ta gentillesse, ton sourire et ton soutien. Merci de m'avoir accueillie dans ton bureau pendant la rédaction de thèse, merci aussi pour toutes les commandes de produits que tu as passées pour moi.

Merci aussi aux anciens et nouveaux non permanents. Merci à toi Cyril, pour avoir été présent et m'avoir accueilli dans ce projet, à mon début de thèse. Merci à Weiya et Bai avec qui j'ai eu le plaisir de débiter cette thèse. I remember at the beginning of our PhD, you were so motivated to learn French and we use to write on the glass of the fume hood English and French words. Bai you are someone who is so funny and you use to take care of others, and I think I won't forget in my life: "C.K" and "coulis aux choix"... Merci à Noelia pour sa bonne humeur, thanks to Jiaji for all the discussions that we have together, your advice and jokes! Merci à ma Marie pour ta présence, ta positivité que tu transmets, pour ton écoute et ton attention et pour toutes nos discussions. Merci à ma petite Yasmine pour ton dynamisme, ta gentillesse et ta spontanéité! Je te souhaite de la réussite pour la suite, tu le mérites. Un grand merci à toi ma Elham pour toute ton attention, ton aide, pour nos discussions. Merci aussi pour le courage que tu m'as donnée et plus particulièrement en fin de thèse... Merci d'avoir été présente pour moi. Beaucoup de courage à toi pour cette 3^{ème} année ! Arnaud, c'était cool de t'avoir comme voisin de bureau, merci pour les discussions et surtout celles autour de la politique. J'admire la personne que tu es, et ton parcours aussi... au final, je ne t'ai jamais entendu te plaindre... Je te souhaite beaucoup de courage pour la suite et de la réussite aussi! Merci à Lucas Fourier, tu es un soleil et tu nous transmets ta bonne humeur. C'était un plaisir de travailler avec toi, bonne continuation !

Merci à tous : Sergio, Laurent Adumeau, Clément (contente d'avoir partagé le bureau avec toi), Samuel (un vrai plaisir de t'avoir rencontré, bon courage pour la suite), Hervé (vive les polym !! courage pour la dernière ligne droite !), Sanaa (ça a été un plaisir de partir en conf' avec toi ! Merci pour ton soutien et ta bonne humeur et ton rire qui résonne encore dans les murs de l'ICMCB), Abhi (my dear north indian friend), Maria (qui mange aussi lentement que moi!), Junjie, Fenghuan, Antoine, Maxime, Alexandre, Benoît Alexandra. Bon courage à Laurent L., qui prend la suite du projet et bon courage pour les nouveaux : Bin, Sharvina, et Lucas.

Je remercie également les membres des autres groupes notamment : Nicolas Penin, Nathalie D., Khawla, Liza, Juan, Marie C., Prashant, Issam, Marlène et Elodie T. pour leur convivialité et toute leur attention à mon égard.

Je souhaite remercier mes amies et plus particulièrement ma Sehr ou plutôt Docteur Sehr! Merci pour ta présence aussi bien dans mes bons et mauvais moments et de m'avoir toujours apporté tes précieux conseils. Ça a été un plaisir de partager cette expérience de thésarde avec toi, malgré la distance. Merci pour tout ton soutien, j'espère pouvoir être présente pour toi comme tu l'as été pour moi. Si tu n'avais pas été là, je ne sais pas si j'en serais vraiment arrivé là... Des fois certaines rencontres restent exceptionnelles. Tu as le cœur sur la main, reste celle que tu es. Merci aussi à ta sœur Hira pour faire le déplacement pour ma soutenance, merci pour ses cannelés !! Merci à ma Sandhu pour ces messages son attention malgré son emploi du temps chargé avec ses deux petits. Merci pour ta présence dans mes bons et

mauvais moments. Merci à ma Zahra. C'était un plaisir de te voir ici en stage, merci pour toutes nos sorties et merci de venir pour la soutenance ! Merci à Dihia, pour ton ouverture d'esprit, nos discussions et ton attention. C'était un plaisir de te voir à Bordeaux! Merci à Anitha, pour toutes ces années d'amitié, nos sorties et nos crêpes au nutella me manquent !

Pour finir, je souhaite remercier toute ma famille. Un grand merci à ma maman. La vie n'a pas été simple pour toi, et malgré les difficultés, tu as toujours fait de ton mieux pour tes enfants, tu as toujours pensé à nous et fait ton maximum pour nous rendre heureux... Merci pour tout maman et cette réussite je te la dédie, tu la mérites largement, alors bravo à toi! Merci à mon père. Tu m'as beaucoup challengée dans ma vie... Ça n'a pas toujours été facile... Toi et maman vous êtes parti de rien quand vous êtes venu en France, mais vous vous êtes accroché à vos ambitions, vous avez travaillé sans relâche et vos parcours reste exemplaire. Peut être que dans le fond, cette motivation et cette volonté de vouloir aller de l'avant malgré toutes les difficultés je la tiens de vous... Alors merci. I would like to thank my dear peryappa. Life is not fair, and I am still missing you a lot... You left too early... Thanks for all the happiness that you bring to me, thanks for all the discussions that we have together, thanks to stand for me. I hope that you are proud of me today... A big thank to my ayya, I hope that I can be as strong as you were in your life. I am so proud of you... Your house (the old one) will remain the happiest place for me.

Merci à ma sœur Sabine pour ton soutien, notamment pendant la rédaction et la préparation pour l'oral et merci à ma petite Jaïna, qui grandit beaucoup trop vite. Ton sourire me fait oublier tout mes soucis mon petit bébé. Thanks to my brother Vinod, thanks for your support, and for your advices. Once you told me: "don't be like others, do what you really want to do, go ahead, don't listen people who are discouraging you". Even now, those words remain so precious for me... and really thank you brother. Merci à ma cousine, ma sœur et mon amie Christina. Tu m'as été d'un grand soutien, tu as toujours fait preuve d'une grande attention et je t'en suis reconnaissante ! Nos séances cinéma et Mcdo me manquent....

Finally, I would like to thank you my dear Madhav to be my family, my best friend and my best confidant. Those last four years were full of ups and downs for us... and thank you to stand for me whatever the situation, thanks for your unconditional love and support, thanks to be my best support in life.

Résumé en français

L'étude et la réalisation de métamatériaux auto-assemblés possédant une réponse magnétique aux fréquences optiques font l'objet d'un champ de recherche très actif depuis plusieurs années. Les matériaux ayant une perméabilité magnétique et une permittivité négative sont des matériaux non conventionnels et inconnus dans la nature. Des études théoriques et expérimentales ont démontré la possibilité de générer une réponse magnétique, par des surfaces métalliques nanostructurées de types « fishnet » élaborées par lithographie [1-2]. Ces études ont démontré qu'une réponse magnétique peut être générée dans l'infrarouge ainsi qu'un indice de réfraction négatif.

La fabrication de métamatériaux actifs aux longueurs d'onde du visible représente un réel challenge. La taille de ces nanorésonateurs doit être inférieure à la longueur d'onde considérée et donc être dans la gamme 100-200 nm. La méthode « top-down » permet la conception de microrésonateurs ayant des réponses actives dans l'infrarouge [3-6]. Cependant, cette méthode ne permet pas ni un contrôle fin de la forme et de la taille des résonateurs, ni une réponse optique isotrope. Pour palier à ces inconvénients, la méthode « bottom-up » s'avère être plus pertinente.

De nombreuses études ont démontré que les nanorésonateurs de type « framboises », basés sur l'utilisation de nanoparticules d'or ou d'argent disposées autour d'un noyau central diélectrique, permettent un couplage plasmonique générant un magnétisme artificiel [7]. Par ailleurs, il a été démontré qu'un nano-objet ayant un cœur de silice de 100 nm décoré de 12 nanoparticules d'or sphériques de 80 nm permettrait d'optimiser le phénomène de magnétisme optique [8]. Ma thèse repose sur l'élaboration de ces objets à partir de particules constituées d'un cœur de silice et 12 nodules de polystyrène (Schéma 1).

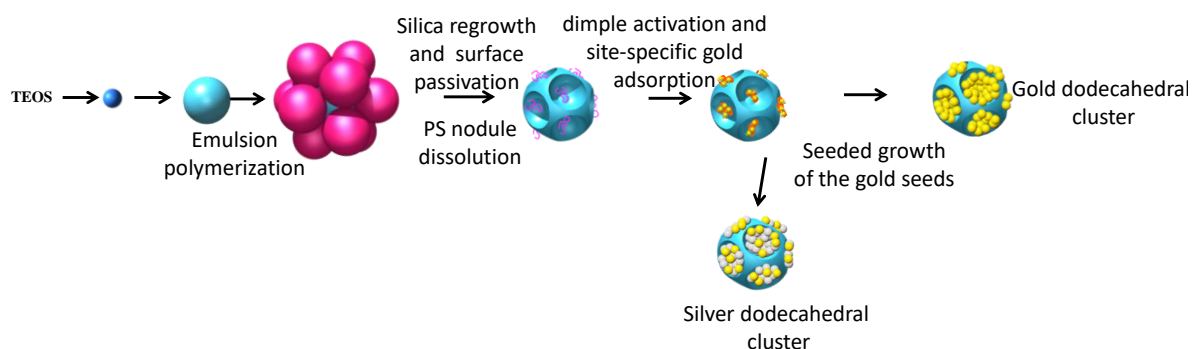


Schéma 1 : Stratégie adoptée pour l'élaboration de nanorésonateurs : (i) synthèse des particules de silice à fossettes, (ii) synthèse de clusters dodécédrique d'or (iii) synthèse de clusters dodécédrique d'argent.

Dans un premier temps, nous avons revisité les étapes successives suivantes : (i) la synthèse de particules de silice de taille contrôlée, (ii) la polymérisation ensemencée en émulsion du styrène pour élaborer des dodécapodes de type polystyrène/silice, (iii) la recroissance du cœur de silice et la dissolution des nodules de polystyrène, (iv) la fonctionnalisation des résidus de polystyrène de manière à les rendre « collants » pour des germes d'or de 2-3 nm [9-12]. Nous avons mis en évidence la répétabilité et la reproductibilité de la synthèse des dodécapodes polystyrène/silice avec un rendement morphologique de 50%, mais aussi la présence de satellites de polystyrène polydisperses en taille. Nous avons étudié l'influence de différents paramètres : la proportion tensioactif/co-tensioactif, la concentration totale en tensioactifs, et la concentration en styrène. En augmentant le nombre de nuclei de polystyrène à la surface de la silice, nous avons augmenté le rendement en morphologie des dodécapodes à 75 %. Cependant, lors de la préparation de ces lots de dodécapodes, certains sous-produits persistent notamment : (i) des multipodes contenant plusieurs cœurs de silice pouvant provenir de la déstabilisation des germes de silice ; (ii) des clusters avec moins de 12 satellites de polystyrène résultant d'une distribution trop large du nombre initial de nuclei ou de phénomènes de coalescence intersatellite inopinés. Ainsi pour porter le rendement morphologique en dodécapodes au-delà de 75 %, des étapes de purification, par exemple par centrifugation en gradient de densité, pourraient être envisagées.

[Silica seeds] L ⁻¹	7.3x10 ¹⁵	7.3x10 ¹⁵	7.3x10 ¹⁵
[Styrene] g/L	45	45	45
[Surfactant] g/L	3	3	4
NP30/SDS mass ratio	95/5	93/7	93/7
Monomer-to-polymer conversion (%)	89	85	80
R _v [∞]	14.4	13.7	12.9
R _v ^{∞ local}	12.2	13.5	11.2
% Hexapods	3	6	
% Octopods	9	19	3
% Nonapods	10	12	6
% Decapods	12		6
% Hendecapods	4		
% Dodécapods	50	58	75
% Multi-silica clusters	11	6	10

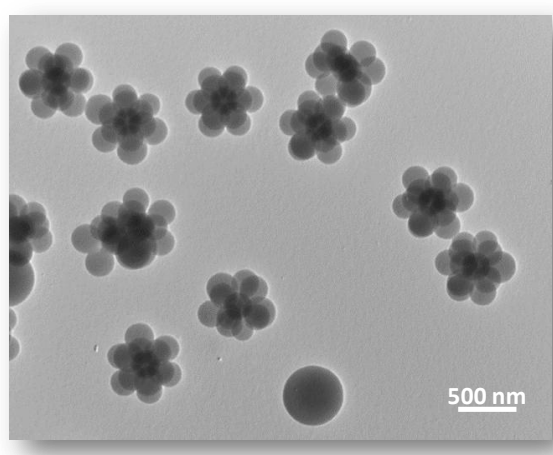
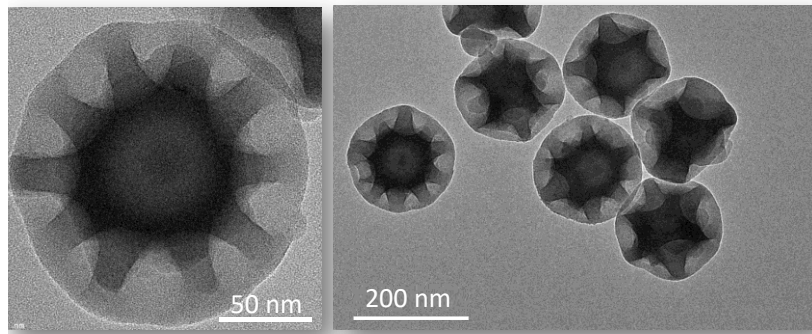


Figure 1: Tableau récapitulatif des conditions expérimentales et paramètres utilisés lors de l'étude de l'influence de la proportion de tensioactif/co-tensioactif SDS/NP30 et de la concentration totale en tensioactifs sur le rendement morphologique en dodécapodes polystyrène/silice ; Image de microscopie électronique à transmission du lot riche à 75 % en dodécapodes.

Ces nodules de PS pouvant être éliminés ultérieurement par dissolution dans le tétrahydrofurane, ces objets ont permis de générer de grandes quantités de particules de silice

décorées d'un nombre précis de « patches », appelés ici « fossettes » (Figure 2). Ces particules ont été utilisées pour élaborer des clusters dodécaédriques plasmoniques.



Diametre total (nm)	175
Profondeur des fossettes (nm)	43
Diamètre externe des fossettes (nm)	81
Pureté en particules à 12 fossettes (%)	75

Figure 2: Clichés de microscopie électronique des particules de silice à 12 fossettes; tableaux récapitulatifs des dimensions des particules à 12 fossettes.

Dans un deuxième temps, nous avons revisité par croissance ensemencée des germes d'or permettant la synthèse des clusters dodécaédriques dorés. Chaque étape de la synthèse a été optimisée, ce qui a permis de contrôler de manière précise la taille des satellites d'or ainsi que la distance entre ces satellites (Figure 3). Lors de la croissance des germes d'or, des phénomènes de dissolution du cœur de silice ont eu avoir lieu. Ce phénomène de dissolution s'est avéré dépendant de l'âge de la solution de précurseurs d'or : plus la solution est âgée, moins la silice est attaquée. Ce phénomène de dissolution semble provenir de l'absorption des contre-ions présents dans la solution de précurseurs d'or.

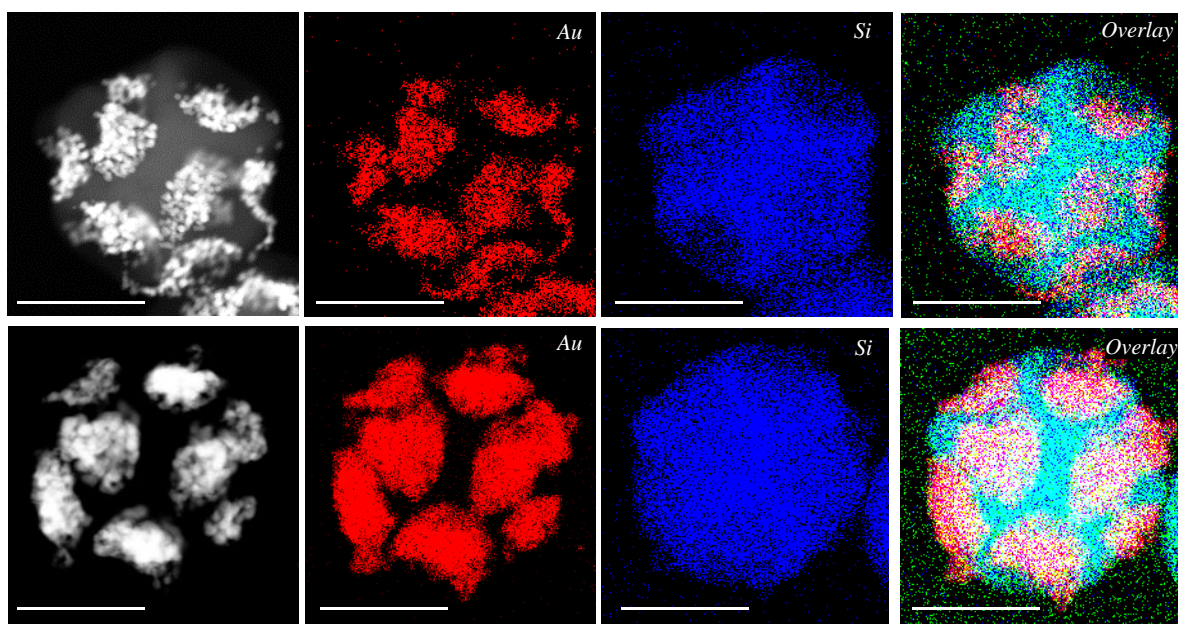


Figure 3: Clichés de microscopie électronique à balayage et cartographies EDS de clusters dodécaédrique dorés obtenus en utilisant 0.2 and 0.9 mM de solution de précurseurs d'or. Barre d'échelle : 100 nm

Chaque satellite est constitué de nanoparticules d'or de quelques nanomètres de diamètre agglomérés. Pour pouvoir densifier ces agrégats d'or, nous avons procédé à un traitement thermique (Figure 4).

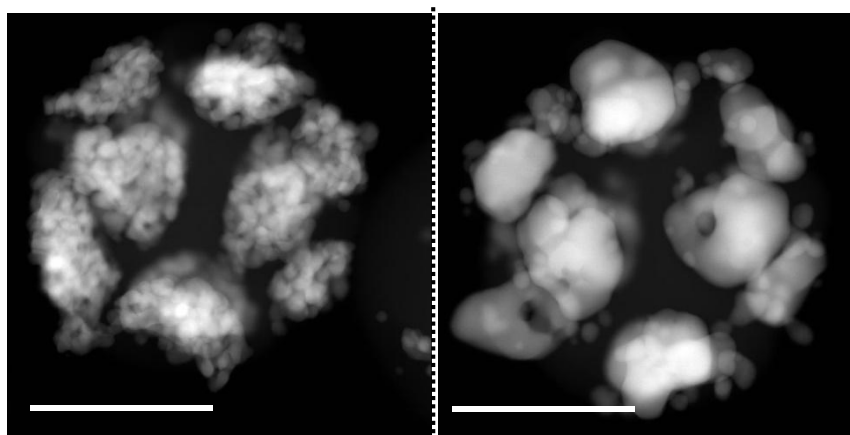


Figure 4: Clichés de microscopie électronique à balayage avant (gauche) et après (droite) le procédé de densification des clusters dodécaédriques dorés. Barres d'échelle : 100 nm.

Les propriétés optiques de ces objets ont été mesurées. Nous avons démontré qu'elles pouvaient être modulées en fonction de la taille des satellites, et la distance entre ceux-ci. Ces clusters basés sur le modèle des particules de type « framboises », proposée par Simovski possèdent une réponse magnétique et isotrope [13-15]. Les mesures de propriétés optiques de ces clusters dodécaédriques dorés ont mis en évidence une réponse optique plus intense que celle des particules de type « framboises » ayant des nanoparticules d'or distribuée de manière

aléatoire autour d'un cœur de silice (Figure 5). Nous avons aussi démontré la possibilité de moduler cette réponse optique en fonction du taux de densification des agrégats d'or au niveau des fossettes.

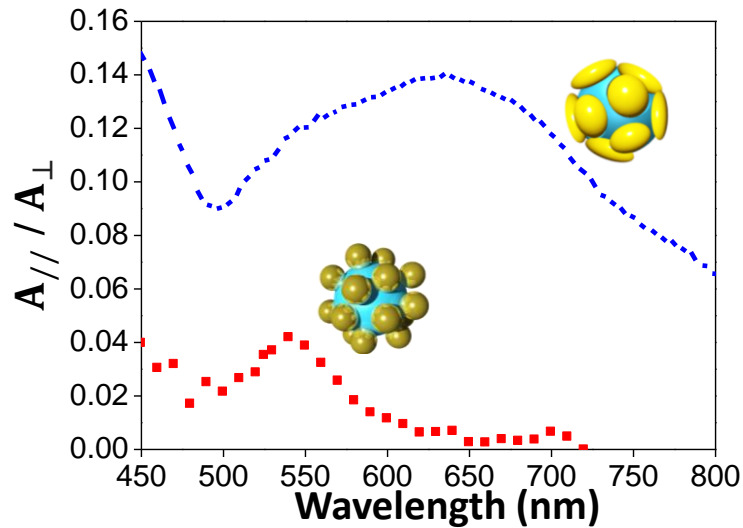


Figure 5: Comparaison des propriétés optiques de framboises plasmoniques (spectre rouge) et de clusters dodécaédriques d'or (spectre bleu) [16].

Nous avons développé une stratégie permettant de faire croître de l'argent à la surface de petits germes d'or ancrés au fond des fossettes. Cette méthode permet de moduler la composition or/argent des satellites en ajustant la concentration des clusters dodécaédriques d'or par rapport à la concentration en précurseurs d'argent (Figure 6).

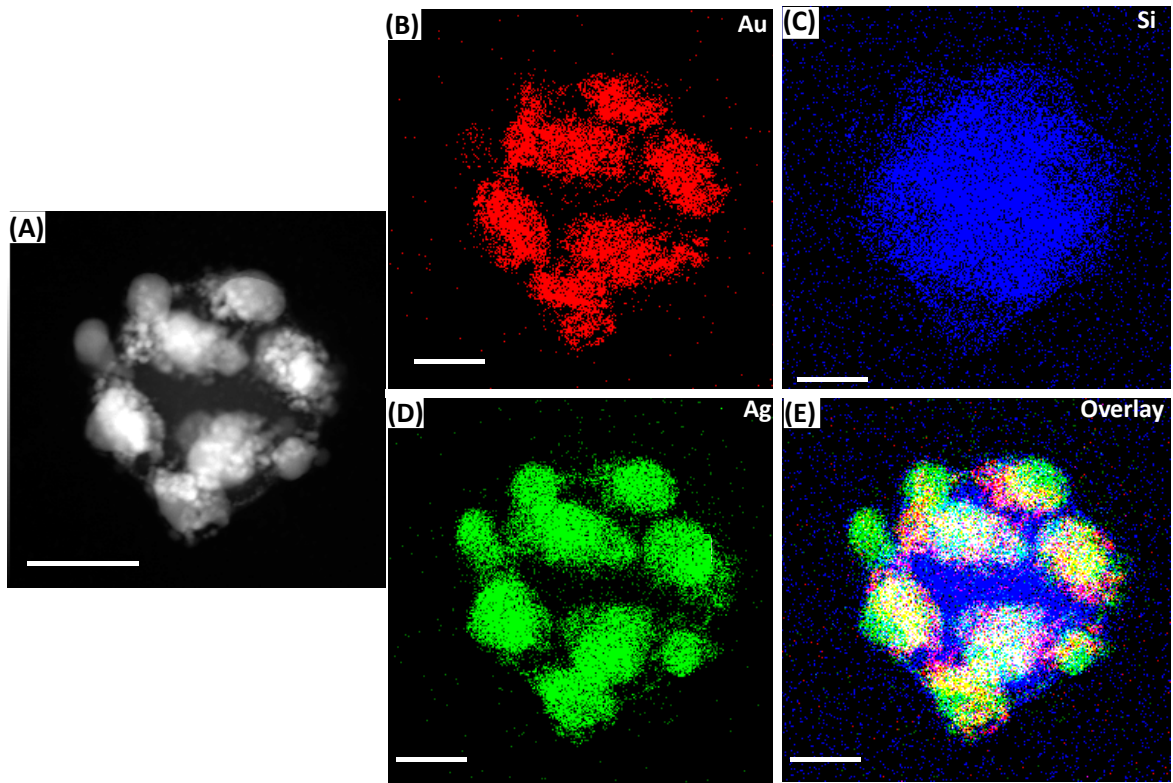


Figure 6: Clichés de microscopie électronique à balayage et cartographies EDS des clusters dodécaédriques Au/Ag 50/50. Barres d'échelle : 100 nm.

Les modes magnétiques optiques des nanoclusters AuAg sont encore plus intenses que ceux observés pour les systèmes à base d'or (Figure 7).

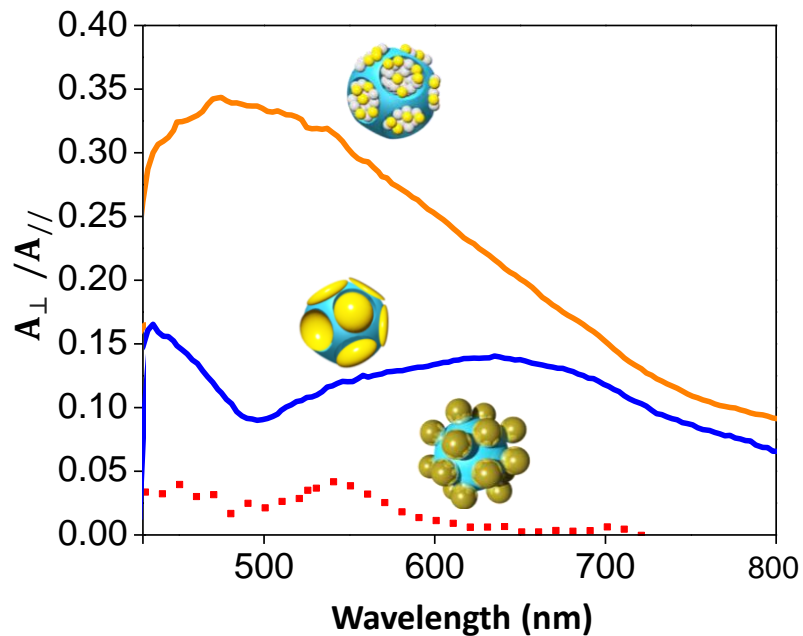


Figure 7: Comparaison des spectres de diffusion des framboises ayant des satellites d'or (spectre rouge) [16]; des clusters dodécaédriques d'or (spectre bleu) ; des spectres clusters dodécaédriques or/argent (spectre orange).

Les voies de synthèse de type « bottom-up » des nanorésonateurs permettent la fabrication en grande quantité de clusters dodécaédriques dorés et ouvrent ainsi la voie pour la fabrication de métamatériaux 2D et 3D.

Pour fabriquer une surface 2D, nous avons employé la méthode de dépôt par « dip-coating ». Nous avons étudié l'influence de paramètres tels que la concentration en suspension de clusters, la nature du solvant, la vitesse de retrait du substrat et la température sur l'épaisseur du film de clusters déposée sur le substrat. Ces expériences ont permis la fabrication d'une monocouche de clusters dodécaédriques dorés (Figure 8).

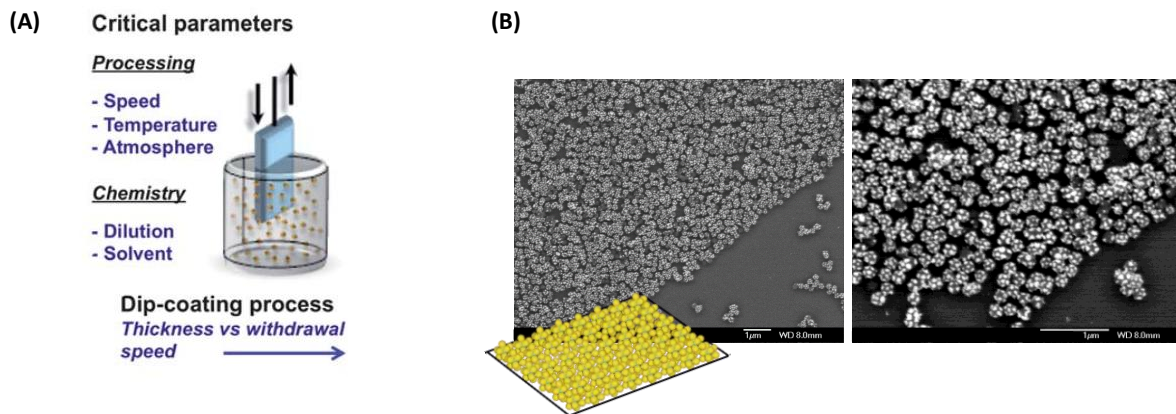


Figure 8: (A) Principe de dépôt par « dip-coating » [17]; (B) Clichés MEB de la surface de clusters à base d'or.

La méthode de microfluidique par évaporation a permis la fabrication d'un matériaux 3D suffisamment dense et épais pour permettre des mesures optiques par ellipsométrie spectroscopique de manière à déterminer l'indice de réfraction de celui-ci (Figure 9).

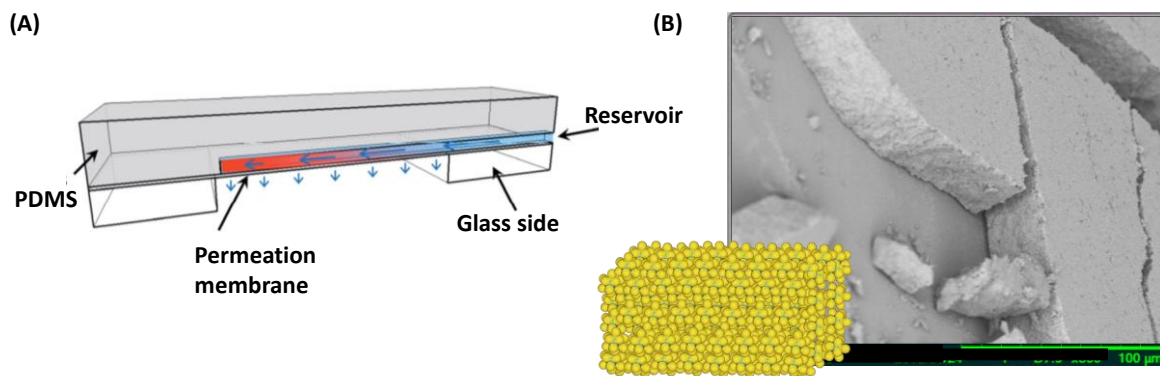


Figure 9: (A) Principe de la microfluidique par évaporation; (B) Image de microscopie à balayage d'un assemblage 3D de clusters dodécaédriques d'or.

Références

- [1] J. B. Pendry, A. J. Holden, D. J. Robbins et W. J. Stewart, "Magnetism from conductors and enhanced nonlinear phenomena," *IEEE Trans. Microw. Theory Tech.*, vol. 47, pp. 2075–2084, 1999.

- [2] R. A. Shelby, D. R. Smith et S. Schultz, “Experimental Verification of a Negative Index of Refraction,” *Science*, vol. 292, pp. 77 – 79, 2001.
- [3] V. M. Shalaev, W. Cai, U. K. Chettiar, H.-K. Yuan, A. K. Sarychev, V. P. Drachev et A. V. Kildishev, “Negative index of refraction in optical metamaterials,” *Opt. Lett.*, vol. 30, pp. 3356–3358, 2005.
- [4] N. Liu, H. Guo, L. Fu, S. Kaiser, H. Schweizer et H. Giessen, “Three-dimensional photonic metamaterials at optical frequencies,” *Nat. Mater.*, vol. 7, p. 31, 2007.
- [5] C. Enkrich, F. Pérez-Willard, D. Gerthsen, J. F. Zhou, T. Koschny, C. M. Soukoulis, M. Wegener et S. Linden, “Focused-Ion-Beam Nanofabrication of Near-Infrared Magnetic Metamaterials,” *Adv. Mater.*, vol. 17, pp. 2547–2549, 2005.
- [6] J. Valentine, S. Zhang, T. Zentgraf, E. Ulin-Avila, D. A. Genov, G. Bartal et X. Zhang, “Three-dimensional optical metamaterial with a negative refractive index,” *Nature*, vol. 455, p. 376, 2008.
- [7] A. Vallecchi, M. Albani et F. Capolino, “Collective electric and magnetic plasmonic resonances in spherical nanoclusters,” *Opt. Express*, vol. 19, pp. 2754–2772, 2011.
- [8] V. Many, R. Dézert, E. Duguet, A. Baron, V. Jangid, V. Ponsinet, S. Ravaine, P. Richetti, P. Barois et M. Tréguer-Delapierre, “High optical magnetism of dodecahedral plasmonic meta-atoms,” *Nanophotonics*, doi:10.1515/nanoph-2018-0175, 2018.
- [9] A. Désert, I. Chaduc, S. Fouilloux, J.-C. Taveau, O. Lambert, M. Lansalot, E. Bourgeat-Lami, A. Thill, O. Spalla, S. Ravaine et E. Duguet, “High-yield preparation of polystyrene/silica clusters of controlled morphology,” *Polym. Chem.*, vol. 3, pp. 1130–1132, 2012.
- [10] C. Chomette, M. Tréguer-Delapierre, N. B. Schade, V. N. Manoharan, O. Lambert, J.-C. Taveau, S. Ravaine et E. Duguet, “Colloidal Alchemy: Conversion of Polystyrene Nanoclusters into Gold,” *ChemNanoMat*, vol. 3, pp. 160–163, 2017.
- [11] C. Chomette, “Thèse de l’université de Bordeaux: Design and synthesis of plasmonic meta-atoms from patchy particles,” 2015.
- [12] A. Désert, “Thèse de l’Université Bordeaux 1: Colloïdes hybrides silice/polystyrène de morphologie contrôlée,” 2011.
- [13] A. Alù, A. Salandrino et N. Engheta, “Negative effective permeability and left-handed materials at optical frequencies,” *Opt. Express*, vol. 14, pp. 1557–1567, 2006.
- [14] C. R. Simovski et S. A. Tretyakov, “Model of isotropic resonant magnetism in the visible range based on core-shell clusters,” *Phys. Rev. B - Condens. Matter Mater. Phys.*, vol. 79, pp. 1–9, 2009.
- [15] C. Simovski et D. Morits, “Isotropic negative refractive index at near infrared,” *J. Opt.*, vol. 14, p. 125102, 2012.
- [16] V. Ponsinet, P. Barois, S. M. Gali, P. Richetti, J. B. Salmon, A. Vallecchi, M. Albani, A. Le Beulze, S. Gomez-Grana, E. Duguet, S. Mornet et M. Treguer-Delapierre, “Resonant isotropic optical magnetism of plasmonic nanoclusters in visible light,” *Phys. Rev. B*, vol. 92, p. 220414, 2015.
- [17] D. Grosso, “How to exploit the full potential of the dip-coating process to better control film formation,” *J. Mater. Chem.*, vol. 21, pp. 17033–17038, 2011.

Outline

General introduction	1
References	2
Chap I : State-of-the-art and objectives	5
1. Metamaterial concept	7
1.1 Brief history	8
1.2 Applications	10
1.3 Bottom-up vs. top-down fabrication routes.....	11
2. Raspberry-like nanoparticles as nano-sized split-ring resonators.....	12
2.1 Theoretical investigations	12
2.2 Synthesis, optical characterization, and assembly into materials.....	12
2.2.1 Synthesis approach and optical investigations.....	12
2.2.1.1 Self-assembly of small plasmonic particles on a dielectric core	13
2.2.1.2 Self-assembly of larger plasmonic particles on a dielectric core	13
2.2.1.3 Seeded-growth of metal satellites on a dielectric core.....	15
2.2.2 Material fabricated from raspberry-like sub-units and evidence of the refractive index of the material	17
3. Plasmonic dodecahedral cluster as a new challenging design.....	18
3.1 Theoretical investigations of raspberry like nanoparticles vs. dodecahedral clusters .	18
3.2 How to adjust to 12 the number of satellites on a dielectric core?.....	20
3.2.1 Virus templating.....	20
3.2.2 Controlled aggregation	21
3.2.3 Templating with colloidal crystals?	22
3.2.4 DNA origami as a scaffold	24
3.2.5 Using dimpled-silica particles as a scaffold	26
4. Conclusion and strategy	28
5. References	29
Chapter II : Synthesis of functional dodecahedral-dimpled silica nanoparticles from PS/silica dodecapods.....	35
Introduction	37
1. Stage I: Synthesis of size-monodisperse silica seeds.....	38
2. Stage II: Synthesis of PS/silica dodecapods by seeded-growth emulsion polymerization	42
2.1 Description of the reference experiment of Désert <i>et al.</i>	42
2.2 The Thill's model to rationalize the nucleation and growth of PS nodules onto silica seeds	43

2.3 Robustness of the dodecapods synthesis	45
2.4 Influence of the surfactant mixture composition and proportion with regard to the monomer	48
2.4.1 Influence of the SDS fraction.....	49
2.4.2 Influence of the total concentration of surfactant	49
2.4.3 Influence of the sonication protocol of the silica seed dispersion	50
2.4.4 Influence of the styrene initial concentration	53
3. Stage III: Derivatization of the PS/silica dodecapods into DDS clusters	55
3.1 Template regrowth of the silica cores.....	55
3.2 Passivation of the silica core	55
3.3 Dissolution of the PS nodules	56
4. Stage IV: Chemical modification of the PS residue at the bottom of the dimples	57
4.1 Chloromethylation of the PS residue	58
4.2 Amination of the chloromethylated PS residue.....	59
5. Conclusion	60
6. References	61
Chapter III : Synthesis of gold dodecahedral clusters and optical investigations.....	65
1. Stage V: Seeded growth of gold seeds on aminated PS chains	68
1.1 Synthesis of the gold seeds	68
1.2 Adsorption of gold seeds on the aminated PS chains	69
1.3 Growth of the gold satellites from the attached seeds	70
1.3.1 Principle of the seeded-growth method.....	70
1.3.1.1. Influence of the pH of the reaction medium.....	72
1.3.1.2 Influence of the gold precursor age to the seeded growth of the gold seeds .	73
1.3.2 Investigation of the DDS clusters concentration.....	74
1.3.3 Investigation of the gold precursor concentration on the synthesis of GDC	75
1.3.4 Characteristics of the GDC after the seeded-growth of gold particles.....	78
2. Stage VI: densification of the gold satellites of the GDC clusters	80
2.1 Investigation of the thermal annealing on the densification of the satellites.....	80
2.2 Characteristics of the GDC after densification	82
2.3 Extension of the densification for GDC with increasing satellites size	83
3. Stage VII: investigation of the magnetic and electric responses of the GDC by static light scattering	84
3.1 Static light scattering principle	84
3.2 Influence of the satellites size of GDC and their densification in their scattering properties	86

3.3. Numerical investigations	88
3.3.1 Numerical investigations of the GDC before densification.....	88
3.3.2 Numerical investigations of the GDC after densification	89
4. Conclusion	90
5. References	91
Chapter IV : Extension to silver dodecahedral clusters.....	95
1. Stage VIII: Direct silver growth from tiny gold seeds adsorbed within the dimples of the dodecahedral clusters	98
2. Stage IX: Silver growth from tiny gold seeds adsorbed within the dimples of the dodecahedral clusters after a preliminary growth of gold.....	99
3. Stage X: Control of the composition of the silver-gold satellites.....	102
4. Investigation of the magnetic and electric responses of the silver dodecahedral clusters from static light scattering.....	105
Conclusion.....	106
References	107
Conclusions and future work	108
References	113

List of abbreviations

CPMV	cowpea mosaic virus
DDS	dodecahedral dimpled-silica
DLVO	Derjaguin-Landau-Vervey-Overbeek
DMF	dimethylformamide
DNG	double negative
DPS	double positive
ED	electric dipole
EDPS	N-[3-(trimethoxysilyl)propyl]-ethylenediamine
EDX	energy-dispersive X-ray spectroscopy
ENG	ϵ negative media
ENZ	ϵ near zero media
FEM	finite element method
GDC	gold dodecahedral clusters
GMM	generalized multi-particle Mie
GPS	gold plating solution
IR	infra-red
MD	magnetic dipole
MMS	methacryloxymethyltriethoxysilane
MQ	quadrupolar modes
NP	nanoparticle
PDDA	polydiallyldimethylammonium
PDI	polydispersity index
PNIPAM	poly(N-isopropylacrylamide)
PS	polystyrene
PS-PAA	polystyrene- <i>block</i> -poly(acrylic acid)
PSS	poly(sodium 4-styrenesulfonate chloride)
PVMe ⁺ I	poly(1-vinyl-4-methyl-1,2,4-triazolium iodide)
PVP	polyvinylpyrrolidone
SDS	sodium dodecyl sulfate
NP 30	polyethylene glycol nonylphenyl ether
SDC	silver dodecahedral clusters
SLS	static light scattering
SRR	split-ring resonators
STEM	scanning transmission electron microscopy
TEM	transmission electron microscopy
TEOS	tetraethoxysilane
THF	tetrahydrofuran
ZIM	zero index media

General introduction

Metamaterials are unconventional materials which are made of artificial sub-units called resonators or meta-atoms. They generate fascinating optical properties such as artificial magnetism. Materials which have both negative magnetic permeability and dielectric permittivity are called double negative materials and do not exist in Nature. Thus, research in such a topic have considerably grown in the past few years.

Pendry *et al.* theoretically reported for the first time the possibility to generate a magnetic response from a split-ring resonators (SRR) [1]. This device was made of a concentric and incomplete loops of metal embedded in a dielectric, with a size smaller than the considered wavelength. A strong coupling is generated between the incident electromagnetic wave and the circulating current modes. Shelby *et al.* confirmed experimentally this theory fabricating two-dimensional arrays of copper SRR.[2] They demonstrated that such devices can have both negative permeability and permittivity in the microwave regime yielding to a negative refractive index at microwave frequencies.

The fabrication of a metamaterial active in the visible range is particularly challenging and promising to revolutionize optics. The resonators should have a specific shape and the size has to be lower than the considered wavelength, *i.e.* in the 100-200 nm size range. Top down methods were reported to fabricate two-dimensional, *i.e.* anisotropic, microresonators therefore restricted to the IR range [3-6]. For nanosized resonators, bottom-up approaches are a good alternative that can pave the way to engineer finely the meta-atoms shape and size and can allow the fabrication of a 3D material by (self-)assembly.

Among the meta-atoms that have been reported so far, the metallodielectric nanoresonators called “raspberry-like” nanoparticles received a specific attention. They are made of a central dielectric core surrounded with plasmonic nanoparticles whose size and in-between gap are supposed to be finely tuned. This particular design allows a plasmonic coupling between the satellites leading to a circulating current around the dielectric core, which generates a magnetic resonance orthogonally to the incident electric field and the electric resonance [7].

Several approaches were reported to synthesize raspberry-like nanoparticles by self-assembly approach [8,9] or seeded growth of silver or gold nuclei on the dielectric core

[10,11]. Those experimental studies reported the occurrence of the magnetic response of such clusters in the visible wavelength.

The goal of the present work was to optimize the isotropic magnetic optical response of metallodielectric nanoresonators in the visible range, by specifically controlling the number, the size and the in-between gap of the satellites. Previous studies already reported the importance of controlling such parameters on the generation of the magnetic response [12,13]. Simulations of the optical properties of clusters made of a silica core and a precise number of gold satellites were performed at the Centre de Recherche Paul Pascal. The influence of the number of the gold satellites, keeping constant their volume and the silica core size was investigated. It appears that gold dodecahedral clusters made of a silica core of 100 nm and twelve gold satellites of 80 nm with an in-between satellites gap of 2 nm are the most promising candidates with regard to the maximization of the magnetic response.

Thus, inspired by previous works performed at the university of Bordeaux [14-17], we focus our work on the synthesis of functional dodecahedral-dimpled silica (DDS) nanoparticles to serve as a scaffold to synthesize discrete and isotropic dodecahedral clusters made of twelve gold or silver satellites.

The first chapter presents the state-of-the-art of the subject summarizing the different approaches of metallodielectric nanoresonators synthesis and the optical investigations of their electromagnetic properties. At the end of this chapter, the strategy of the present work is fully developed and justified. The second chapter reports the synthesis of functional dodecahedral-dimpled silica nanoparticles from PS/silica dodecapods in high yield and quantity. The third and fourth chapters describe the synthesis of gold and silver dodecahedral clusters by a seeded-mediated growth approach and the study of their optical properties.

References

- [1] J. B. Pendry, A. J. Holden, D. J. Robbins, and W. J. Stewart, "Magnetism from conductors and enhanced nonlinear phenomena," *IEEE Trans. Microw. Theory Tech.*, vol. 47, no. 11, pp. 2075–2084, 1999.
- [2] R. A. Shelby, D. R. Smith, and S. Schultz, "Experimental Verification of a Negative Index of Refraction," *Science*, vol. 292, no. 5514, pp. 77 – 79, 2001.
- [3] V. M. Shalaev, W. Cai, U. K. Chettiar, H.-K. Yuan, A. K. Sarychev, V. P. Drachev, and A. V. Kildishev, "Negative index of refraction in optical metamaterials," *Opt. Lett.*, vol. 30, no. 24, pp. 3356–3358, 2005.
- [4] N. Liu, H. Guo, L. Fu, S. Kaiser, H. Schweizer, and H. Giessen, "Three-dimensional photonic metamaterials at optical frequencies," *Nat. Mater.*, vol. 7, p. 31, 2007.
- [5] C. Enkrich, F. Pérez-Willard, D. Gerthsen, J. F. Zhou, T. Koschny, C. M. Soukoulis, M. Wegener, and S. Linden, "Focused-Ion-Beam Nanofabrication of Near-Infrared Magnetic

- Metamaterials,” *Adv. Mater.*, vol. 17, no. 21, pp. 2547–2549, 2005.
- [6] J. Valentine, S. Zhang, T. Zentgraf, E. Ulin-Avila, D. A. Genov, G. Bartal, and X. Zhang, “Three-dimensional optical metamaterial with a negative refractive index,” *Nature*, vol. 455, p. 376, 2008.
- [7] A. Vallecchi, M. Albani, and F. Capolino, “Collective electric and magnetic plasmonic resonances in spherical nanoclusters,” *Opt. Express*, vol. 19, no. 3, pp. 2754–2772, 2011.
- [8] S. N. Sheikholeslami, H. Alaeian, A. L. Koh, and J. A. Dionne, “A Metafluid Exhibiting Strong Optical Magnetism,” *Nano Lett.*, vol. 13, no. 9, pp. 4137–4141, 2013.
- [9] V. Ponsinet, P. Barois, S. M. Gali, P. Richetti, J. B. Salmon, A. Vallecchi, M. Albani, A. Le Beulze, S. Gomez-Grana, E. Duguet, S. Mornet, and M. Treguer-Delapierre, “Resonant isotropic optical magnetism of plasmonic nanoclusters in visible light,” *Phys. Rev. B*, vol. 92, no. 22, p. 220414, 2015.
- [10] Z. Qian, S. P. Hastings, C. Li, B. Edward, C. K. McGinn, N. Engheta, Z. Fakhraai, and S.-J. Park, “Raspberry-like Metamolecules Exhibiting Strong Magnetic Resonances,” *ACS Nano*, vol. 9, no. 2, pp. 1263–1270, 2015.
- [11] C. Li, S. Lee, Z. Qian, C. Woods, S.-J. Park, and Z. Fakhraai, “Controlling Magnetic Dipole Resonance in Raspberry-like Metamolecules,” *J. Phys. Chem. C*, vol. 122, no. 12, pp. 6808–6817, 2018.
- [12] Y. A. Urzhumov, G. Shvets, J. Fan, F. Capasso, D. Brandl, and P. Nordlander, “Plasmonic nanoclusters: a path towards negative-index metafluids,” *Opt. Express*, vol. 15, no. 21, pp. 14129–14145, 2007.
- [13] A. Vallecchi, M. Albani, and F. Capolino, “Effect of irregularities of nanosatellites position and size on collective electric and magnetic plasmonic resonances in spherical nanoclusters,” *Opt. Express*, vol. 21, no. 6, pp. 7667–7685, 2013.
- [14] A. Désert, I. Chaduc, S. Fouilloux, J.-C. Taveau, O. Lambert, M. Lansalot, E. Bourgeat-Lami, A. Thill, O. Spalla, S. Ravaine, and E. Duguet, “High-yield preparation of polystyrene/silica clusters of controlled morphology,” *Polym. Chem.*, vol. 3, no. 5, pp. 1130–1132, 2012.
- [15] C. Chomette, M. Tréguer-Delapierre, N. B. Schade, V. N. Manoharan, O. Lambert, J.-C. Taveau, S. Ravaine, and E. Duguet, “Colloidal Alchemy: Conversion of Polystyrene Nanoclusters into Gold,” *ChemNanoMat*, vol. 3, no. 3, pp. 160–163, 2017.
- [16] C. Chomette, “Thèse de l’université de Bordeaux: Design and synthesis of plasmonic meta-atoms from patchy particles,” 2015.
- [17] A. Désert, “Thèse de l’Université Bordeaux 1: Colloïdes hybrides silice/polystyrène de morphologie contrôlée,” 2011.

Chapter I:
State-of-the-art
and objectives

1. Metamaterial concept

A metamaterial is an artificial composite material whose internal structure generates electromagnetic properties that do not exist in natural environments. In general, those structures are artificially engineered and made of periodically or randomly distributed structured elements called “meta-atoms” or “nanoresonators” (Figure 10A). Their size and spacing should be much smaller than the wavelength (λ) of electromagnetic waves (Figure 10B) since the metamaterial has to be considered as an effective medium in order to avoid any diffractive effects.

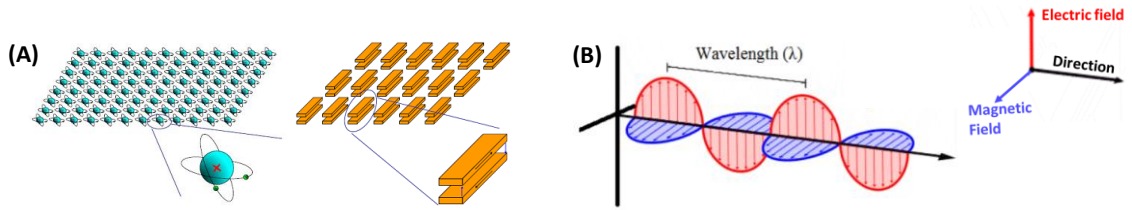


Figure 10: Scheme of (A) a conventional material made of atoms (left) and a metamaterial with artificially structured “meta-atoms” (right); (B) an electromagnetic wave, based on an oscillating electric field and an oscillating magnetic field

This thesis focused on electromagnetic metamaterials for visible light. Such materials can be characterized by a complex refractive index \tilde{n} , which is dependent on the wavelength λ of the electromagnetic wave[1]:

$$\tilde{n}(\lambda) = n(\lambda) + ik(\lambda)$$

Equation 1

where n is the real part of the refractive index, also called optical refractive index and k is the imaginary part and represents the absorption coefficient, *i.e.* the energy loss of an electromagnetic radiation which passes through the medium [2]. If $n(\lambda)$ becomes real at some wavelength, the electromagnetic wave can go through the medium without being absorbed (with $k(\lambda) = 0$), leading to a transparent medium at this wavelength. For all media, $\tilde{n}(\lambda)$ can be defined as:

$$\tilde{n}(\lambda) = \sqrt{\tilde{\epsilon}(\lambda)\tilde{\mu}(\lambda)}$$

Equation 2

where $\tilde{\epsilon}(\lambda)$ is the complex electrical permittivity, and $\tilde{\mu}(\lambda)$ the complex magnetic permeability. They quantify the response of the medium to electrical and magnetic excitations, respectively.

Materials can be classified according to their real part of electrical permittivity $\tilde{\epsilon}(\lambda)$ and magnetic permeability $\tilde{\mu}(\lambda)$ [3],[4]. Figure 11 shows materials classification into 4 quadrants:

Quadrant I corresponds to materials called “Double Positive” (DPS) with $\text{Re}(\tilde{\epsilon})$ and $\text{Re}(\tilde{\mu}) > 0$ which include most dielectric materials; Quadrant II defines materials with $\text{Re}(\epsilon) < 0$ and $\text{Re}(\mu) > 0$, called “ ϵ negative media” (ENG), which include metals, ferroelectric materials, and doped semiconductors; Quadrant III represents the category of “double negative (DNG)” materials, which have both $\text{Re}(\tilde{\mu})$ and $\text{Re}(\tilde{\epsilon}) < 0$ and cannot be found in nature; Quadrant IV corresponds to “ μ negative (MNG)” materials such as ferrite materials, with $\text{Re}(\tilde{\epsilon}) > 0$ and $\text{Re}(\tilde{\mu}) < 0$.

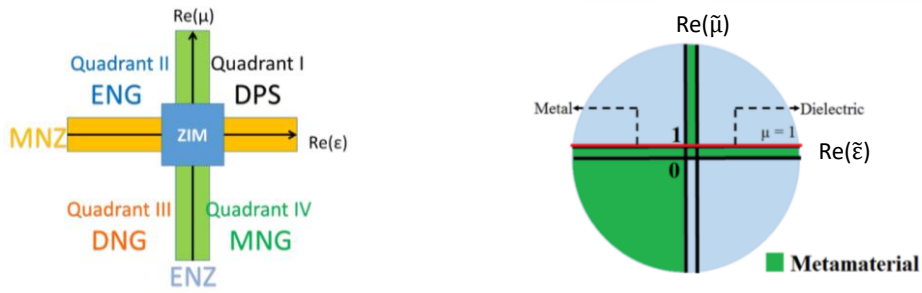


Figure 11: Classification of materials by the values of $\text{Re}(\tilde{\mu})$ and $\text{Re}(\tilde{\epsilon})$. [5,6] DPS: double positive media, ENG: ϵ negative media, MNG: μ negative media, DNG: double negative media, ENZ: ϵ near zero media, MNZ: μ near zero media, ZIM: zero index media.

The permittivity and permeability of a conventional material depend on the response of the different atoms (structural units) constituting the material. An appropriate structuring of the material is required to induce the original electromagnetic properties of a metamaterial. Indeed, metamaterials properties depend on the precise design of their meta-atoms, *i.e.* their shape, geometry, size, orientation and arrangement. This gives them their smart properties to manipulate electromagnetic waves by blocking, absorbing, enhancing, or bending waves in order to go beyond of what is possible with conventional materials.

1.1 Brief history

The concept of metamaterials was introduced in 1968 by Veselago, who investigated the behavior of an electromagnetic wave in a material with a negative permittivity, by applying the Maxwell equations to this material [7]. He reported that the electromagnetic wave could propagate through these materials in a very unusual way. Such media were called “left-handed materials” as the trihedral formed by the electric field, the magnetic field and the wave vector does not obey to the usual right hand rule, contrary to conventional materials for which the trihedral is indirect.

In this case, when light goes in a negative material medium, the law of refraction (Equation 3) is still satisfied at the interface, but the angle of refraction is negative.

$$n_1 \sin \theta_1 = n_2 \sin \theta_2$$

Equation 3

It means that the propagation direction of light changes at the interface between two media and the refracted beam lies on the same side of the normal as the incident one (Figure 12b).

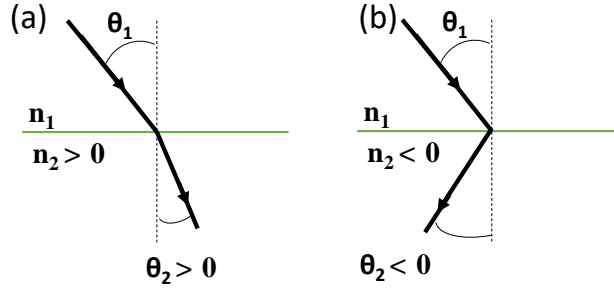


Figure 12: Light refraction at the interface (green) between two media. (a) In a conventional material, (b) in a material with a negative refractive index

The idea of negative refractive index was considered physically impossible for thirty years because of the absence of materials with a negative magnetic permeability. It is in 1999, that Pendry *et al.* theoretically reported for the first time the possibility to generate a magnetic response from objects without magnetic properties, *i.e.* a split-ring resonator (SRR) (Figure 13B) [8]. SRR are planar devices based on a concentric and incomplete loops of metal embedded in a dielectric, with a size smaller than the considered wavelength. Therefore, a strong coupling can occur between the incident electromagnetic wave and the circulating current modes that can be tuned through the geometry of the device. Such resonator can be compared as a LC circuit (Figure 13A). Indeed, the concentric rings of metal give the device inductance L , while the gaps in the metal and the close proximity of concentric rings provide capacitance C . The resonant frequency of the LC circuit can be engineered by the ring design and the gap. Therefore, the circulating current in the plane generates a magnetic dipole pointing out of the plane.

Shelby *et al.* confirmed experimentally the theory of Pendry *et al.* by fabricating two-dimensional arrays of copper SRR [9]. They showed that millimeter-scaled resonators with the design shown in Figure 13C can display both negative permeability and permittivity in the microwave regime. They reported that the refractive index of such metamaterial was negative at microwave frequencies.

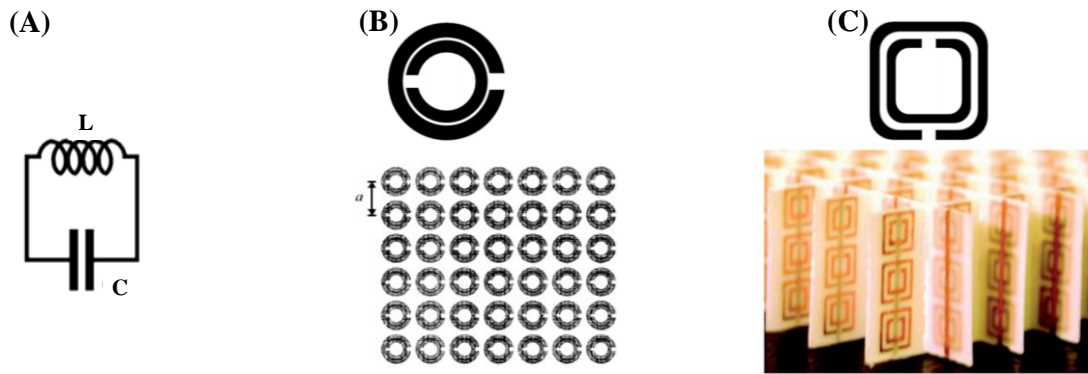


Figure 13: (A) A split-ring resonator uses external electromagnetic waves to establish a circulating current resonance, like that found in an LC circuit; (B) Illustration of a square array of SRR [8]; (C) Photograph of the first left-handed metamaterial consisting of square copper SRR and copper wire strips on fiber glass circuit board material [9].

1.2 Applications

The unique electromagnetic properties of metamaterials can pave the way for many applications in optics. Superlenses devices were fabricated by the use of metamaterials to go beyond the diffraction limit and to overcome the limitation in the conventional optical devices or lenses [10,11]. Indeed, the emission or scattering of the light from an object requires the propagation and the evanescence of the waves. Thus, the evanescent waves lead to a diffraction-limited image, as they cannot be collected at the image plane by using a conventional lens. The use of a superlens, made of a planar metamaterial with a negative refractive index, allows to overcome those waves decay and to reconstruct the image of the object in the near field.

Another application is the cloaking devices used to bend light around an object and so make it partially or wholly invisible (Figure 14A). The first experimental device was fabricated by Pendry et al. in the microwave range [12,13]. The metamaterial consists in a multilayer with an ensemble of circular films on which SRR are printed (Figure 14B). The size of resonators evolves regularly from the inner circle to the outer circle conferring them different magnetic resonances. Thus, the electromagnetic wave is guided by the modulation of the refractive index and more exactly of the magnetic permeability in the material.

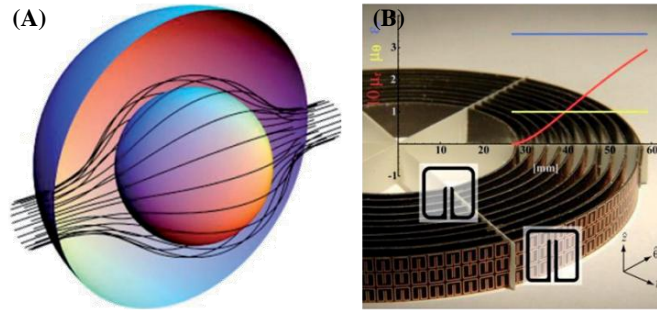


Figure 14: (A) Sketch of an electromagnetic cloaking device; (B) Photograph of the first prototype cloaking device operating in microwaves range [12,13].

1.3 Bottom-up vs. top-down fabrication routes

As previously mentioned, the fabrication of metamaterials active at the visible range requires a nanoresonator with a specific shape and a size which should be lower than the considered wavelength. It is thus challenging. Historically, top-down methods such as electron-beam lithography and focused ion beam milling were used to fabricate the first metamaterial [14-17]. Even if those methods enable the fabrication of nanoresonators such as SRR, they have several drawbacks: the fabrication of a bulk material with a millimeter size, which requires 10^{12} - 10^{15} nanoresonators is time consuming, costly, and resolution-limited by the spot size (~ 10 nm) [18]. Another drawback is that top-down methods produce only two-dimensional nanoresonators leading to a system anisotropy: the incident wavelength needs to be in a particular direction to interact efficiently with the material and to exhibit meta-properties.

Nowadays, many applications require metamaterials with an isotropic response. Therefore, the fabrication of a nanoresonator with a well-controlled design and size becomes trickier. Thus, bottom-up approaches can be good candidates to engineer in a precise way the meta-atoms shape and size. If a colloidal suspension of isotropic subwavelength nanoresonators can be synthesized: (i) the meta-atoms orientation relative one to another and relative to the incident light would have no effect on the optical properties of the metamaterial; (ii) their random dispersion in a suspension would still respond to incident light. Thus, a concentrated colloidal nanoresonators suspension would be a fluid metamaterial, also known as metafluid [19]. Additionally, a metafluid can be manipulated in microfluidic devices and hence shaped into 3-dimensional (3D) materials.

Consequently, the use of a bottom-up method to control the design of the nanoresonators, and the use of a self-assembly technique to fabricate a highly organized 3D metamaterial

active in the visible range represents a challenging way to fabricate metamaterials with original optical properties.

2. Raspberry-like nanoparticles as nano-sized split-ring resonators

2.1 Theoretical investigations

The concept of raspberry-like nanoclusters was introduced by Alù *et al.* and Simovski *et al.* by theoretical investigations [20-22]. Their design consists in a central dielectric core surrounded with gold or silver plasmonic particles (Figure 15).

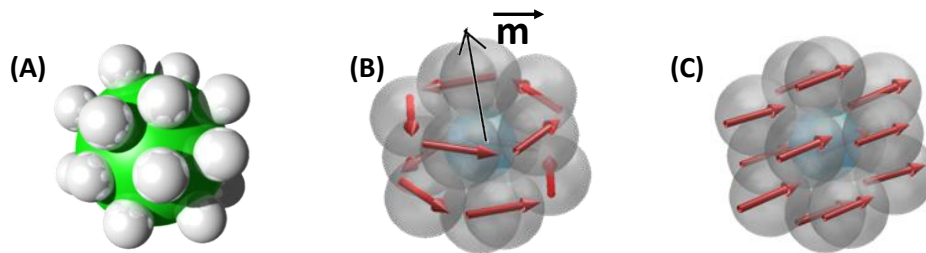


Figure 15: (A) Proposed design for isotropic nanoresonators; (B) Electric and (C) magnetic resonant modes of a raspberry-like nanocluster [23].

Simovski *et al.* reported indeed that this particular design allows a plasmonic coupling between the satellites due to their size and their in-between satellites gap leading to an artificial magnetism. Indeed, this architecture enables a circulating current around the dielectric core, which generates a magnetic resonance orthogonally to the incident electric field and the electric resonance [23]. This creates a negative magnetic permeability in a certain frequency range within the optical spectrum. Additionally, it has been shown that, in a given frequency region, a material made of the self-assembly of these magnetic nanoclusters would be a DNG operating in the visible range.

2.2 Synthesis, optical characterization, and assembly into materials

2.2.1 Synthesis approach and optical investigations

Several synthesis methods were developed to fabricate raspberry-like nanoclusters. In most cases, silica or polystyrene (PS) beads have been used as a dielectric core because of their easy synthesis, modulation in size and surface functionalization. Until now, two main approaches based on (i) the self-assembly of plasmonic particles on the silica core or (ii) the seeded growth of a silver or gold nucleus on the silica core were carried out.

2.2.1.1 Self-assembly of small plasmonic particles on a dielectric core

Mühlig *et al.* extended the method of Halas *et al.* to functionalize silica nanoparticles (NPs) by an organosilane bearing amine groups [24]. Thus, 150 nm silica particles were modified by using N-[3-(trimethoxysilyl)propyl]-ethylenediamine (EDPS) and 8 nm size gold NPs were attached onto the dielectric core by electrostatic interactions (Figure 16A). Xue *et al.* reported that in the case of large size (from 13 to 32 nm) plasmonic NPs, such a ‘glue’ is not robust enough due to the high difference of density between silica and gold [25,26].

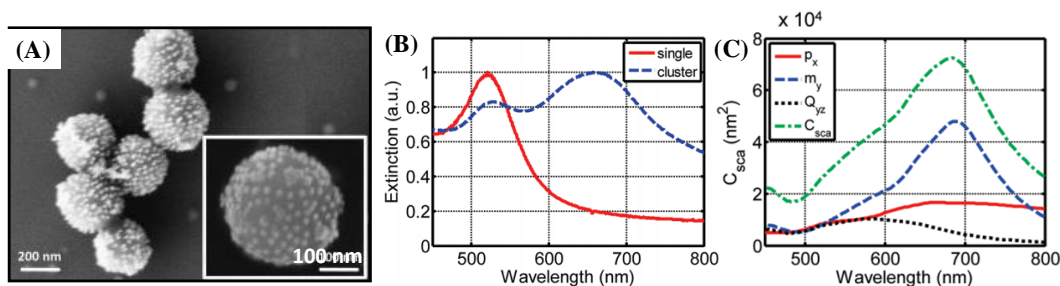


Figure 16: (A) TEM image of raspberry-like clusters made of EDPS modified silica core and 8 nm gold seeds; Measured extinction spectra of: (B) fabricated core-shell clusters in solution (blue dashed curve) and single gold nanospheres (red solid curve); (C) Simulated contributions of the relevant multipole moments: P_x : Electric dipole; m_y : magnetic dipole; Q_{yz} : electric quadrupole and C_{sca} : Scattering cross section of the core shell clusters as a function of the wavelength [24].

Mühlig *et al.* investigated the optical behavior of such clusters produced by self-assembly approach [24]. They carried out UV-absorption spectroscopy of gold NPs before and after the assembly onto a silica core. They reported a red-shift and a broadening of the extinction spectrum of the gold nanoparticles, after the assembly onto the silica core. They carried out simulations to evidence the magnetic, multipole and electric components.

2.2.1.2 Self-assembly of larger plasmonic particles on a dielectric core

Dionne *et al.* carried out the self-assembly of large silver NPs (> 20 nm) on a 90 nm PS core via protein-directed interactions [27]. The PS core was functionalized with streptavidin and the 35 nm silver satellites with biotin-terminated polyethylene glycol (Figure 17A). The specific chemical recognition of streptavidin to biotin allows silver NPs to strongly interact with PS particles to form raspberry-like nanoclusters (Figure 17B). They reported a gap in-between the satellites of 3.8 nm. They performed the very first time experimental investigations of the magnetic properties of the nanoclusters. They showed the presence of an isotropic magnetic dipole in the visible range, by dark field spectroscopy and angle polarization-resolved scattering spectroscopy (Figure 17C).

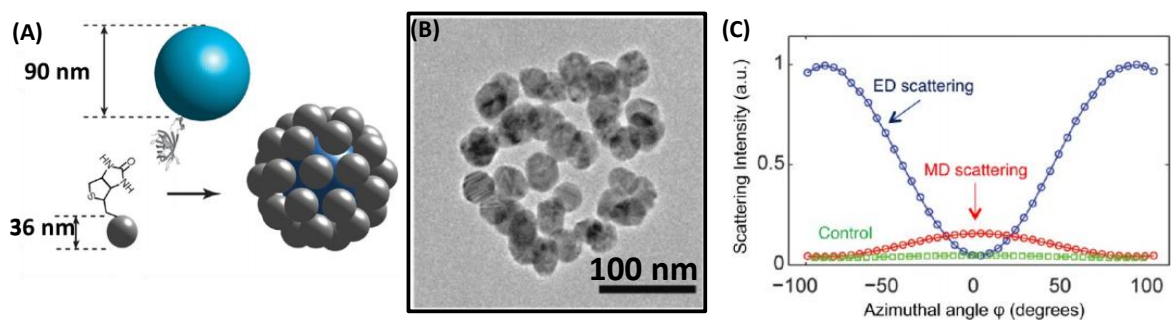


Figure 17: (A) Schematic representation of the raspberry made of a PS core (90nm) and large silver NPs (35 nm) via protein-directed assembly; (B) TEM image of the raspberry-like NPs; (C) Optical characterization of the bulk metafluid by angle polarization-resolved light scattering spectroscopy highlighting the electric (ED) and magnetic (MD) mode at 633 nm; the control curve represents the magnetic mode of a suspension of silica NPs with unassembled silver NPs [27].

Le Beulze *et al.* and Gomez-Grana *et al.* reported another fabrication routes based on the use of polyelectrolytes [28,29]. They pre-deposited polydiallyldimethylammonium chloride (PDDA) and poly(sodium 4-styrenesulfonate) (PSS) onto the surface of 100 nm silica particles. Subsequently, citrate-stabilized gold NPs (30 nm) were successfully adsorbed onto the silica cores (Figure 18A). The authors showed that poly(1-vinyl-4-methyl-1,2,4-triazolium iodide) (PVMe⁺I) may be alternatively used alone, especially with silver plasmonic NPs (Figure 18B). For both methods, a thin layer (5 nm) of silica was grown on the surface of the raspberry-like assemblies to make them more robust and colloidal stable.

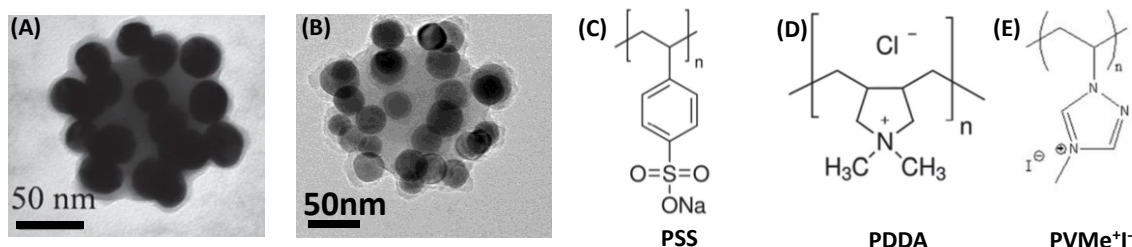


Figure 18: TEM images of raspberry-like NP made of: (A) a silica core (106 nm) and 26 gold satellites (30 nm) encapsulated in a thin silica layer; (B) silica core (90 nm) and 22 silver satellites (25 nm) with a thin silica layer of 5 nm; (C) to (E) Molecular structures of PSS, PDDA and PVMe⁺I [28,29].

The scattering intensity of magnetic and electric modes were investigated by static light scattering at 530 nm and 444 nm vs. the direction ϕ of the incident polarization for both gold and silver raspberries, respectively. Figure 19-insets shows transverse (red circles) and axial (blue triangles) scattering measured at 530 nm and 444 nm vs. the direction ϕ of the incident polarization for both gold and silver raspberries, respectively. They are fitted for each wavelength to oscillating functions $B_{\perp} + A_{\perp} \cos^2 \phi$ and $B_{\parallel} + A_{\parallel} \sin^2 \phi$, respectively. For both clusters, the common background $B_{\perp} \approx B_{\parallel}$ is less than 4% of the amplitude of the ED mode, confirming the isotropic response of the gold and silver raspberries. The scattering intensities of magnetic and electric modes were investigated in the whole visible spectrum. The

magnetic-to-electric scattering ratio exhibits a clear maximum of 4.5% at 540 nm for the gold-based raspberries consistently with numerical simulations (Figure 10A). For the silver-based raspberries, the magnetic to electric scattering ratio exhibits a sharp maximum of 28 % at 450 nm (Figure 10B).

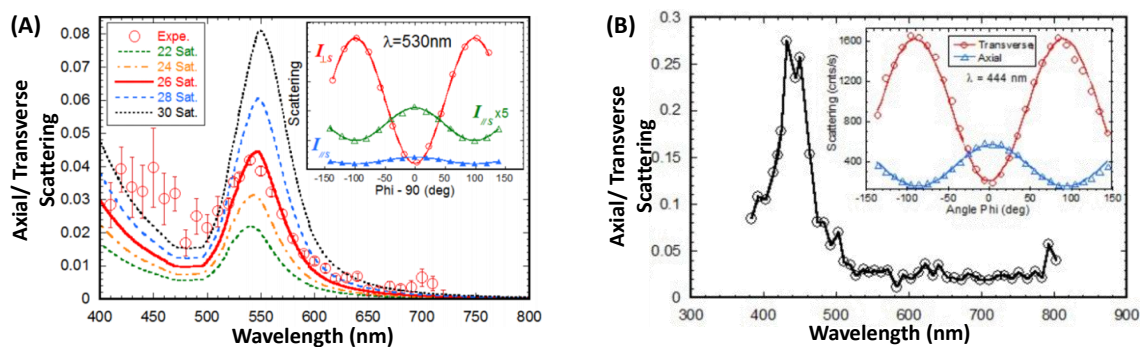


Figure 19: Ratio of axial-to-transverse scattering vs. wavelength: (A) experimental data (red circles), and numerical simulation of gold raspberry-like particles with varying satellites number; (B) of silver raspberry-like particles. The inset shows transverse (red circles) and axial (blue triangles) scattering measured at $\lambda = 530$ nm and $\lambda = 444$ nm, for gold and silver raspberries, respectively; the solid lines are fits to the $\sin^2\phi$ and $\cos^2\phi$ functions [28,29].

2.1.1.3 Seeded-growth of metal satellites on a dielectric core

The seeded-growth approach is based on the adsorption of tiny gold or silver seeds on the dielectric core, and then their subsequent regrowth. Typically, Qian *et al.* carried out experiments using Ag seeds adsorbed onto carboxylate-modified PS particles [30]. Subsequently, they mixed this suspension with a growth solution containing an aromatic surfactant, *e.g.* benzyl dimethyl hexadecyl ammonium chloride, HAuCl_4 , silver nitrate, and ascorbic acid and obtained raspberry-like clusters with gold satellites. They studied the influence on the optical properties of the satellite size adjusted through the volume ratio between the seed and the growth solution ($V_{\text{seed}}/V_{\text{growth}}$) (Figure 20B-C) and the PS core size (Figure 20F-G). They highlighted that increasing the satellites size leads to a red-shift of the plasmon band and a broadening of the overall bandwidth. For each extinction spectra, two main peaks in the visible and near-IR region can be observed. They carried out finite-difference time-domain (FDTD) modeling to investigate the broad profile of the extinction spectra, demonstrating that features and major peak positions of simulated extinction spectra are consistent with the profiles and trends of experimental ones.

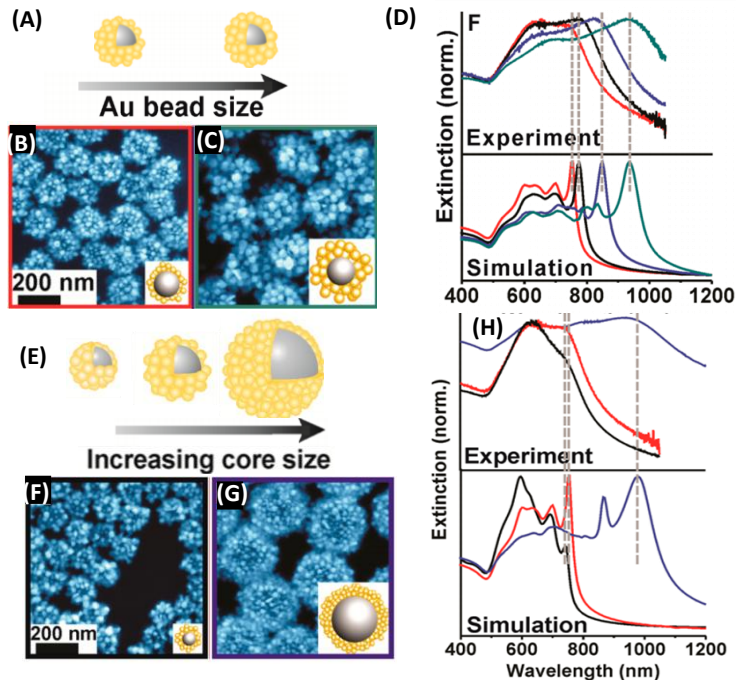


Figure 20: (A) and (E) Schematic description; (B-C) and (F-G) SEM images of raspberries with: (B) $D_{\text{core}} = 96$ nm, $N_{\text{satellites}} = 100$, $R_{\text{satellites}} = 12$ nm, and (C) $D_{\text{core}} = 96$ nm, $N_{\text{satellites}} = 100$, $R_{\text{satellites}} = 19$ nm; (F) $D_{\text{core}} = 56$ nm, $N_{\text{satellites}} = 70$, $R_{\text{satellites}} = 11$ nm; (G) $D_{\text{core}} = 184$ nm, $N_{\text{satellites}} = 800$, $R_{\text{satellites}} = 11$ nm; (D) and (H) Experimental (top) and simulated (bottom) extinction spectra of the samples [30].

Another study was carried out by increasing the silica core size and the number of seeds and by decreasing their size (Figure 20E-G). It led to the broadening of the extinction spectra which is extended into the near IR region. By decomposing the scattering cross section of the raspberries into individual multipole components using FDTD simulations, they highlighted that the spectra broadening arise from absorption, scattering, but also magnetic and electric dipoles and multipole dipoles and thus assigned the magnetic dipole resonance at 1207 nm and the magnetic quadrupole resonance at 995 nm. They also measured experimentally the magnetic and electric contributions of the cluster made of a silica core of 184 nm with 800 satellites of 14 nm by angle polarization-resolved scattering spectroscopy. They reported a magnetic resonance with an intensity comparable to the electric one at 900 nm.

Later, Li et al. extended this method to tune the gap in-between the satellites by varying the chain length of the surfactants [31]. By reducing this gap a red shift of the extinction spectra is observed (Figure 21A-B). Simulations were carried out highlighting that peaks 680 and 900 nm could arise from the electric resonance and magnetic resonance modes, respectively. The authors claim that the magnetic resonance can be influenced by several parameters: (i) the in-between satellites gap, indeed the increase of the in-between satellites gap, leads to an increase and a red-shift of the magnetic resonance (Figure 21C); (ii) the

increase of the satellites size could exhibit stronger and more red-shifted electric and magnetic resonance modes.

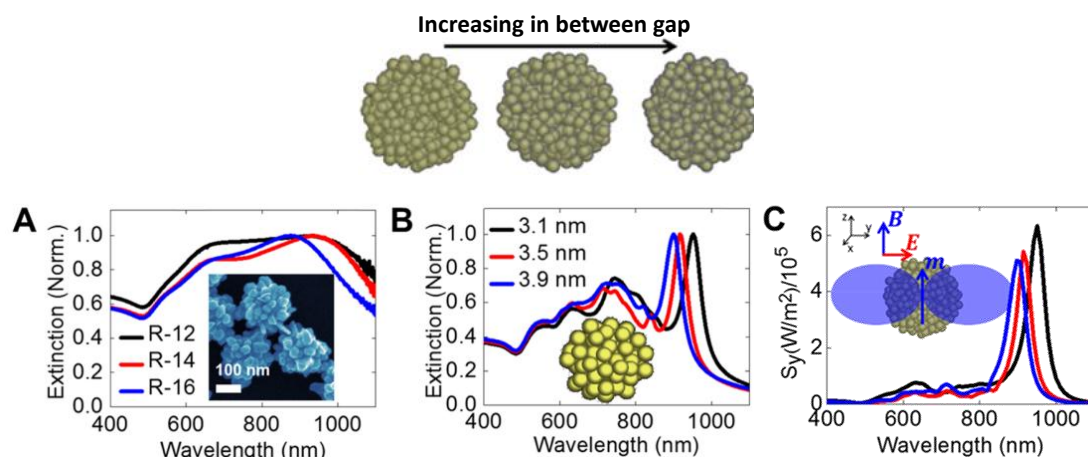


Figure 21: (A) Extinction spectra of raspberries with a PS diameter of 102 nm, 98 satellites of 38 nm using surfactants of different lengths; (B) Simulated far-field extinction spectra of the raspberries varying the gap; (C) Simulated magnetic scattering intensity [31].

To summarize, Qian *et al.* and Li *et al.* reported the synthesis of raspberry NPs claiming the tunability of the dielectric core size from 56 nm to 180 nm, the satellites size from 15 nm to 50 nm and their in between gap from 3.1 nm to 3.9 nm. Their approach has the advantage to produce raspberry-like particles with large satellites size. However, even if they mentioned that the gap in between the satellites can be controlled by the length of the surfactant, they did not mention how they control the number of seeds on the silica core. Additionally, it seems that the morphology and the satellites dispersion on the dielectric core is not well controlled. Several drawbacks can be highlighted, such as (i) the different shapes of the satellites (spiky and non-spherical); (ii) the satellites seem to be anisotropic; (iii) the size of the aggregates seems to be highly polydisperse. Moreover, Qian *et al.* reported that the scattering of the magnetic and electric dipoles are in the near infrared and not in the visible range. Later, Li *et al.* reported by simulation that those clusters could generate a magnetic resonance [30,31].

2.2.2 Material fabricated from raspberry-like sub-units and evidence of the refractive index of the material

Up to now, the observation of a strong artificial magnetism at frequencies of visible or near-infrared light has been reported in several types of 2D anisotropic nanostructures [32-36]. Among the reported works dedicated to the 3D material, only Gomez-Grana's work led to the fabrication and the optical properties of a bulk material. The material was elaborated by microfluidic evaporation and had typical dimensions of 10 mm thick, 100 mm wide and 3-5 mm long. Thus, the sample is thicker than the absorption length of the material and allows the

material to behave as a semi-infinite material. Numerical and experimental values of the refractive index was evaluated (Figure 22C). The refractive index value is less than 1 in the blue region of the spectrum.

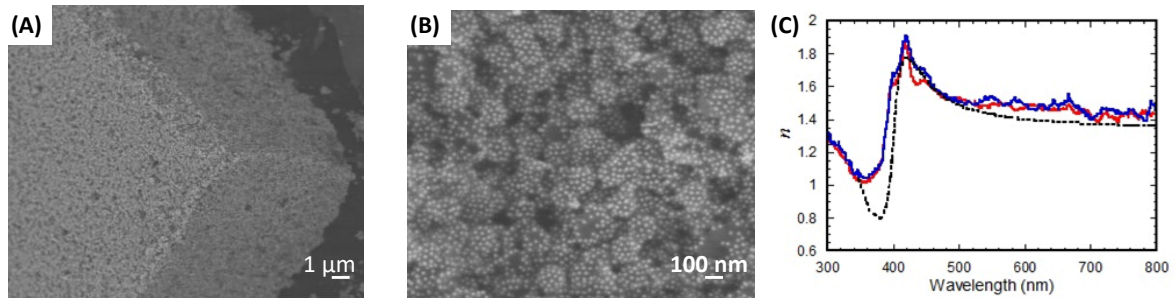


Figure 22: (A) and (B) High-Resolution Scanning Electron Microscopy images of the material made of silver raspberry-like NPs at different scales; (C) Real part of the refractive index of the material. The blue and red curves correspond to the experimental data from spectroscopic ellipsometry at two different positions in the sample, and the black curve corresponds to the finite element numerical simulation of the optical properties of a cubic lattice of homogeneous spheres [29].

3. Plasmonic dodecahedral cluster as a new challenging design

3.1 Theoretical investigations of raspberry like nanoparticles vs. dodecahedral clusters

Our goal was to optimize the magnetic optical response of metallodielectric nanoresonators by specifically controlling the number, the size and the in-between gap of the satellites. Urzhumov *et al.* theoretically investigated the optical properties of a symmetric cluster made of four spherical plasmonic particles whose center were located along the vertices of a tetrahedron [19]. The four gold NPs were spaced by a gap of few nanometers, which yielded to a strong coupling coming from the closely-packed structure and an isotropic magnetic resonance at optical frequencies. They showed that the magnetic resonance was strongly affected by the satellites gap. They also demonstrated that several other structures, *i.e.* octahedron, icosahedron and dodecahedron, can exhibit a similar feature. In 2011, Capolino *et al.* investigated the effect of parameters such as the number of satellites, their size polydispersity and position irregularities. They reported that the magnetic resonance is more affected by those parameters than the electric resonance. They confirmed that the magnetic response is sensitive to the satellites number as well as their size inhomogeneity [37].

Simulations of the optical properties of clusters made of a silica core and a precise number of gold satellites have been performed at the Centre de Recherche Paul Pascal by P. Richetti. Hypothetical clusters in which the satellites position, size and in-between gap can be specifically controlled were considered. The electromagnetic response of those clusters was

computed numerically by the Generalized Multi-particle Mie (GMM) theory, a semi-analytical solution to Maxwell's equations for a system of non-intersecting spheres. Following the Mie theory describing the scattering of a single sphere[38], the scattered fields are expanded in series of modes (electric magnetic and electric quadrupole modes and so on) computed for the whole cluster. In the simulations, the silica relative dielectric permittivity was $\epsilon_{\text{SiO}_2} = 2.25$ and the environment medium was water, with a relative dielectric permittivity $\epsilon_{\text{H}_2\text{O}} = 1.77$. The scattering efficiency can be described as the ratio between the cross section to the clusters area:

$$Q_{scatt}^y = \frac{\sigma_{scatt}^y}{\pi a^2}$$

Equation 4

where Q_{scatt}^y is the scattering efficiency of the “y” which may consider the sum of the all dipoles (tot), electric dipole (ED), magnetic dipole (MD), or electric (EQ) and magnetic (MQ) quadrupolar modes; σ_{scatt}^y is the cross-section of the “y”; and a is the radius of the cluster. The nature of the various resonances of the nanoclusters can be attributed by decomposing the total scattering efficiency Q_{scatt}^{tot} into the contributions originated by the induced electric and magnetic dipole moments Q_{scatt}^e and Q_{scatt}^m , Q_{scatt}^{EQ} , Q_{scatt}^{EQ} , respectively, which were plotted separately.

$$Q_{scatt}^{tot} = Q_{scatt}^e + Q_{scatt}^m + Q_{scatt}^{mult}$$

Equation 5

As a first attempt, the scattering properties of clusters made of a silica core of 100 nm and a specific number of gold satellites made of 4, 6, 8 and 12 were investigated. For each cluster, the total volume of gold was kept constant and implies that the radius of the N satellites scales as $N^{-1/3}$ (Figure 23). Thus, the radius of the gold satellites for each cluster was (i) 57.7 nm for the tetrahedral; (ii) 50.4 nm for the hexahedral; (iii) 45.8 nm for the octahedral and (iv) 40 nm for the dodecahedral clusters.

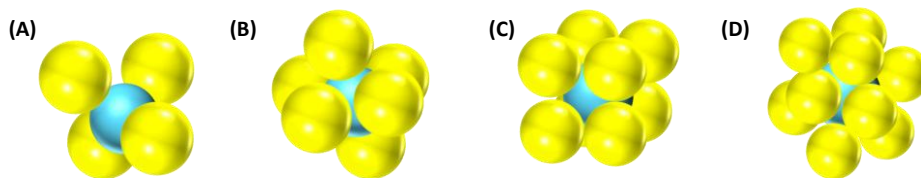


Figure 23: Sketch of the gold: (A) tetrahedral. (B) hexahedral. (C) octahedral and (D) and dodecahedral clusters.

The gold dodecahedral clusters scattering efficiency of the different modes are displayed in Figure 24A. It exhibits a broad electric mode (blue curve) and a magnetic dipole resonance (orange curve) at 720 nm, which has a higher scattering efficiency than the electric one. An

electric quadrupole mode is also generated at 600 nm. Figure 24B shows the magnetic contribution of the four clusters represented in Figure 23. The gold dodecahedral structure has the highest magnetic response. The magnetic dipole scattering efficiency, defined as the scattering cross-section normalized by the geometrical cross-section, reaches $1.1 \cdot 10^5 \text{ nm}^2$.

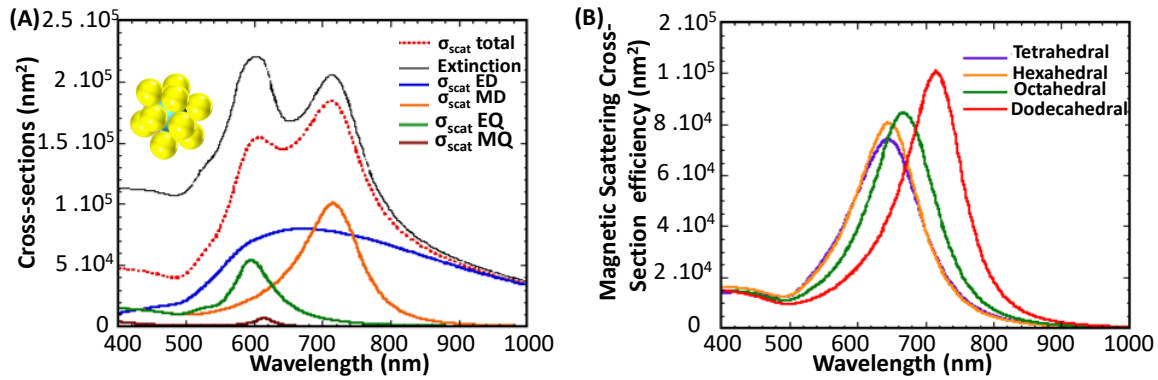


Figure 24: (A) Extinction and scattering cross-sections of a gold dodecahedral cluster in water. The radii of the silica core and of the gold satellites are 50 and 40 nm, respectively; (B) Magnetic (MD) scattering efficiency computed for the tetrahedral, hexahedra octahedral and dodecahedral clusters with a silica core radius of 50 nm and a satellites radius scaling as $N^{-1/3}$ [unpublished results].

Therefore, on the basis of these numerical simulations, the gold dodecahedral clusters were chosen as the most desirable ones for the optimization of the magnetic response. The metallodielectric nanoresonators should be designed with a 100 nm silica core and 80 nm size gold satellites with an in-between gap of 2 nm.

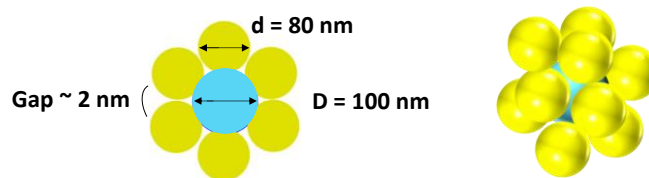


Figure 25: Scheme of the targeted dodecahedral nanoresonators

3.2 How to adjust to 12 the number of satellites on a dielectric core?

3.2.1 Virus templating

Fontana *et al.* reported a synthesis method based on a Cowpea mosaic virus (CPMV) which is a well-characterized plant virus with an icosahedral symmetry produced in gram amounts [39,40]. This virus symmetry enables to define the location of gold NPs on the virus scaffold. Therefore, they engineered CPMV to present specifically cysteine amino acids with thiol groups at the twelve vertices of the icosahedron. They demonstrated that gold NPs of 17 nm size can be attached to the thiol groups, leading to a cluster with twelve gold satellites.

However, they reported that the control of the number of gold satellites per virus was difficult when increasing their size.

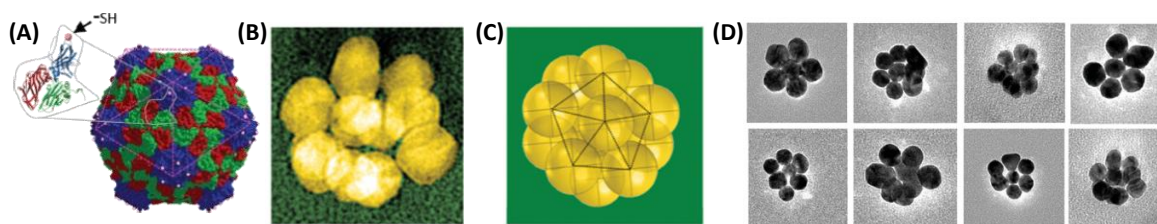


Figure 26: (A) CPMV structure; The inset shows the protein subunit; in pink is a single cysteine (thiol containing amino acid) in the loop; (B) False-colored TEM image of the virus with 18 nm size gold NPs attached. (d) Model of a nanocluster (NC) with 30 nm gold NPs with a similar orientation to (B). The dotted black lines represent a five-fold symmetry axis; (D) Representative TEM images of NC with 30 nm gold NPs attached [39].

3.2.2 Controlled aggregation

Manoharan *et al.* reported a strategy to fabricate clusters of cross-linked PS microspheres of 844 nm, with sulfate groups covalently bonded to their surface and typically packed together in a water/toluene system [41]. The spheres were initially dispersed in toluene, a good solvent of polystyrene (PS). In such conditions, the dissociation of sulfate groups is limited, but the Van der Waals forces between the particles are much smaller than in water [42] leading to the particles to swell with the solvent and to interact only through a short ranged steric (entropic) repulsion. Further, water was added and mixed to create an oil-in-water emulsion consisting of small droplets of toluene leading to a strong bounding of the PS microspheres to the droplet interfaces. The evaporation of toluene enabled the particles to pack together and to form clusters with a certain number of PS spheres (Figure 27A). Indeed, the number of spheres into each droplet was not the same due to the fact that, initially, the droplets were not uniform in size, leading to polydisperse clusters. Density gradient centrifugation was used to separate the clusters based on the difference in sedimentation velocity, or average hydrodynamic radius [43]. This method allows the synthesis of clusters made of a controlled number of PS spheres from 4 to 15 spheres (Figure 27A). Thus, with such a strategy, dodecahedral clusters can be fabricated. Further, Urban *et al.* extended this method to plasmonic particles [44]. Indeed, they functionalized 15 nm size citrate-stabilized gold NPs with thiol-terminated PS (PS₁₁₅-SH, $M_n = 12,000$) and incubated them in dimethylformamide (DMF) with amphiphilic diblock copolymer, *i.e.* polystyrene-block-poly(acrylic acid) (PS-PAA). A small amount of water was introduced leading to pack the particle into clusters. The same method was used for 60 nm silver NPs. This strategy enabled the formation of clusters of various morphologies (Figure 27B-C), including dodecahedral

ones. However, the authors were not able to purify them and to extend this method to larger gold NPs. In addition, the yield of the gold dodecahedral clusters is low.

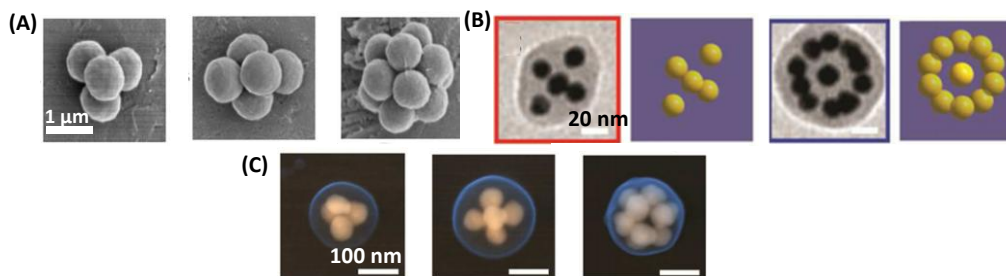


Figure 27: (A) Typical PS clusters obtained by Manoharan *et al.*; Typical clusters obtained by Urban *et al.* and made of (B) 17 nm gold NPs and (C) 60 nm silver particles [41,44].

3.2.3 Templating with colloidal crystals?

Yuan *et al.* developed a strategy to synthesize dodecahedral clusters from poly(N-isopropylacrylamide) (PNIPAM) microgel spheres of 310 nm and 800 nm [45]. Those particles were synthesized via free radical precipitation polymerization [46]. Two sets of PNIPAM particles were specifically modified with vinyl and thiol groups, respectively. Further, highly ordered colloidal crystals were prepared by the self-assembly of those particles with a HS-PNIPAM to vinyl-PNIPAM particles ratio of 40. Subsequently, the crystal was irradiated with UV light, in the presence of a photo-initiator, added before the crystallization of the sample leading to thiol-ene click reaction between the vinyl groups on vinyl-PNIPAM microgel particles and the thiol groups on the neighboring HS-PNIPAM microgel particles (Figure 28AB).

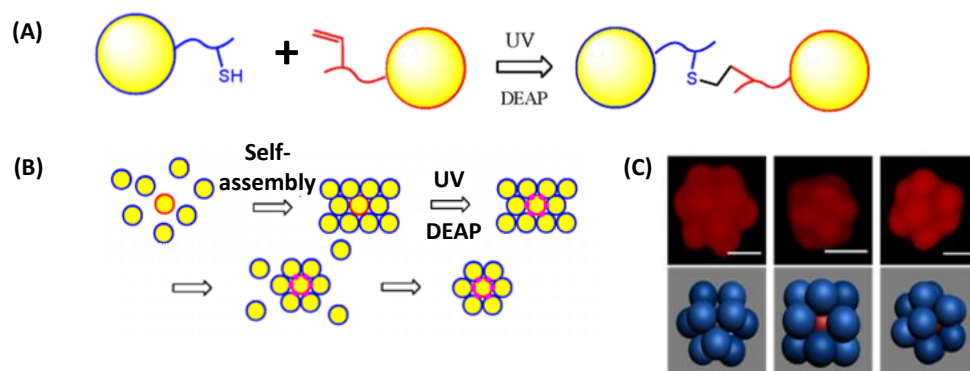


Figure 28: (A) Thiol-ene reaction between vinyl- and HS-PNIPAM, (B) Synthesis of microgel clusters by first assembling the microgel spheres into colloidal crystal, followed by bonding vinyl-PNIPAM microgels with the surrounding SH-PNIPAM microgels, (c) Reconstructed 3D confocal images of fluorescently labelled clusters (first row, scale bar: 1 μm)

Therefore, dodecahedral clusters were obtained when one vinyl-PNIPAM microgel is located in the center of twelve SH-PNIPAM microgels and can be linked to them by thiol-ene

bonds. This process also allowed the fabrication of other by-product clusters of more or less than thirteen spheres and it also involves the fabrication of clusters made of several vinyl-PNIPAM particles surrounded with several HS-PNIPAM particles. Finally, the particle batches were purified by density gradient centrifugation [41].

By extending this method to silica particles and specifically modifying silica surface by thiol and vinyl groups, respectively, silica dodecahedral particles could be synthesized [26,47]. Indeed, as mentioned previously, the dodecahedral clusters fabricated by this strategy are made of a central core and twelve satellites functionalized with thiol groups. Thus, by adding gold seeds on the HS-silica and by using a conventional seeded growth method implying a gold precursor such as HAuCl_4 and a reducing agent, a gold nanoshell can be formed [48]. This method via self-assembly is interesting and could be extended for our investigations. However, the size of the particles should be reduced to reach the previously mentioned particle design specifications. As we can see in Figure 28C, the spheres seem to be in contact leading to a small gap in between the satellites. Consequently, it is difficult to grow gold seeds on the SH-silica satellites; otherwise, the satellites would touch each other. Using larger vinyl-silica NPs or smaller HS-silica NPs satellites should lead to an increase of the in-between satellites gap and then a gold shell could be grown around the satellites.

Another strategy based on this self-assembly method could also be implemented. Indeed, gold and silica NPs could be synthesized and specifically functionalized with thiol and vinyl groups, respectively [47,49]. To form colloidal crystals from these two types of precursors a gold suspension can be first kept to sediment on a substrate to form a monolayer. Secondly, a small amount of silica particles can be added, and finally an excess of gold NPs can be deposited following with the irradiation of the sample in order to form thiol-ene bonds between gold and silica NPs (Figure 29). By adding sequentially the colloidal suspensions, we could expect to avoid any problem due to the density contrast between gold and silica. Indeed, as the gold density is higher than the silica one, the deposition of a mixture of both suspensions could lead to a fast sedimentation of all gold NPs and the deposition of the silica particles on the top of the gold NPs layer. Side-clusters with less or more gold satellites or with several silica particles could also be formed. A purification step, such as density gradient centrifugation would be required to remove these non-desired clusters.

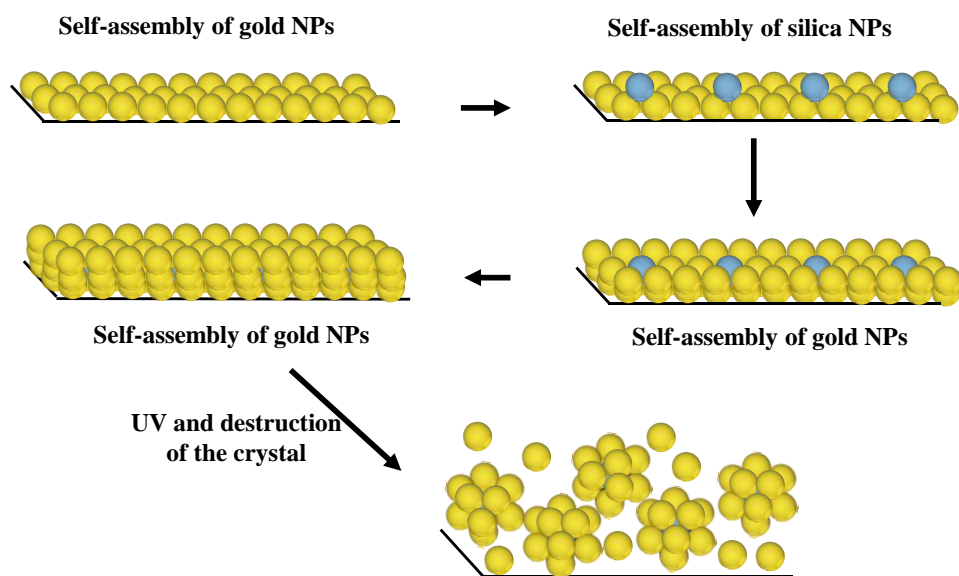


Figure 29: Hypothetical strategy to synthesize gold dodecahedral clusters via the self-assembly method.

To reach a high yield of gold dodecahedral clusters, the position of the silica and gold particles should be carefully controlled. Indeed, several situations can occur: (i) if the gold NPs have an important gap between each other, side-product clusters can be formed, reducing the clusters yield; (ii) the silica NPs deposition should be homogeneous and should maintain a certain distance between each other in order to avoid the formation of clusters with multiple silica NPs. The distribution of the gold particles around the silica core should be homogeneous to form regular dodecahedral clusters. Therefore, the yield of those clusters could be low due to those limitations. Additionally, this method could be costly because of the use of a large quantity of gold NPs. Due to these several drawbacks, this method was not envisaged.

3.2.4 DNA origami as a scaffold

Over the last decade, numerous progress in the programmable DNA-assembly have been done to fabricate original building-block structures with a controlled shape, including the preparation of periodic and aperiodic 2D nanopatterns [50-52] and 3D polyhedra [53-55]. Zhang *et al.* synthesized icosahedral origami by a two steps synthesis method based on (i) the self-assembly of three DNA single strands and (ii) the self-assembly of a motif (tile) through sticky-end association between the tiles (Figure 30A) [56]. This tile corresponds to a five-way branched vertex in the final icosahedra structures. In the icosahedra, the five-point-star tiles are not planar, they bend out of the original plane by 32° . In order to obtain specifically

dodecahedral clusters, the tiles should be enough flexible for such a degree of bending. Thus, the central single-stranded loops (red color segments, Figure 30 center) should have a specific design. The icosahedra fabrication consists in mixing and slowly cooling down the five-way branched DNA vertex mixture from 95°C to 23°C, leading to the DNA single strand to first recognize the complementary DNA and assembled into individual five-point-star tiles that further formed the icosahedra through sticky-end association between the tiles (Figure 30A2-A3). Each sticky end is made of an ensemble of four G-C base pairs. The strong G-C base pairing imposes kinetic controls in the assembly process and ensures the stability of the final assemblies.

Veneziano *et al.* reported another method based on a top-down approach consisting in an automatic inverse design procedure that programs arbitrary wireframe DNA assemblies and which is able to fabricate several structures such as Platonic DNA origami via polymerase chain reaction [57]. However, for both strategies the size of the obtained structures is too small (~ 40 nm). Very recently, Wagenbauer *et al.* reported a strategy to synthesize large size DNA origami with icosahedral shape [58]. For this, they designed a reactive vertex made of (i) a triangular brick (blue sites) with three docking sites; (ii) V brick (light grey sites) with a tunable angle; (iii) a connector brick (red sites) with recessed docking sites on one face and a self complementary dock on the opposite face (Figure 30B1). The reactive vertex can be programmed to self-assemble by adding salt. Tetrahedron, hexahedron or dodecahedron can be obtained by tuning the angles in the wings of the reactive vertex, which should be 55°, 35° or 22°, respectively. Figure 30B2 highlights the icosahedral structure fabricated by this strategy.

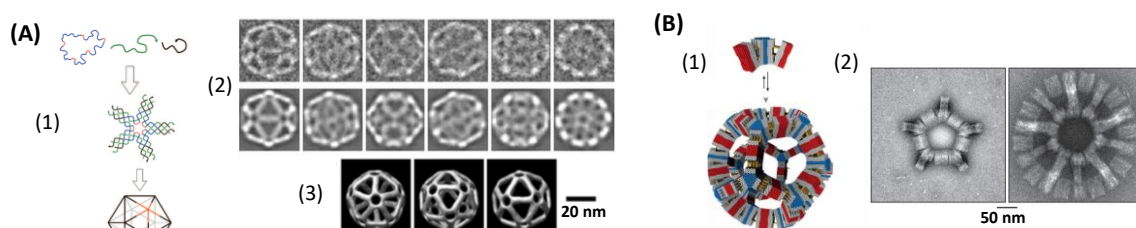


Figure 30: (A1) scheme of the two steps fabrication of the icosahedral DNA origami: (i) three single strands DNA assemble into sticky-ended five-point-star motifs (tiles)[top], (ii) assembly of the sticky-ended five-point-star motifs into icosahedra [center and down]; (A2) Comparison of class average of particle images with similar views (Upper) and the corresponding computer generated model projections (Lower). (A3) Three views of the DNA icosahedron structure reconstructed from cryo-EM images. (B1) Reactive vertices designed to self-assemble into a tetrahedron; (B2) Typical TEM images of a dodecahedron [56,58].

Thus, those structures can be used as a scaffold due to their regular morphology with a controlled number and well-defined vertices and in-between gap and can pave the way to add in a specific position gold NPs. Thus, Gang *et al.* developed a strategy to self-assembled gold

NPs on octahedral DNA origami structure [59]. The DNA frame was specifically designed with vertices, which can be specifically encoded with distinctive single-stranded DNA ‘sticky ends’. By functionalizing specifically the gold NPs (10 nm) by a complementary DNA to the vertices, the NPs can be self-assembled on the vertices of the octahedral DNA origami (Figure 31).

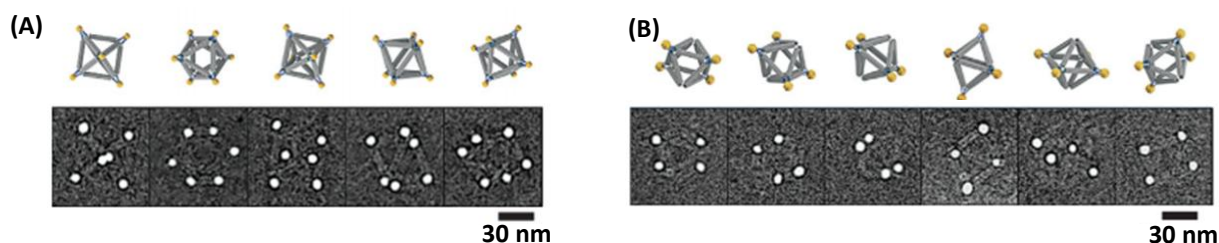


Figure 31: (A) and (B) Series of selected raw cryo-EM images of the octahedron DNA origami with 6 and 4 gold NPs, with corresponding views from the 3D design model

Therefore, we can envisage to combine the synthesis of icosahedra DNA frame and the method to make sticky the vertices of the frame in order to precisely organize gold NPs in a dodecahedral structure. However, Gang *et al.* noticed that the self-assembly of 15 nm gold NPs leads to the distortion of the DNA origami framework [59]. Thus, we may wonder whether such structure can be rigid enough to hold larger gold NPs (90 nm).

3.2.5 Using dimpled-silica particles as a scaffold

Désert *et al.* developed a strategy to synthesize silica particles with a controlled number of dimples [60]. It is based on a multistep synthesis starting from PS/silica clusters prepared by a seeded-growth emulsion polymerization reaction. Those clusters were prepared in high morphology yield (up to 80 % for tetrapods, hexapods, and 74% for dodecapods) at the gram scale. The first step was the production of highly size-monodisperse silica particles through a seeded-growth approach followed by a surface modification using a hydrophobizing and copolymerizing silane [61,62]. The second step consists in the seeded-growth emulsion polymerization of styrene performed in the presence of a surfactant mixture made of Synperonic[®] NP 30 and SDS and initiated by the thermal decomposition of sodium persulfate (Figure 32). Tetrapods, hexapods and dodecapods were synthesized from silica seeds with diameters of 55 nm, 85 nm and 85 nm, respectively. Chomette *et al.* extended this synthesis to functional tetrahedral and hexahedral-dimpled silica NPs. Thus, the silica cores of the tetrapods and hexapods were regrown through a hydrolysis/condensation reaction of tetraethoxysilane and then the PS nodules were dissolved in tetrahydrofuran (THF). PS bumps

remain at the bottom of the dimples, corresponding to the PS macromolecules covalently bonded to the silica surface thanks to the copolymerization of styrene and MMS-derived grafts [63]. The PS macromolecules were chemically modified for making them sticky and thus capable to develop covalent bonds or electrostatic interactions [64,65]. For that, they carried out a chloromethylation and subsequently an amination of the chloromethylated PS residue by simple nucleophilic substitution reactions. Later, Chomette *et al.* developed a general strategy to convert PS/silica multipods into gold/silica analogues. They used the aminated PS as a glue to stick gold nanoseeds and carried out their growth using formaldehyde as a reducing agent and a gold plating solution consisting of an $\text{Au}(\text{OH})_4^-$ complex generated in water from HAuCl_4 and K_2CO_3 . This strategy enabled to obtain clusters with large gold satellites (> 50 nm) (Figure 33D). Preliminary experiments were also carried out leading to gold dodecahedral clusters. However, the gold dodecahedral clusters purity and quantity weren't high enough to allow optical measurements.

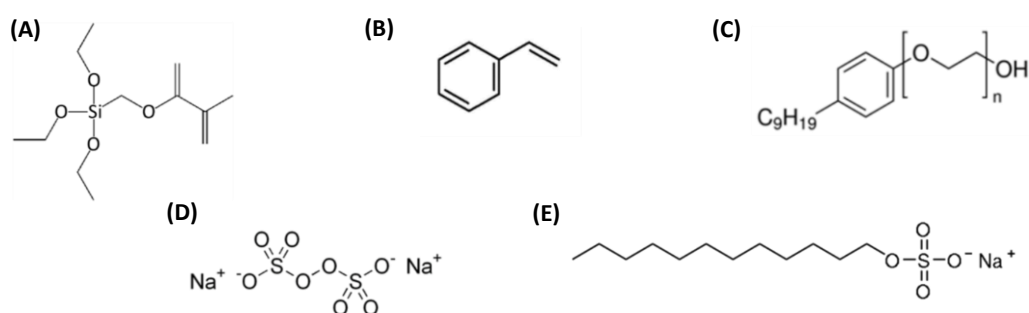


Figure 32: Chemical formulae of the main reagents used for getting silica PS/clusters through a seeded-growth emulsion polymerization: A) methacryloxymethyltriethoxysilane (MMS); B) styrene; C) Synperonic® NP 30; D) sodium persulfate and E) sodium dodecylsulfate (SDS) [61,66].

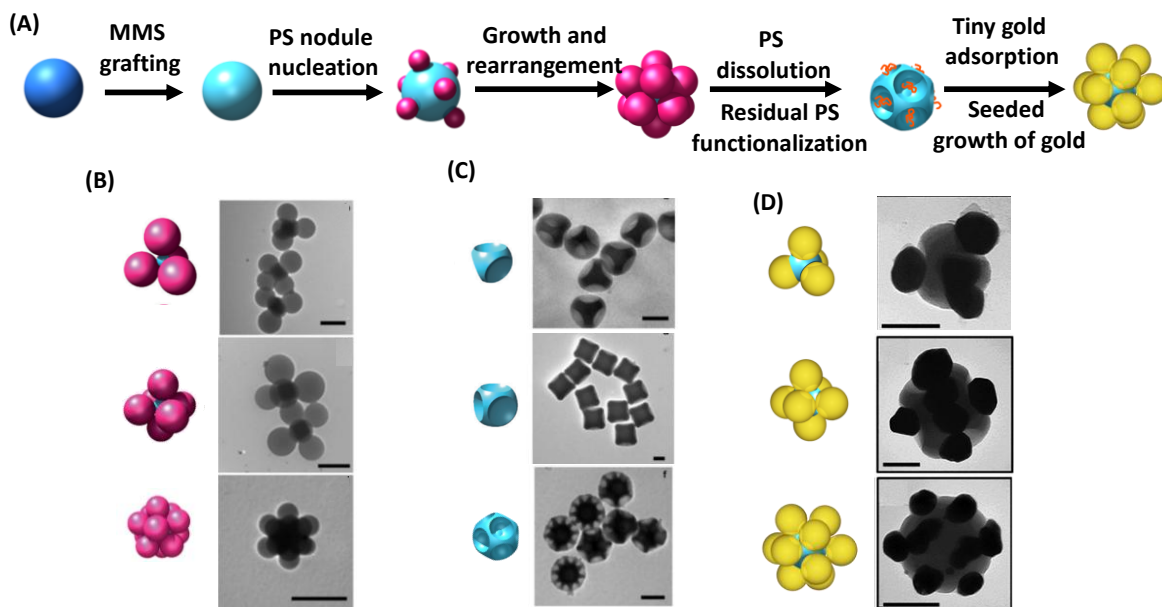


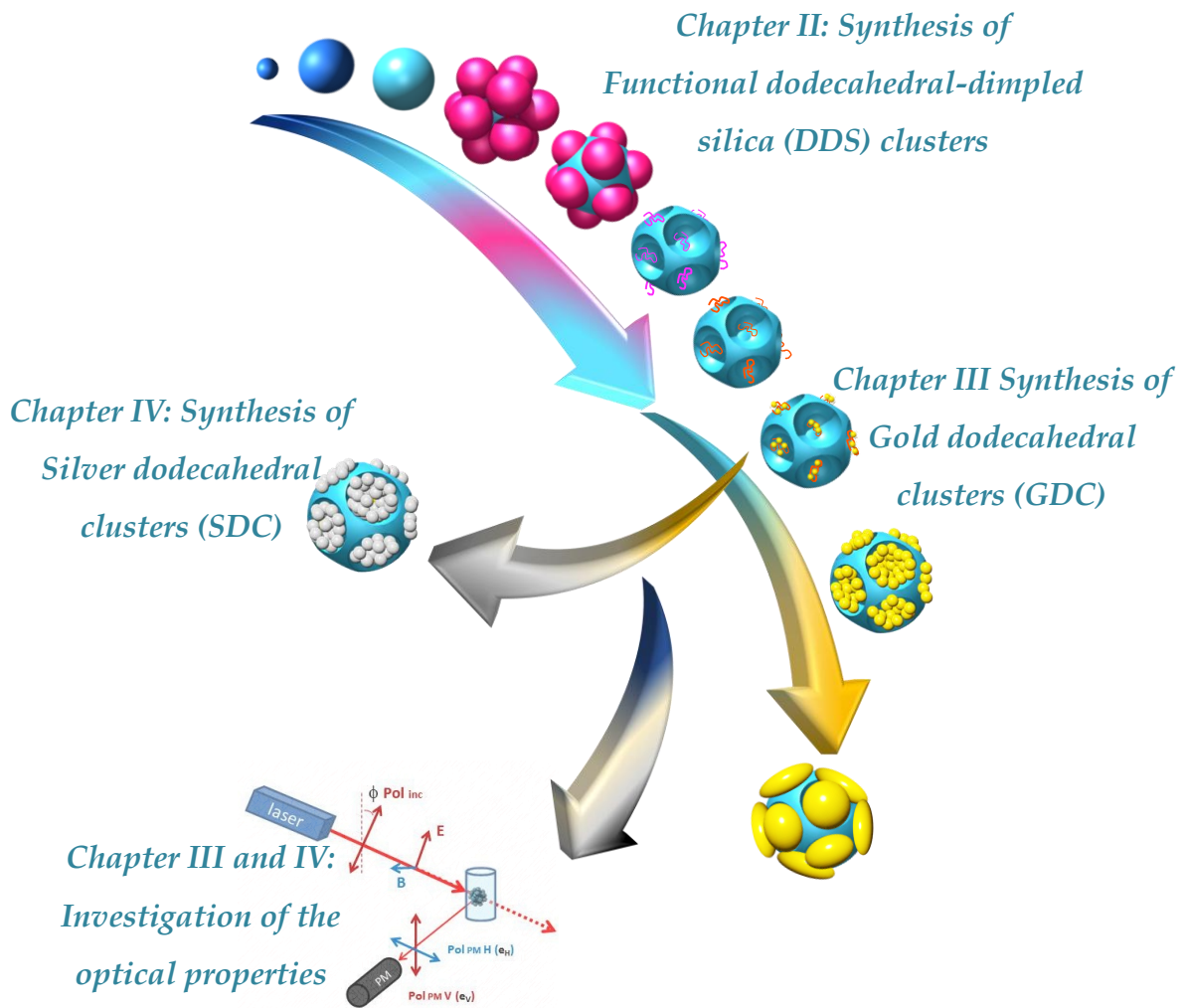
Figure 33: (A) Strategy of the fabrication of dodecapods PS/silica hybrid clusters from surface-modified silica seeds; TEM images of: (B) tetrapods, hexapods and dodecapods (from top to down); (C) silica particles with four, six, twelve dimples (from top to bottom); (D) gold tetrahedral, hexahedral and dodecahedral clusters (from top to bottom) (scale bars: 100 nm).

4. Conclusion and strategy

This state-of-the-art shows that only a few isotropic metallodielectric nanoresonators were reported up to now. Among the most efficient ones, raspberry-like NPs could be optimized by increasing the size of the plasmonic satellites and therefore decreasing their number while keeping an isotropic distribution. Dodecahedral arrangements combining twelve satellites are the optimal design. Several synthetic routes to get such plasmonic dodecahedral clusters were reported even if some of them didn't aim to generate metamaterial capabilities. Among them, only the route using the dimpled-silica NPs as scaffolds is the most interesting. It allows to control of the satellite number, the satellite size and the in-between gap, and the possibility of fabrication of these objects at the gram scale.

As a consequence, the objectives of this thesis was to (i) synthesize gold and silver dodecahedral clusters (named GDC and SDC) from functional dodecahedral dimpled-silica (DDS) NPs, (ii) study their optical properties as metafluids and (iii) assemble them in a 3D (bulk) or 2D material to get metamaterials or metasurfaces, respectively.

An overview of the overall strategy is presented in Scheme 1.



Scheme 1: The overall strategy guiding this study: the chapter II describes the synthesis of patchy particles; the chapters III and IV report the formation of plasmonic nanoclusters through a seeded-growth approach.

5. References

- [1] M. Born, E. Wolf, *Principles of optics: electromagnetic theory of propagation, interference and diffraction of light.*, Elsevier. 1980.
- [2] H. Fujiwara, *Spectroscopic ellipsometry: principles and applications*, John Wiley. 2007.
- [3] Y. Liu and X. Zhang, "Metamaterials: a new frontier of science and technology," *Chem. Soc. Rev.*, vol. 40, no. 5, pp. 2494–2507, 2011.
- [4] D. R. Smith, J. B. Pendry, and M. C. K. Wiltshire, "Metamaterials and Negative Refractive Index," *Science*, vol. 305, no. 5685, pp. 788 – 792, 2004.
- [5] M. Lapine and S. Tretyakov, "Contemporary notes on metamaterials," *IET Microwaves, Antennas Propag.*, vol. 1, no. 1, pp. 3–11, 2007.
- [6] A. Alu, N. Engheta, A. Erentok, and R. W. Ziolkowski, "Single-Negative, Double-Negative, and Low-index Metamaterials and their Electromagnetic Applications," *IEEE Antennas*

- Propag. Mag.*, vol. 49, no. 1, pp. 23–36, 2007.
- [7] V. G. Veselago, “The electrodynamics of substances with simultaneously negative values of ϵ and μ ,” *Sov. Phys. Uspekhi*, vol. 10, no. 4, p. 509, 1968.
- [8] J. B. Pendry, A. J. Holden, D. J. Robbins, and W. J. Stewart, “Magnetism from conductors and enhanced nonlinear phenomena,” *IEEE Trans. Microw. Theory Tech.*, vol. 47, no. 11, pp. 2075–2084, 1999.
- [9] R. A. Shelby, D. R. Smith, and S. Schultz, “Experimental Verification of a Negative Index of Refraction,” *Science*, vol. 292, no. 5514, pp. 77 – 79, 2001.
- [10] J. B. Pendry, “Negative Refraction Makes a Perfect Lens,” *Phys. Rev. Lett.*, vol. 85, no. 18, pp. 3966–3969, 2000.
- [11] N. Fang, H. Lee, C. Sun, and X. Zhang, “Diffraction-Limited Optical Imaging with a Silver Superlens,” *Science*, vol. 308, no. 5721, pp. 534– 537, 2005.
- [12] J. B. Pendry, D. Schurig, and D. R. Smith, “Controlling Electromagnetic Fields,” *Science*, vol. 312, no. 5781, pp. 1780 – 1782, 2006.
- [13] D. Schurig, J. J. Mock, B. J. Justice, S. A. Cummer, J. B. Pendry, A. F. Starr, and D. R. Smith, “Metamaterial Electromagnetic Cloak at Microwave Frequencies,” *Science*, vol. 314, no. 5801, pp. 977 – 980, 2006.
- [14] V. M. Shalaev, W. Cai, U. K. Chettiar, H.-K. Yuan, A. K. Sarychev, V. P. Drachev, and A. V. Kildishev, “Negative index of refraction in optical metamaterials,” *Opt. Lett.*, vol. 30, no. 24, pp. 3356–3358, 2005.
- [15] N. Liu, H. Guo, L. Fu, S. Kaiser, H. Schweizer, and H. Giessen, “Three-dimensional photonic metamaterials at optical frequencies,” *Nat. Mater.*, vol. 7, p. 31, 2007.
- [16] C. Enkrich, F. Pérez-Willard, D. Gerthsen, J. F. Zhou, T. Koschny, C. M. Soukoulis, M. Wegener, and S. Linden, “Focused-Ion-Beam Nanofabrication of Near-Infrared Magnetic Metamaterials,” *Adv. Mater.*, vol. 17, no. 21, pp. 2547–2549, 2005.
- [17] J. Valentine, S. Zhang, T. Zentgraf, E. Ulin-Avila, D. A. Genov, G. Bartal, and X. Zhang, “Three-dimensional optical metamaterial with a negative refractive index,” *Nature*, vol. 455, p. 376, 2008.
- [18] W. Cai and V. M. Shalaev, *Optical Metamaterials Fundamentals and Applications*, Springer, 2009.
- [19] Y. A. Urzhumov, G. Shvets, J. Fan, F. Capasso, D. Brandl, and P. Nordlander, “Plasmonic nanoclusters: a path towards negative-index metafluids,” *Opt. Express*, vol. 15, no. 21, pp. 14129–14145, 2007.
- [20] A. Alù, A. Salandrino, and N. Engheta, “Negative effective permeability and left-handed materials at optical frequencies,” *Opt. Express*, vol. 14, no. 4, pp. 1557–1567, 2006.
- [21] C. R. Simovski and S. A. Tretyakov, “Model of isotropic resonant magnetism in the visible range based on core-shell clusters,” *Phys. Rev. B - Condens. Matter Mater. Phys.*, vol. 79, no. 4, pp. 1–9, 2009.
- [22] C. Simovski, D. Morits, “Isotropic negative refractive index at near infrared,” *J. Opt.*, vol. 14, no. 12, p. 125102, 2012.
- [23] A. Vallecchi, M. Albani, and F. Capolino, “Collective electric and magnetic plasmonic resonances in spherical nanoclusters,” *Opt. Express*, vol. 19, no. 3, pp. 2754–2772, 2011.
- [24] S. Mühligh, A. Cunningham, S. Scheeler, C. Pacholski, T. Bürgi, C. Rockstuhl, and F. Lederer, “Self-Assembled Plasmonic Core–Shell Clusters with an Isotropic Magnetic Dipole Response in the Visible Range,” *ACS Nano*, vol. 5, no. 8, pp. 6586–6592, 2011.
- [25] J. Xue, C. Wang, and Z. Ma, “A facile method to prepare a series of SiO₂@Au core/shell

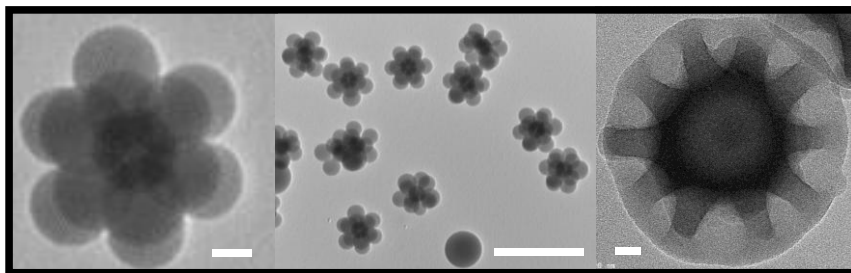
- structured nanoparticles,” *Mater. Chem. Phys.*, vol. 105, no. 2, pp. 419–425, 2007.
- [26] M. Nakamura and K. Ishimura, “Synthesis and Characterization of Organosilica Nanoparticles Prepared from 3-Mercaptopropyltrimethoxysilane as the Single Silica Source,” *J. Phys. Chem. C*, vol. 111, no. 51, pp. 18892–18898, 2007.
- [27] S. N. Sheikholeslami, H. Alaeian, A. L. Koh, and J. A. Dionne, “A Metafluid Exhibiting Strong Optical Magnetism,” *Nano Lett.*, vol. 13, no. 9, pp. 4137–4141, 2013.
- [28] V. Ponsinet, P. Barois, S. M. Gali, P. Richetti, J. B. Salmon, A. Vallecchi, M. Albani, A. Le Beulze, S. Gomez-Grana, E. Duguet, S. Mornet, and M. Treguer-Delapierre, “Resonant isotropic optical magnetism of plasmonic nanoclusters in visible light,” *Phys. Rev. B*, vol. 92, no. 22, p. 220414, 2015.
- [29] S. Gomez-Grana, A. Le Beulze, M. Treguer-Delapierre, S. Mornet, E. Duguet, E. Grana, E. Cloutet, G. Hadziioannou, J. Leng, J.-B. Salmon, V. G. Kravets, A. N. Grigorenko, N. A. Peyyety, V. Ponsinet, P. Richetti, A. Baron, D. Torrent, and P. Barois, “Hierarchical self-assembly of a bulk metamaterial enables isotropic magnetic permeability at optical frequencies,” *Mater. Horizons*, vol. 3, no. 6, pp. 596–601, 2016.
- [30] Z. Qian, S. P. Hastings, C. Li, B. Edward, C. K. McGinn, N. Engheta, Z. Fakhraai, and S.-J. Park, “Raspberry-like Metamolecules Exhibiting Strong Magnetic Resonances,” *ACS Nano*, vol. 9, no. 2, pp. 1263–1270, 2015.
- [31] C. Li, S. Lee, Z. Qian, C. Woods, S.-J. Park, and Z. Fakhraai, “Controlling Magnetic Dipole Resonance in Raspberry-like Metamolecules,” *J. Phys. Chem. C*, vol. 122, no. 12, pp. 6808–6817, 2018.
- [32] A. N. Grigorenko, A. K. Geim, H. F. Gleeson, Y. Zhang, A. A. Firsov, I. Y. Khrushchev, and J. Petrovic, “Nanofabricated media with negative permeability at visible frequencies,” vol. 438, pp. 335–338, 2005.
- [33] S. Linden, C. Enkrich, M. Wegener, J. Zhou, T. Koschny, and C. M. Soukoulis, “Magnetic Response of Metamaterials at 100 Terahertz,” *Science*, vol. 306, no. 5700, pp. 1351 – 1353, 2004.
- [34] J. Zhou, L. Zhang, G. Tuttle, T. Koschny, and C. M. Soukoulis, “Negative index materials using simple short wire pairs,” *Phys. Rev. B*, vol. 73, no. 4, p. 41101, 2006.
- [35] G. Dolling, M. Wegener, C. M. Soukoulis, and S. Linden, “Negative-index metamaterial at 780 nm wavelength,” *Opt. Lett.*, vol. 32, no. 1, pp. 53–55, 2007.
- [36] T. Xu, A. Agrawal, M. Abashin, K. J. Chau, and H. J. Lezec, “All-angle negative refraction and active flat lensing of ultraviolet light,” *Nature*, vol. 497, p. 470, 2013.
- [37] A. Vallecchi, M. Albani, and F. Capolino, “Effect of irregularities of nanosatellites position and size on collective electric and magnetic plasmonic resonances in spherical nanoclusters,” *Opt. Express*, vol. 21, no. 6, pp. 7667–7685, 2013.
- [38] C. F. Bohren and D. R. Huffman, *Absorption and Scattering of light by Small Particle*, Wiley-Inte. 1983.
- [39] J. Fontana, W. J. Dressick, J. Phelps, J. E. Johnson, R. W. Rendell, T. Sampson, B. R. Ratna, and C. M. Soto, “Nanoclusters: Virus-Templated Plasmonic Nanoclusters with Icosahedral Symmetry via Directed Self-Assembly (Small 15/2014),” *Small*, vol. 10, no. 15, p. 3196, 2014.
- [40] J. Johnson, T. Lin, and G. Lomonosoff, “Presentation of heterologous peptides on plant viruses: Genetics, Structure, and Function,” *Annu. Rev. Phytopathol.*, vol. 35, no. 1, pp. 67–86, 1997.
- [41] V. N. Manoharan, M. T. Elsesser, and D. J. Pine, “Dense Packing and Symmetry in Small Clusters of Microspheres,” *Science*, vol. 301, no. 5632, pp. 483 – 487, 2003.
- [42] B. R. Saunders and B. Vincent, “Microgel particles as model colloids: theory, properties and

- applications,” *Adv. Colloid Interface Sci.*, vol. 80, no. 1, pp. 1–25, 1999.
- [43] R. Hinton; M. Dobrota, *Density Gradient Centrifugation in Laboratory Techniques in Biochemistry and Molecular Biology*, vol. 6, part 1, Elsevier. 1976.
- [44] A. S. Urban, X. Shen, Y. Wang, N. Large, H. Wang, M. W. Knight, P. Nordlander, H. Chen, and N. J. Halas, “Three-Dimensional Plasmonic Nanoclusters,” *Nano Lett.*, vol. 13, no. 9, pp. 4399–4403, 2013.
- [45] Q. Yuan, J. Gu, Y. Zhao, L. Yao, Y. Guan, and Y. Zhang, “Synthesis of a Colloidal Molecule from Soft Microgel Spheres,” *ACS Macro Lett.*, vol. 5, no. 5, pp. 565–568, 2016.
- [46] R. H. Pelton and P. Chibante, “Preparation of aqueous latices with N-isopropylacrylamide,” *Colloids and Surfaces*, vol. 20, no. 3, pp. 247–256, 1986.
- [47] T.-S. Deng, J.-Y. Zhang, K.-T. Zhu, Q.-F. Zhang, and J.-L. Wu, “Highly monodisperse vinyl functionalized silica spheres and their self-assembled three-dimensional colloidal photonic crystals,” *Colloids Surfaces A Physicochem. Eng. Asp.*, vol. 356, no. 1, pp. 104–111, 2010.
- [48] S. L. Westcott, S. J. Oldenburg, T. R. Lee, and N. J. Halas, “Formation and Adsorption of Clusters of Gold Nanoparticles onto Functionalized Silica Nanoparticle Surfaces,” *Langmuir*, vol. 14, no. 19, pp. 5396–5401, 1998.
- [49] Y. Yamanoi, N. Shirahata, T. Yonezawa, N. Terasaki, N. Yamamoto, Y. Matsui, K. Nishio, H. Masuda, Y. Ikuhara, and H. Nishihara, “Detailed Structural Examinations of Covalently Immobilized Gold Nanoparticles onto Hydrogen-Terminated Silicon Surfaces,” *Chem. Eur. J.*, vol. 12, no. 1, pp. 314–323, 2005.
- [50] E. Winfree, F. Liu, L. A. Wenzler, and N. C. Seeman, “Design and self-assembly of two-dimensional DNA crystals,” *Nature*, vol. 394, p. 539, 1998.
- [51] H. Yan, S. H. Park, G. Finkelstein, J. H. Reif, and T. H. LaBean, “DNA-Templated Self-Assembly of Protein Arrays and Highly Conductive Nanowires,” *Science*, vol. 301, no. 5641, pp. 1882 – 1884, 2003.
- [52] P. W. K. Rothmund, “Folding DNA to create nanoscale shapes and patterns,” *Nature*, vol. 440, p. 297, 2006.
- [53] J. Chen and N. C. Seeman, “Synthesis from DNA of a molecule with the connectivity of a cube,” *Nature*, vol. 350, p. 631, 1991.
- [54] Y. Zhang and N. C. Seeman, “Construction of a DNA-Truncated Octahedron,” *J. Am. Chem. Soc.*, vol. 116, no. 5, pp. 1661–1669, 1994.
- [55] W. M. Shih, J. D. Quispe, and G. F. Joyce, “A 1.7-kilobase single-stranded DNA that folds into a nanoscale octahedron,” *Nature*, vol. 427, p. 618, 2004.
- [56] C. Zhang, M. Su, Y. He, X. Zhao, P. Fang, A. E. Ribbe, W. Jiang, and C. Mao, “Conformational flexibility facilitates self-assembly of complex DNA nanostructures,” *Proc. Natl. Acad. Sci.*, vol. 105, no. 31, pp. 10665 – 10669, 2008.
- [57] R. Veneziano, S. Ratanalert, K. Zhang, F. Zhang, H. Yan, W. Chiu, and M. Bathe, “Designer nanoscale DNA assemblies programmed from the top down,” *Science*, vol. 352, p. 1534, 2016.
- [58] K. F. Wagenbauer, C. Sigl, and H. Dietz, “Gigadalton-scale shape-programmable DNA assemblies,” *Nature*, vol. 552, p. 78, 2017.
- [59] Y. Tian, T. Wang, W. Liu, H. L. Xin, H. Li, Y. Ke, W. M. Shih, and O. Gang, “Prescribed nanoparticle cluster architectures and low-dimensional arrays built using octahedral DNA origami frames,” *Nat. Nanotechnol.*, vol. 10, p. 637, 2015.
- [60] A. Désert, C. Hubert, Z. Fu, L. Moulet, J. Majimel, P. Barboteau, A. Thill, M. Lansalot, E. Bourgeat-Lami, E. Duguet, and S. Ravaine, “Synthesis and Site-Specific Functionalization of Tetravalent, Hexavalent, and Dodecavalent Silica Particles,” *Angew. Chemie Int. Ed.*, vol. 52,

no. 42, pp. 11068–11072, 2013.

- [61] A. Désert, I. Chaduc, S. Fouilloux, J.-C. Taveau, O. Lambert, M. Lansalot, E. Bourgeat-Lami, A. Thill, O. Spalla, S. Ravaine, and E. Duguet, “High-yield preparation of polystyrene/silica clusters of controlled morphology,” *Polym. Chem.*, vol. 3, no. 5, pp. 1130–1132, 2012.
- [62] K. D. Hartlen, A. P. T. Athanasopoulos, and V. Kitaev, “Facile preparation of highly monodisperse small silica spheres (15 to >200 nm) suitable for colloidal templating and formation of ordered arrays,” *Langmuir*, vol. 24, no. 5, pp. 1714–1720, 2008.
- [63] C. Chomette, E. Duguet, S. Mornet, E. Yammine, V. N. Manoharan, N. B. Schade, C. Hubert, S. Ravaine, A. Perro, and M. Treguer-Delapierre, “Templated growth of gold satellites on dimpled silica cores,” *Faraday Discuss.*, vol. 191, pp. 105–116, 2016.
- [64] C. Chomette, “Thèse de l’université de Bordeaux: Design and synthesis of plasmonic meta-atoms from patchy particles,” 2015.
- [65] C. Chomette, M. Tréguer-Delapierre, N. B. Schade, V. N. Manoharan, O. Lambert, J.-C. Taveau, S. Ravaine, and E. Duguet, “Colloidal Alchemy: Conversion of Polystyrene Nanoclusters into Gold,” *ChemNanoMat*, vol. 3, no. 3, pp. 160–163, 2017.
- [66] A. Desert, “Thèse de l’Université Bordeaux 1: Colloïdes hybrides silice/polystyrène de morphologie contrôlée,” 2014.

Chapter II :
Synthesis of functional
dodecahedral-dimpled silica
nanoparticles from
PS/silica dodecapods



TEM images of PS/silica dodecapods (right and center) and silica dodecahedral-dimpled nanoparticles (left). Scale bars: 100 nm, 500 nm and 20 nm, respectively

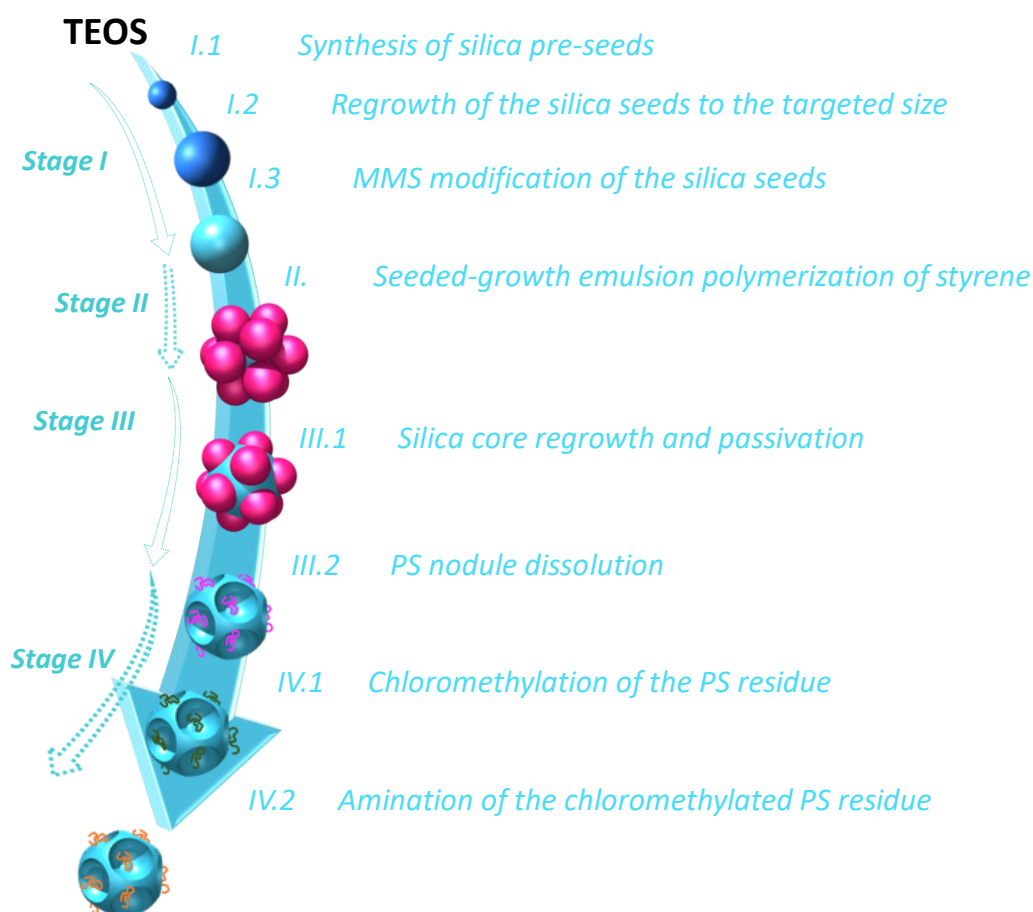
Introduction

In the previous chapter, we discussed about the synthesis pathways of well-controlled and well-defined dodecapod-like clusters highlighting the complexity of such syntheses. The approach that we chose is based on the seeded-growth emulsion polymerization route developed and optimized successively by S. Reculosa, A. Perro, D. Nguyen and A. Désert, successive PhD students at the university of Bordeaux [1-4]. S. Reculosa developed the pathway to synthesize PS/silica multipods, especially raspberry-like and monopod-like clusters [5,6]. However, it didn't provide well controlled shapes because the morphology yield was lower than 50 %. Later, A. Perro succeeded in controlling the number of PS nodules per silica particle from two to twelve nodules, but at the expense of quenching the polymerization progress at low monomer-to-polymer conversion (~30 %) [7]. Further, D. Nguyen carried out cryo-TEM experiments highlighting (i) the presence of small PS nuclei bound to the silica seeds in random arrangements from the beginning of the polymerization, and (ii) a decrease of $N_{\text{PS/silica}}$ and position optimization of the PS satellites as the polymerization runs and the satellites grow [8]. Those experiments also allowed to measure the contact-angle that the PS nodules form at the silica surface. Finally, A. Désert optimized the surface modification of the silica seeds and the polymerization recipe to achieve a complete monomer-to-polymer conversion within 6 h by adding sodium dodecylsulfate (SDS) as co-surfactant [9]. This leads to enhance the reaction kinetics, to reduce the size of the PS nodules and to get hexapods and tetrapods with a morphology yield over 80 %. He also extended this method to other morphologies such as dodecapods using silica seeds with diameter of 145 nm or 85 nm, achieving morphology yields of 45 % and 74 %, respectively [10]. Further, A. Désert reported that, by growing the silica core using a sol gel process and dissolving the PS nodules, silica particles with a specific number of dimples are obtained [11].

Later, C. Chomette reported that the PS residues covalently bonded at the bottom of the dimples may be readily modified to make them capable to develop covalent bonds or electrostatic interactions [12,13]. For this purpose, he carried out a chloromethylation and subsequently an amination of the chloromethylated PS residue by nucleophilic substitution reactions.

The dodecapods from 85-nm silica particles are indeed those we targeted to fabricate plasmonic dodecahedral clusters. Our ambition was to reach a higher morphology yield. Scheme 2 summarizes the overall synthetic pathway. The next sections describe the

preparation of the DDS clusters (stages I to III). Beyond the protocol previously developed by Désert *et al.*, we report our efforts for a better understanding and control of the final morphology of the PS/silica dodecapods. The last section concerns the stage IV that we visited again to make the dimples sticky with regard to gold, *i.e.* functionalized with amino groups.



Scheme 2: Multistep pathway to fabricate silica dodecahedral-dimpled (DDS) clusters with reactive PS chains at the bottom of the dimples.

1. Stage I: Synthesis of size-monodisperse silica seeds

The synthesis of highly size-monodisperse silica particles was carried out according to a seeded-growth strategy reported by Hartlen *et al.* [14] and optimized by Désert *et al.* [4]. The first step (stage I.1) consists in the synthesis of silica pre-seeds by the slow diffusion of TEOS through the interface of a biphasic medium (Protocol 1) [15]. The reaction is carried out in an L-arginine aqueous solution whose mild conditions allows to decrease the hydrolysis rate and to control the nucleation stage.

Protocol 1: Synthesis of the silica pre-seeds.

One hundred mL of 6 mM L-Arginine (99 %, Sigma- Aldrich) aqueous solution are poured in a 150-mL double-walled vial and equipped with a reflux condenser (Figure 34A). When the temperature is stabilized at 60°C, 10 mL of TEOS (99 %, Sigma- Aldrich) are added. The stirring setup is set to 150 rpm for a 3-cm cylindrical magnetic stirrer to generate a stable vortex and therefore an interface between both phases of constant surface area. The heating/stirring system is turned off when the TEOS upper phase has disappeared, typically, after two days. A small volume of the dispersion is collected in order to analyze the size of the pre-seeds by TEM and determine their concentration by the dry extract method.

The pre-seeds were characterized by transmission electron microscopy (TEM) (Figure 34B). Their average size was measured by statistical analysis using ImageJ software performed over 1000 particles and the polydispersity index (PDI) was calculated by

$$PDI = \frac{\overline{D_w}}{\overline{D_n}} = \frac{\sum n_i}{\sum n_i d_i} \cdot \frac{\sum n_i d_i^4}{\sum n_i d_i^3}$$

Equation 6

where $\overline{D_w}$ and $\overline{D_n}$ are the weight average and number average particle diameters, respectively. The typical average size of the pre-seeds was 26 nm with PDI of 1.02. The dry extract method allowed to determine the silica concentration: 27 g/L. In a given volume, the number of silica pre-seeds N_{Silica} was calculated from the silica concentration by assuming that the particles were spherical and their density was 2.2 g/cm³.

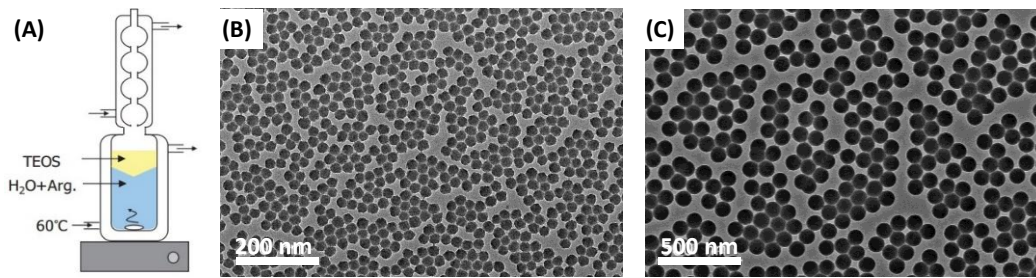


Figure 34: A) Scheme of the pre-seeds synthesis setup; TEM images of (B) the silica pre-seeds and (C) silica seeds.

The second step consists in the regrowth of these pre-seeds to the targeted diameter by the conventional Stöber's method (stage I.2). The amount of TEOS is critical to control the final size of the silica particles (Equation 7) and depends on the targeted diameter of the silica particles D_f , the average diameter of the silica pre-seeds D_i and the number of silica particles N_{Silica} contained in a given volume of pre-seeds dispersion. M_{TEOS} is the molecular weight of TEOS (208.32 g/mol); ρ_{TEOS} is the TEOS density (0.94 g/cm³) and M_{silica} is the molecular

weight of the SiO₂ monomer unit (60.08 g/mol). The regrowth stage was performed at room temperature in a typical Stöber medium made of a mixture of ethanol and ammonia (Protocol 2).

$$V_{TEOS} = \frac{M_{TEOS} \cdot \rho_{Silica}}{M_{Silica} \cdot \rho_{TEOS}} N_{Silica} \cdot \frac{\pi}{6} \cdot (D_f^3 - D_i^3) \quad \text{Equation 7}$$

Protocol 2: Regrowth of the silica pre-seeds

In a 1L round bottom flask surmounted by a bubbler, 455 mL of ethanol (99%), 35 mL of ammonia (28-30 %, J-T Baker) corresponding to [NH₃] = 3 M and 10 mL of aqueous dispersion of pre-seeds were added and stirred. The proper volume of TEOS calculated by Equation 7 is added to the solution with a syringe pump at the rate of 0.5 mL/h. The average size of seeds is determined by ImageJ analysis of the TEM images and the concentration of the dispersion is determined by the dried extracts method.

Targeting a final diameter of 85 nm, the analysis of the TEM images gave an average size of the particles of 90 nm with PDI of 1.003 (Figure 34C).

Further, in order to promote the nucleation and growth of the PS nodules, the surface of the silica seeds shall be made organophilic enough through the grafting of methacryloxymethyl groups from methacryloxytrialkoxysilane (MMS) coupling agent (Figure 35).¹

Désert *et al.* reported that a nominal surface density of 0.5 molecule/nm² of silica surface is the optimal value to get PS/silica multipod-like clusters with the expected contact angle [9]. Indeed, a lower value leads to unstable clusters, *e.g.* PS nodules falling down on the TEM grids, and a higher value leads to silica cores more or less perfectly embedded in a continuous PS shell [16]. The required MMS amount was calculated by Equation 8 and grafted according to Protocol 3.

$$V_{MMS} = \frac{6 \cdot d_{MMS} \cdot M_{MMS} \cdot V_{silica} \cdot C_{silica}}{N_A \cdot \rho_{MMS} \cdot \rho_{silica} \cdot D_{silica}} \quad \text{Equation 8}$$

where d_{MMS} is the surface grafting density of MMS, M_{MMS} is the molar mass of MMS (262.37 g/mol for methacryloxymethyltriethoxysilane and 220.3 g/mol for methacryloxymethyltrimethoxysilane), ρ_{MMS} is the MMS density (0.998 g/cm³), V_{silica} and

¹ Note: in this work, the coupling agent used was the methacryloxymethyltrimethoxysilane instead of the methacryloxymethyltriethoxysilane used by Désert *et al.* It may exist some differences concerning their reactivity just when the grafting to the silica surface occurs, but as soon as the alkoxy groups have left the methacryloxymethyl grafts are expected to be strictly identical.

C_{silica} are the volume and concentration of the silica seeds suspension, respectively, D_{silica} is the diameter of the silica seeds, and N_A is the Avogadro's number.

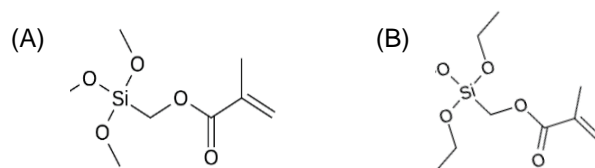


Figure 35: Chemical formula of the MMS coupling agents: (A) methacryloxymethyltrimethoxysilane and (B) methacryloxymethyltriethoxysilane.

Protocol 3: Functionalization of the silica seeds by MMS.

A volume V_{silica} of the hydro-alcoholic dispersion of the silica seeds obtained after the Protocol 2 is added in a round bottom flask and stirred. The setup is surmounted with a condenser. In this study, the grafting rate of MMS was fixed at 0.5 function/nm². The volume of MMS, calculated by Equation 8, is added to the mixture and stirred at room temperature for 3 h, then the temperature is increased at 90°C for 1 h under reflux of ethanol. The excess ammonium hydroxide was removed from the reacting medium by a rotary evaporator and the silica particles were transferred into Milli-Q® water. Further, the particles were purified by dialysis against water until neutral pH in order to remove the remaining reactants.

There is no specific characterization at the end of this step: the MMS is supposed to be grafted in a completed way and the surface density is therefore considered to be the nominal surface density. The success of this stage is indirectly checked by the success of the following stage. Table 1 summarizes the physico-chemical features of the four batches of the silica seeds prepared for this study.

Table 1: Summary of the experimental conditions of the silica pre-seeds and seeds synthesis and physico-chemical features of the four batches of silica seeds (the targeted diameter of the silica seeds was 85 nm)

Silica pre-seeds				Silica seeds				
V_{TEOS} (mL)	D_{silica} (nm)	PDI	C_{silica} (part./L)	V_{TEOS} (mL)	D_{silica} (nm)	PDI	C_{silica} (part./L)	Seed batch number
10	27	1.01	1.2×10^{18}	31	92	1.001	1.6×10^{16}	I
				31	90	1.003	1.5×10^{16}	II
10	26	1.02	1.3×10^{18}	33	89	1.001	1.3×10^{16}	III
				33	90	1.003	1.4×10^{16}	IV

2. Stage II: Synthesis of PS/silica dodecapods by seeded-growth emulsion polymerization

2.1 Description of the reference experiment of Désert *et al.* [10]

The multipod-like silica/PS clusters are synthesized by seeded-growth emulsion polymerization of styrene. Briefly, the emulsion polymerization is defined as a free-radical polymerization in a direct emulsion made of water, monomer and surfactant. When introduced above the critical micellar concentration, the surfactant molecules form micelles. When the organic monomer is added, the monomer is mainly contained in the droplets, but a fraction of the molecules diffuses through the water phase and swells the surfactant micelles. The polymerization starts with the addition of a water-soluble initiator and its thermal decomposition into free-radicals. By meeting the monomer molecules, active centers are generated, become more and more hydrophobic as the monomer addition and are finally captured by the micelles where the stocked monomer is polymerized according to the conventional propagation and termination stages. The micelles are permanently fed in monomer by diffusion from the reservoir droplets. From a colloidal point of view, the micelles grow and become polymer particles stabilized by the surfactant molecules and are generally called “latex” particles. It may be mentioned that (i) the air oxygen is an inhibitor for the polymerization and shall be removed from the reactor and (ii) when the monomer-to-polymer conversion increases from 20 to 50 %, the growing polymer particles are stickier and some coalescence phenomena are generally observed during this period.

Using seeds, *i.e.* the MMS-modified silica particles, is the opportunity for the latex particles to nucleate preferentially at their surface. For getting regular multipod-like silica/PS clusters, it was shown that the nature of the surfactant molecules is critical and that optimal results are obtained by using a mixture of Synperonic[®] NP 30 (non-ionic surfactant) and SDS (anionic surfactant) [9]. The latter boosts the polymerization reaction because it promotes the nucleation stage and therefore leads to more numerous but smaller PS particles. But used solely, it is not capable to control the cluster morphology [17].

Protocol 4: Synthesis of dodecapod-like silica/PS clusters.

In a 250-mL three-neck flask, equipped with a stirring anchor and a condenser itself surmounted by a bubbler, 50 mL of an aqueous dispersion made of amounts of MMS-functionalized silica seeds ($7.3 \cdot 10^{15}$ part./L) previously sonicated for 10 min, NP30 (Sigma-Aldrich) and SDS (Sigma-Aldrich) mixture (3 g/L including 5 wt.% of SDS) are introduced and deaerated with nitrogen for 1 h. The stirring speed is set at 170 rpm. Then, 45 g/L of styrene (99 % Sigma-Aldrich) are added and the stirring speed is

momentarily increased to 250 rpm for 15 min. The nitrogen flux is reduced in order to keep a low over-pressure. The temperature is increased at 70°C with a thermostated oil bath. Then, 1 mL of an aqueous solution previously nitrogen-degassed and containing 25 mg of sodium persulfate (99 %, Sigma Aldrich) is added. The polymerization is performed for 6 h. Then, the monomer-to-polymer conversion is measured by the dried extracts method.

Following this method, Désert *et al.* obtained 74 % of dodecapods with by-products such as pentapods/hexapods (4 %), octopods (5 %), nonapods (5 %), decapods (6 %) and hendecapods (5 %) [10].

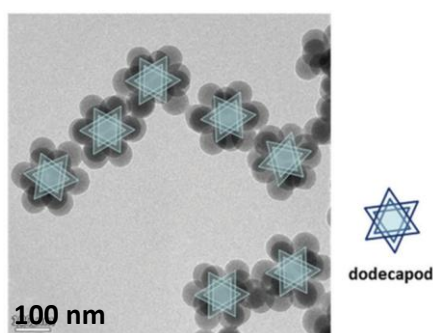


Figure 36: Typical TEM image of the dodecapods obtained by Désert *et al.* from silica seeds with a diameter of 85 nm [10].

2.2 The Thill's model to rationalize the nucleation and growth of PS nodules onto silica seeds

In order to understand and then control the growth process of the PS satellites onto the silica seeds, A. Thill developed a simulation tool whose adjustable parameters are close to those of the emulsion polymerization. Digital and chemical experiments were compared and allowed to rationalize the process [10,18]. The Thill's model is based on three main simplifying assumptions:

- every attached and free PS particle had initially nucleated and begun to grow onto the silica seeds surface in agreement with the heterogeneous nucleation regime;
- every PS nuclei was initially randomly distributed on the silica seeds and grew at the same surface rate;
- the growth rate of the nodules is not strongly affected by the fact they are attached to or detached from the seeds.

This model considers that when two growing PS satellites come into contact, one pushes the other one on the seed surface to continue to grow. Therefore, if the silica surface becomes too crowded for further motion, two mechanisms can stem from that: (i) two PS satellites merge in a larger one by coalescence (with a probability P_C) or (ii) one is expelled from the

silica surface and continue to grow independently becoming a free PS latex particle (with a probability $1 - P_C$) (Figure 37A). From these digital experiments, a R_V vs. $N_{PS/silica}$ diagram, called here Thill's diagram, was drawn showing the existence domain of the PS/silica clusters where R_V is the PS-to-silica volume ratio and $N_{PS/silica}$ is the number of PS satellites per silica seed (Figure 37B). Typically, in a production batch of PS/silica clusters, every cluster arises from the bottom of the existence domain along vertical lines corresponding to the number of initially growing PS nodules $N_{PS/silica}^0$. From that, two situations can occur:

- (i) if the possibility of merging or losing PS nodules is neglected, it “climbs” this line, along which it stops as soon as the growth stage, *i.e.* the polymerization reaction, is completed;
- (ii) if the geometrical boundary is reached, it implies that the PS nodules have become too bulky and therefore, for ensuring their further growth, the value of $N_{PS/silica}$ shall be reduced by at least one unit. Therefore, expulsion from the surface or coalescence phenomenon can occur which gives rise to free PS particles or polydisperse PS satellites, respectively, and the growth is extended along a vertical line corresponding to a smaller $N_{PS/silica}$ value.

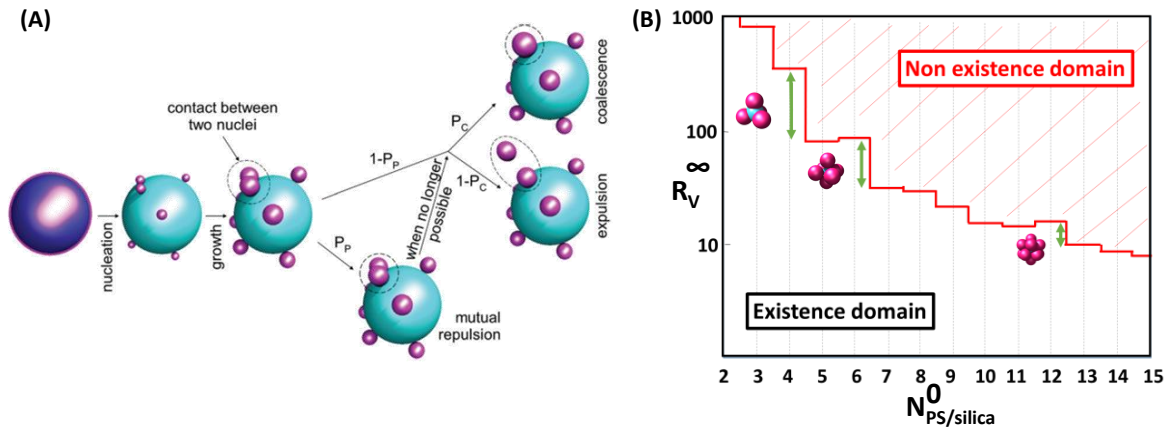


Figure 37: (A) Rules of the Thill's model for the nucleation and growth of the PS nodules; (B) Existence domain of PS/silica clusters expressed in the PS-to-silica ratio R_V as a function of $N_{PS/silica}^0$; the green arrows show that tetrapod, hexapod and dodecapod are the morphologies for which the exclusive existence domains are the largest ones. Nevertheless, the synthesis of dodecapods represents a challenging task comparing to tetrapods and hexapods.

The final y axis position, *i.e.* R_V^∞ , represents the PS-to-silica volume ratio at the end of the polymerization and may be calculated as a function of the experimental parameters thanks to Equation 9:

$$R_V^\infty = \frac{[styrene]_0 \cdot (styrene\text{-to-polystyrene conversion})^\infty}{d_{PS}} \frac{6}{\pi \cdot N_{silica} \cdot (D_{silica})^3} \quad \text{Equation 9}$$

where $[styrene]_0$ is the initial styrene concentration, and d_{PS} is the PS density (1.05 g/cm^3).

However, in the case where the amount of free PS particles is not negligible, R_V^∞ is necessarily over-estimated and an alternative value may be calculated from the geometrical dimensions (extracted from TEM images) of the targeted cluster $R_V^{\infty local}$, defined by Equation 10 in the specific case of a dodecapod:

$$R_V^{\infty local} = \frac{12 \cdot D_{PS}^3}{D_{silica}^3} \quad \text{Equation 10}$$

Lastly, the initial x axis position, *i.e.* $N_{PS/silica}^0$, may be estimated by Equation 11 considering the smallest isolated PS particles of size $D_{free PS}^\infty$ observed on the TEM grids assumed as having been expelled from a silica seed upon approaching the steric hindrance boundary [10]:

$$N_{PS/silica}^0 = R_V^\infty \cdot \left(\frac{D_{silica}}{D_{free PS}^\infty} \right)^3 \quad \text{Equation 11}$$

According to Désert *et al.*, 74 % of dodecapods can be achieved [10]. In order to improve the morphology dodecapods yield, several parameters can be varied. Typically, the adjustable experimental parameters are: (i) the surfactant concentration that should allow to control P_C , (ii) SDS fraction for controlling D_{PS} , (iii) $[silica]$ and $[styrene]_0$ for controlling R_V^∞ and (iv) $[silica]$ for controlling $N_{PS/silica}$.

2.3 Robustness of the dodecapods synthesis

Because the dodecapod synthesis reported by Désert *et al.* had been run once, we first decided to check the reproducibility and repeatability of the Protocol 4 [10]. Six batches of PS/silica clusters were so-prepared and characterized by TEM with statistical analyses of the images (without software help) carried out from 200-500 particles. Multi-silica clusters were also taken into account for the statistics. It corresponds to larger clusters made of two or three aggregated silica cores, which can stem from an imperfect initial dispersion of silica seeds or an unwanted inter-cluster aggregation during the polymerization process. It can be mentioned that TEM is a suitable tool to determine the PS nodules number thanks to the difference of contrast between silica and polystyrene. However, the identification of the dodecapods is particularly tricky because of the large number of PS satellites and the same size range of PS satellites and silica cores. The features of the six dodecapod batches and their statistical morphological analysis are summarized in Table 2, and Figure 38A represents a typical TEM image of the as-obtained dodecapods.

Table 2: Morphology and geometrical parameters of the PS/silica clusters obtained after the following conditions: preliminary sonication time of the seed dispersion = 10 min; [styrene]₀ = 45 g/L ; [Na₂S₂O₈]₀ = 0.5 g/L; [surfactant] = 3 g/L (including 5 wt.% of SDS); [silica] = 7.3.10¹⁵ part./L and d_{MMS} = 0.5 function per nm².

		Entry	# 1	# 2	# 3	# 4	# 5	# 6
Experimental conditions	Seed batch number		I	I	I	I	II	II
	Age of the seeds (days)		14	15	18	19	44	44
	Monomer-to-polymer conversion (%)		83	88	82	82	80	89
	R_V^∞		14.5	14.2	13.6	13.4	12.9	14.4
	$R_V^{\infty local}$		13.4	13.1	12.5	11.8	12.4	12.2
Final batch composition in clusters	% Hexapods		14	7	22		13	3
	% Octopods		15	8	14	8	14	9
	% Nonapods		10	11	7	10	11	10
	% Decapods			20	5	9		12
	% Hendecapods		5	4	3	3		4
	% Dodecapods		54	43	49	56	53	50
	% Multi-silica clusters		2	7		14	8	11
	Unexpected morphologies		*		*	*		
	D _{PS} (nm) on dodecapods		114	90	111	106	121	118
	PDI of D _{PS} on dodecapods		1.12	1.02	1.21	1.73	1.02	1.01
free PS	Estimated amount		+	+	ε	++	ε	++
	D _{free PS} (nm)		119	111	107	110	129	123
	N ⁰ _{PS/silica}		14.6	14.7	13.7	14.6	14.3	14.8

* some PS microparticles were also observed

Table 2 evidenced that the main morphologies obtained are systematically dodecapods with yields between 43 and 56 % that is a good sign for the robustness of the experiment. Nevertheless, the variability is higher on the nature and proportions of the by-products, and more importantly the morphology yield is not as high as reported by Désert *et al.* (74 % of dodecapods) [10]. Moreover, TEM images reveal the presence of size-polydisperse PS satellites, which probably arise from the coalescence of some PS satellites during their growth. This phenomenon seems to be accentuated for the by-products: for instance in batch # 2, the average size of the PS satellites is 90 nm (PDI = 1.02) for dodecapods vs. 109 nm (PDI = 1.12) for octopods (Figure 38A2). Lastly, R_V^∞ and $R_V^{\infty local}$ values are quite close to each other which is consistent with the low amount of free PS particles. This confirms that coalescence and expulsion phenomena coexist.

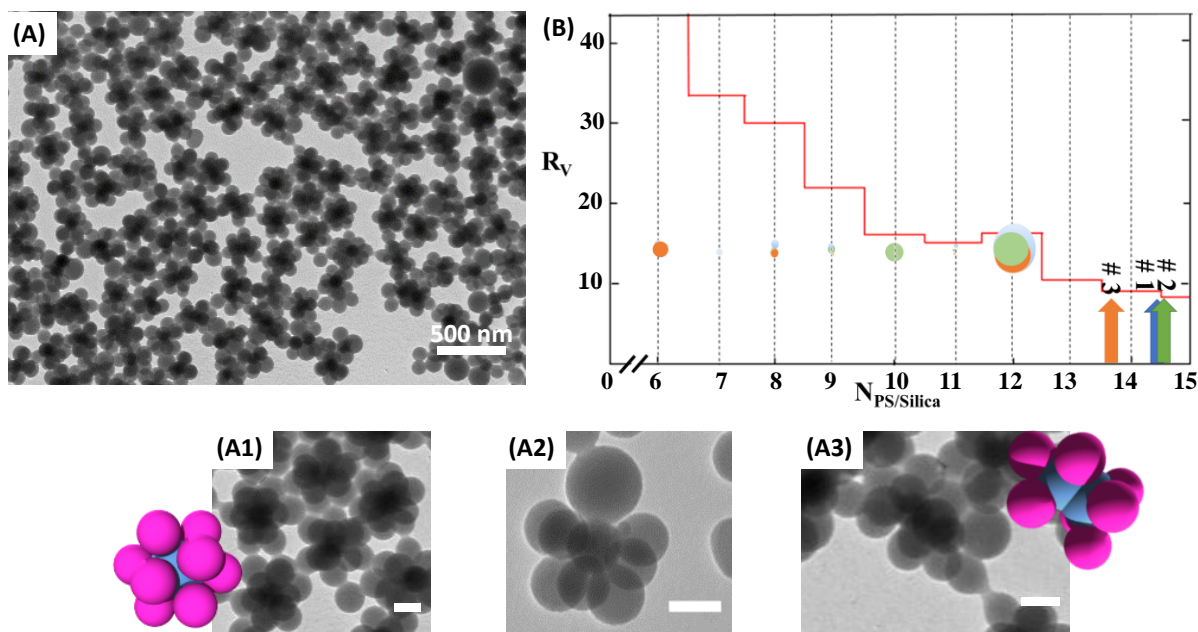


Figure 38: (A) Typical TEM image of the PS/silica dodecapods (experiments #1) ; Zoom of: (A1) a dodecapod, (A2) an octopod, (A3) a multi-silica cluster ; (scale bar: 100 nm); (B) Plot of the cluster composition of the experimental batches (coloured spots whose diameter is proportional to the fraction of the corresponding cluster) on the Thill's diagram using the typical protocol of Désert *et al.*[10].

The results of the experiments #1, #2 and #3 were reported on the Thill's diagram as spherical spots whose diameter is proportional to the fraction of the different clusters in each batch (Figure 38B). The value of $N_{PS/silica}^0$ was labelled by an arrow of the same color arising from the bottom of the diagram. Whatever the experiments, the average value of $N_{PS/silica}^0$ is close to 14 (Table 2). It means that most of the obtained dodecapods are the results of a geometrical refinement, *i.e.* clusters with more than 12 PS satellites that lost some of them when reaching the geometrical boundary. This is consistent with the size polydispersity of the PS satellites and the presence of free PS latex particles. But the coexistence of clusters with less than 12 satellites (from undecapods to hexapods) means that the polydispersity on $N_{PS/silica}^0$ is real and high, leading only to a partial geometrical refinement (Figure 39B). Therefore a way to maximize the dodecapod yield would be to make $N_{PS/silica}^0$ as high as possible with a minimal value of 12 and to stop the PS satellite growth up to the exclusive existence domains of the dodecapods, *i.e.* $10.2 \leq R_V^\infty \leq 16.3$ (Figure 39C). This could be achieved by increasing the number of PS nuclei on each silica seed.

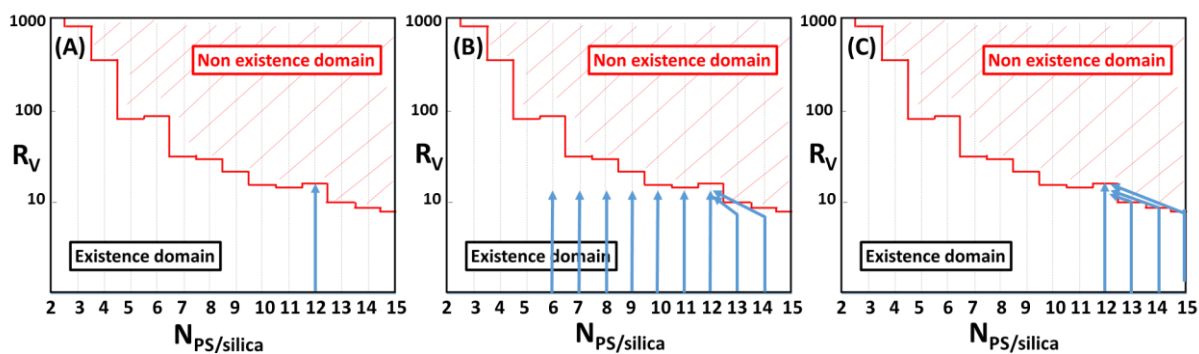


Figure 39: Thill's diagram showing the different strategies to get dodecapods. (A) The ideal conditions where all the clusters present twelve growing PS satellites and the reaction is stopped before reaching the geometrical boundary, i.e. R_V^∞ lower than 16.3. (B) The real conditions where a dispersion on $N_{PS/silica}^0$ exists and the geometrical refinement is partial. (C) The optimal conditions where the dispersion on $N_{PS/silica}^0$ exists but the smallest value of $N_{PS/silica}^0$ is 12 for promoting a full geometrical refinement.

That is why we first studied the influence of the composition of the surfactant mixture and its proportion with regard to the monomer. In order to decrease the amount of multi-silica clusters, we also tried to improve the dispersion state of the silica seeds.

2.4 Influence of the surfactant mixture composition and proportion with regard to the monomer

The surfactant is known to stabilize the PS nuclei and it was shown that SDS is particularly efficient for this purpose, because the higher the SDS fraction the smaller and the more numerous the PS particles [10]. The Protocol 4 was repeated by varying the SDS fraction and the total concentration of surfactants (Table 3).

Table 3: Morphology and geometrical parameters of the PS/silica clusters as a function of the surfactant mixture composition and concentration obtained after the following conditions: [styrene]₀ = 45 g/L ; [Na₂S₂O₈]₀ = 0.5 g/L; [silica] = 7.3.10¹⁵ part./L and d_{MMS} = 0.5 function per nm².

Entry		# 7	# 8	# 9	# 10	# 11	# 12	# 13
Experimental conditions	Seed batch number	II	II	II	IV	IV	II	II
	Age of the seeds (days)	20	28	34	7	13	57	62
	Preliminary sonication time of the silica seed dispersion (min)	10	10	10	10	10	30	30*
	[surfactant] (g/L)	3	3	3	4	4	4	4
	Symperonic® NP30 / SDS mass ratio	93/7	93/7	93/7	93/7	93/7	93/7	93/7
	Monomer-to-polymer conversion (%)	81	82	85	80	82	88	94
	R _v [∞]	13.1	13.3	13.7	12.9	13.2	14.2	15.2
	R _v ^{∞local}	12.8	13.2	13.5	11.2	12.3	12.1	11.9
Final batch composition in clusters	% Hexapods	11	6	6			9	
	% Octopods	15	15	19	3	5	9	1
	% Nonapods	17	15	12	6	6	5	2
	% Decapods		8		6	8	2	1
	% Hendecapods						3	2
	% Dodecapods	55	54	58	75	73	37	46
	% Multi-silica clusters	2	2	6	10	8	35	48
	D _{PS} (nm) on dodecapods	97	95	95	81	78	85	82
	PDI of D _{PS} on dodecapods	1.02	1.03	1.04	1.001	1.002	1.002	1.005
	free PS	Estimated amount	ε	ε	ε	+	+	+++
D _{free PS} (nm)		92	92	93	82	80	80	82
N ⁰ _{PS/silica}		14.9	14.6	15.7	25	22	19	21

* for this experiment, the sonication was performed in the presence of the surfactant mixture

2.4.1 Influence of the SDS fraction

Our first experiments consisted in increasing the SDS fraction from 5 to 7 wt.% (Table 3 entry #7 to #9 to be compared to Table1 entries #1 to #6) with the objective to promote the nucleation of PS particles and therefore to increase $N_{PS/silica}^0$. Considering averaged values, we observe indeed an increase of $N_{PS/silica}^0$ from 14.4 to 15.1 combined to a decrease of D_{PS} on the dodecapods from 110 to 96 nm and lower PDI values. Nevertheless, this didn't lead to an increase of the dodecapod yield which remained about 56 %.

2.4.2 Influence of the total concentration of surfactant

Experiments corresponding to entries from #10 to #13 were performed with a total concentration of surfactants of 4 g/L (vs. 3 g/L previously) keeping constant the fraction of SDS to 7 wt.%. The experiment #10 showed that a dodecapod yield of 75 % may be achieved with D_{PS} on dodecapods close to 80 nm. This corresponds to an increase of $N_{PS/silica}^0$ from 15.1 to 25 and this is consistent with the strategy envisioned on Figure 39C even if some

octopods, nonapods and decapods are still present (Figure 40). The repeatability of this experiment was checked and confirmed (Experiment #11).

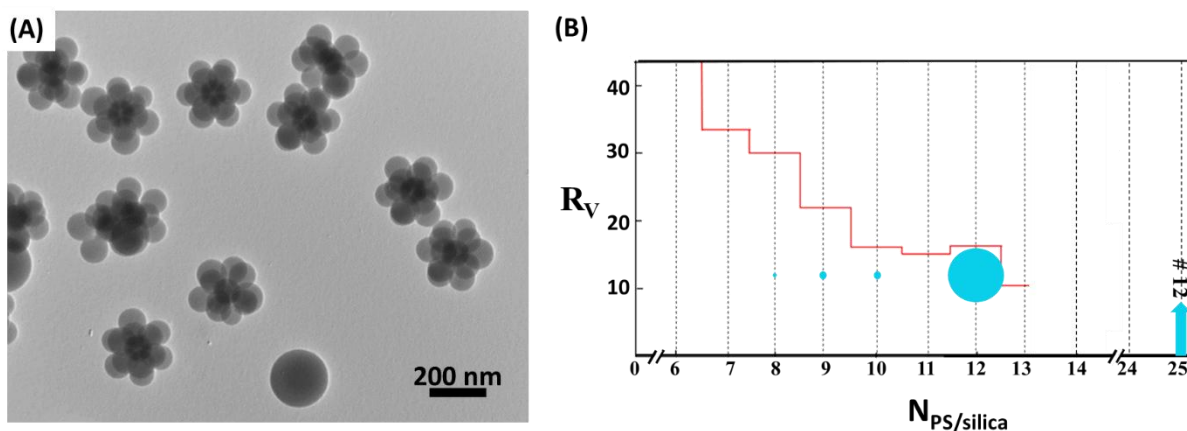


Figure 40: (A) Typical TEM image of the PS/ Silica dodecapods from batch #10; (B) Plot of the cluster composition of the experimental batches (coloured spots whose diameter is proportional to the fraction of the corresponding cluster) on the Thill's diagram using the typical protocol of Désert *et al.* [10].

2.4.3 Influence of the sonication protocol of the silica seed dispersion

Because in the Experiment #10 the main by-products are the multi-silica clusters (10 %), we studied the influence of the sonication protocol assuming that their presence could result from a bad dispersion of the silica seeds before the emulsion polymerization stage or a destabilization at this time. Experiments #12 and #13 were performed with a sonication time increased from 10 to 30 min. We observed unexpectedly an increase of the fraction of the multi-silica clusters to 35 %, and even 48 % when the protocol was applied after the addition of the surfactant mixture (Experiment #13, Figure 41).

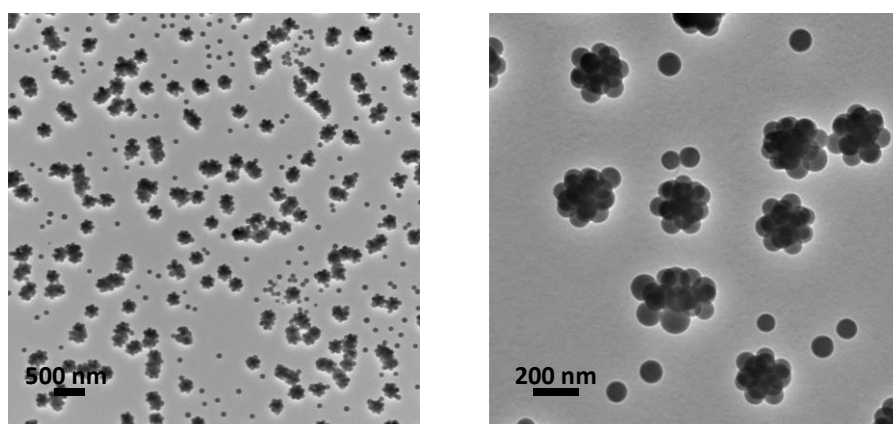


Figure 41: Typical TEM images of the PS/silica clusters in the batch #12 (*cf.* Table 2).

In general, the aggregation of particles can be explained by the potential curve reported by Derjaguin-Landau-Verwey-Overbeek (DLVO) theory representing the long-range, attractive van der Waals interaction (V_A) and the short-range double-layer repulsion (V_R) and V_T the total energy potential between particles corresponding to the sum of both interactions V_R and

V_A (Figure 42B) [19,20]. When two particles tend to be close to each other, an attraction force (Van der Waals) appears between two particles and a primary minimum occurs in the total potential energy. Therefore, collisions between particles will occur giving rise to agglomeration of these particles. By contrast, when the distance between two particles is increased, electrostatic repulsions appear between these two particles leading to a maximum (called repulsive barrier) in the potential curve. Therefore, in order to improve the dispersion of the silica seeds before the polymerization an external force to overcome the van der Waals attractions forces between the silica particles should be applied. Ultrasonication method can be used to disperse agglomerates, as it can impose a force on it. The applied force should be strong enough to break the aggregates.

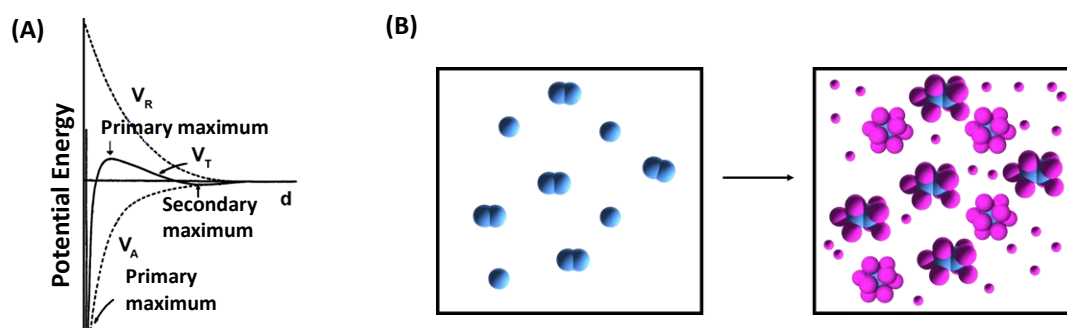


Figure 42: (A) Schematic scheme of a typical DLVO potential, where V_A is due to the attractive Van Der Waals interaction and V_R is due to the electrostatic repulsion; (B) Schematic illustration showing how: (i) Aggregates of silica are formed owing to collision between silica particles, (ii) Emulsion polymerization occurs around the multi-silica aggregates and single silica seeds.

Nevertheless, it seems that in our situation the sonication time and the presence of the surfactants promote the formation of the multi-silica clusters. Several articles confirm that ultrasonication method can also lead to particle aggregation [21-23]. Zhong *et al.* indeed reported that the aggregation of gold nanoparticles can occur from ultrasonication [22]. Fan *et al.* were able to synthesize monodisperse selenium colloidal dimers and trimers by controlling the sonication time [23]. Those studies are consistent with our results. Indeed, the increase of silica aggregates with sonication time can be explained based on the various phenomena associated with cavitation. Cavitation is defined as the formation, growth and subsequent implosion of microbubbles during sonication [24]. First, cavitation leads to acoustic streaming and turbulent fluid movement in the medium which drive the transport and contact of the particles [25]. Suslick *et al.* also showed that the particle aggregation due to cavitation is primarily due to high speed interparticle collisions [26,27]. Additionally, Radziuk *et al.* studied the sonication effect toward gold nanoparticles in pure water and in presence of SDS or cationic dodecyl amine in water [21]. They reported that long time sonication could lead

the particles to aggregate. However, in our case, we observe an increase of the particle aggregation in presence of surfactants which is not consistent with Radziuk's investigations. Moreover, Mandzy *et al.* studied the long-term stability of nanoparticle dispersions, *e.g.* titanium dioxide, and reported that breakage of agglomerates is hardly reached by ultrasonication method [28]. They observed that ultrasonication caused indeed the breakage of the agglomerates, but shortly after the end of this process they observed the re-aggregation of the particles.

In our situation, the mechanism of formation of the aggregates under sonication is not elucidated. A comprehensive study would necessitate to follow the aggregation of silica nanoparticles in the storage conditions and to understand the interactions of the surfactant molecules with the silica surface knowing that it was incompletely modified with MMS a quite hydrophobic agent. Because it wasn't the main purpose of this work, we didn't initiate such a long study. However, a preliminary sonication time is required to disperse the particles in the medium. Additional experiments were carried out varying the sonication time from 1 min to 10 min, and no increase of the multi-silica clusters were observed. Thus, a sonication time of 10 min is kept for the overall emulsion polymerization experiments. Nevertheless, without performing any extra experiments, we looked for a possible correlation between the proportion of the multi-silica clusters and the age of the seed dispersions used to get them (Figure 10). These curves were built from the results of experiments that have not been systematically reported in the result tables. It appears that the older the seed dispersion, the higher the amount of multi-silica clusters. The results concerning the silica batch II are a little bit less relevant because the polymerization conditions were different from the viewpoint of the surfactant composition and proportion. These results are consistent with the investigations reported by Ibisate *et al.* for getting silica dimers by spontaneous aggregation [29]. They demonstrated that the age of the silica seeds influences the yield of dimers, *i.e.* the aggregation of two silica particles. Indeed, it is known that the stability of silanol groups on the surface of silica particles is strongly dependent on the pH value, solvent nature, and ionic impurities [30]. These silanol groups are stable in water at pH 3 to 5, however they condense rapidly at pH values in the range from 7 to 9. Therefore, keeping the silica seeds in an aqueous solution at a pH range between 7 and 9 (here, the pH value is 7.5) could lead to the condensation of adjacent silanol groups, which arises from the continuous decrease of the repulsive barrier, *i.e.* the surface zeta potential.

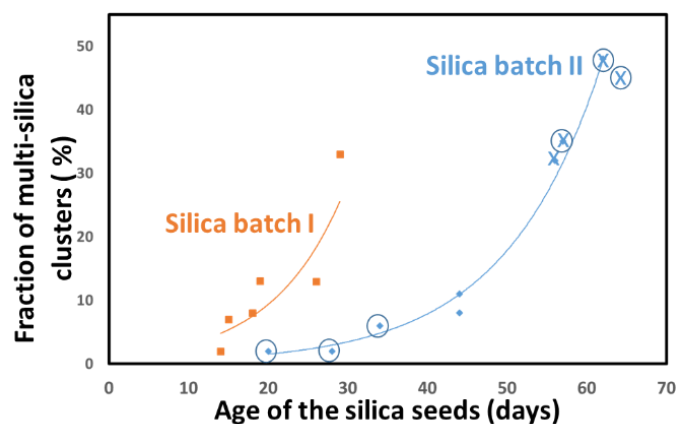


Figure 43: A plot of the age of silica seeds from batch II (orange dots) and batch I (blue dots) versus the percentage of multi-silica clusters; For the batch II, the surfactant concentration or the SDS fraction were such as: \odot 3 g/L of surfactants, and 5 % SDS; \circ 3 g/L of surfactants and 7 % SDS; \times 4 g/L of surfactants and 5 % SDS; \otimes 4 g/L of surfactants and 7 % SDS. These curves were built from the results of experiments that haven't been systematically reported in the result tables. The sonication time for the overall samples is 10 min except for the samples labelled with \times (30 min).

2.4.4 Influence of the styrene initial concentration

Another way to increase the value of $N_{PS/silica}^0$ would be to decrease the initial styrene concentration, which is quite similar to the previous strategy because it also consists in increasing the surfactant-to-monomer ratio. This affects $N_{PS/silica}^0$ and D_{PS} , as demonstrated by Désert *et al.* [10]. Therefore, the styrene concentration was decreased from 45 to 35, then 26 and finally 15 g/L (Table 4, entries #14 to #18). With 35 g/L, dodecapods were obtained with a yield of 70 % (Figure 44A). With regards to the Experiment #10, the PS nodules were smaller ($D_{PS} = 75$ nm vs. 80 nm). For lower styrene concentrations, any dodecapod was obtained; the PS nodules were systematically much smaller and much more numerous, as in raspberry-like structures (Figure 44B).

Table 4: Morphology and geometrical parameters of the PS/silica clusters as a function of the initial styrene concentration and surfactant mixture composition and concentration obtained after the following conditions: $[\text{Na}_2\text{S}_2\text{O}_8]_0 = 0.5 \text{ g/L}$; $[\text{silica}] = 7.3 \cdot 10^{15} \text{ part./L}$ and $d_{\text{MMS}} = 0.5 \text{ function per nm}^2$.

		Entry	# 14	# 15	# 16	# 17	# 18
Experimental conditions	Seed batch number		IV	IV	IV	IV	IV
	Age of the seeds (days)		7	10	11	13	15
	$[\text{styrene}]_0$ (g/L)		35	26	26	26	15
	$[\text{surfactant}]$ (g/L)		3	4	3	3	3
	Symperonic® NP30 / SDS mass ratio		93/7	95/5	93/7	95/5	95/5
	Monomer-to-polymer conversion (%)		82	77	75	80	78
	R_V^∞		13.2	-	-	-	-
	$R_V^{\infty \text{local}}$		8.2	-	-	-	-
Final batch composition in clusters	% Nonapods		7				
	% Decapods		8				
	% Hendecapods		7				
	% Dodecapods		70				
	% Raspberry-like clusters			100	100	100	100
	% Multi-silica clusters		8				
	D_{PS} (nm) on dodecapods		75				
	PDI of D_{PS} on dodecapods		1.02				
free PS	Estimated amount		++	++	++	++	++
	$D_{\text{free PS}}$ (nm)		80	-	-	-	-
	$N_{\text{PS/silica}}^0$		25	-	-	-	-

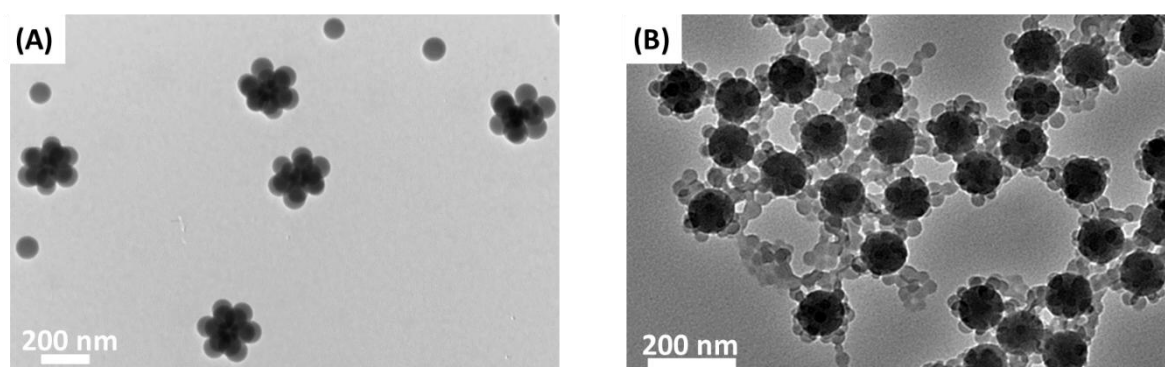


Figure 44: Typical TEM images of the PS/silica clusters obtained by styrene emulsion polymerization from 85-nm silica seeds under the experimental conditions described in Table 4. (A) Entry # 14. (B) Entry #15.

For these reasons, we decided to use the dodecapods obtained from the Experiments #10 and #11 as precursor batches for the rest of the study.

3. Stage III: Derivatization of the PS/silica dodecapods into DDS clusters

3.1 Template regrowth of the silica cores

The regrowth of the silica core was performed in ethanol/ammonia mixture, *i.e.* Stöber's medium, through the addition of a controlled quantity of TEOS. This regrowth step may be seen as an extra regrowth stage of the initial silica pre-seeds (*cf.* § 1). The experiments were conducted according to the Protocol 5.

Protocol 5: Regrowth of the silica cores of the silica/PS dodecapods.

In a 1L round bottom flask, 225 mL of ethanol (99 %) and 17.5 mL of ammonia (28-30 %, J.T. Baker) corresponding to $[NH_3] = 1 M$ are added. The mixture is stirred and 5 mL of the aqueous dispersion of the silica/PS clusters, corresponding to $3.7 \cdot 10^{13}$ particles, obtained through the Protocol 4 are added in order to have a total water concentration of 3.6 M. The flask is closed with a septum and 5 mL of the proper amount of ethanol solution of TEOS (10 vol.% diluted in ethanol absolute) is dropwise added at a rate of 1 mL/h. The average size of the regrown silica cores is determined from the statistical analysis of the TEM images.

TEM images show that the diameter of the silica core (178 nm) was consistent with the expected one (180 nm) (Figure 45). However, some silica tiny nanoparticles were sometimes observed on the TEM grid or attached to the PS satellites. This phenomenon stemmed from a secondary nucleation of silica during the regrowth of the silica core indicating that the mechanism of homogeneous nucleation or nucleation on the PS surface wasn't fully avoided. However, these silica tiny nanoparticles are supposed to be removed during the forthcoming stages of PS dissolution and particle washing.

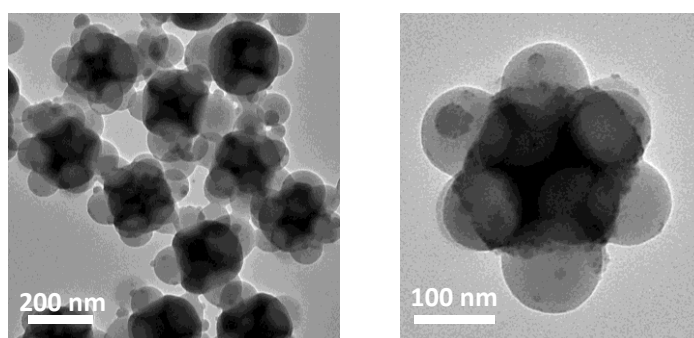


Figure 45: TEM images of dodecapods after the regrowth stage of the silica core.

3.2 Passivation of the silica core

Chomette *et al.* reported the requirement of passivating the silica core by propyltrimethoxysilane (PTMS) to promote the forthcoming stage of site-specific gold

nanoparticle adsorption (*cf.* chapter III) [12]. PTMS bears a non polar methyl group that is expected to not be sticky with regard to the gold nanoparticles, contrarily to the bottom of the dimples which will be specifically made sticky as described in the forthcoming sections.

Protocol 6: Passivation of the inter-pod surface area of the dodecapods with PTMS.

Typically, the dispersion of the regrown silica/PS clusters obtained after Protocol 5 in their reacting ethanol/ammonia mixture maintained in the growth flask and a volume of PTMS corresponding to 50 functions per nm² (section 2.2 from the appendix) is introduced in the flask in one shot. The reaction is let to be completed under stirring at ambient temperature for 12 h.

No specific characterization was performed at the end of this stage to check its success, which is indeed indirectly confirmed by that of the stage of the site-specific gold adsorption (*cf.* Chapter III).

3.3 Dissolution of the PS nodules

The PS chains are known to be soluble in solvents like dimethylformamide (DMF) and tetrahydrofuran (THF). Both solvents are used successively according to the Protocol 7.

Protocol 7: Dissolution of the PS nodules.

A volume of DMF corresponding to 10 vol. % of the volume of the dispersion obtained after the Protocol 6 is added. Subsequently, the mixture is heated at 70°C and is partially evaporated under vacuum by a rotavapor. The temperature is increased to 90°C and the evaporation continued until the dispersion turns from white to transparent indicating the solvent transfer of the silica particles from ethanol to DMF thanks to the refractive index matching of silica and DMF ($n_{DMF} = 1.4305$ and $n_{amorphous\ silica} = 1.4585$ at 20°C for $\lambda = 589\text{ nm}$). The solubilized PS chains are then removed by 3 cycles of centrifugation/redispersion in 20 mL of THF (12,000 g; 10 min).

This procedure allowed an efficient removal of the PS nodules resulting in the development of the expected concave areas at the positions previously occupied by the PS nodules (Figure 46). Furthermore, this protocol is efficient to remove the PS satellites, but it is also helpful to get rid of the silica nanoparticles appearing sometimes on the PS surface during the silica regrowth step. It makes sense when considering the difference of sedimentation rates in between the large DDS clusters and the silica nanoparticles. Even if the identification of DDS clusters is quite tricky, we checked that their fraction is close to 75 %, *i.e.* similar to that of the dodecapods in the precursor PS/silica cluster batch. The main by-products are the dimpled silica particles resulting from the multi-silica clusters (about 10 %) and specifically labelled with a red arrow on the Figure 46.

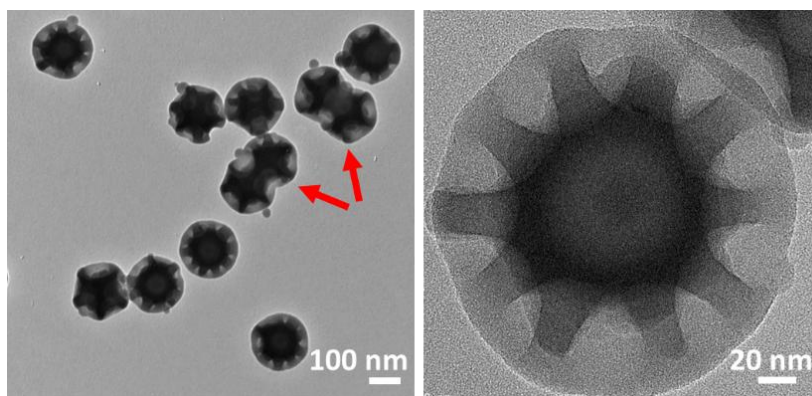
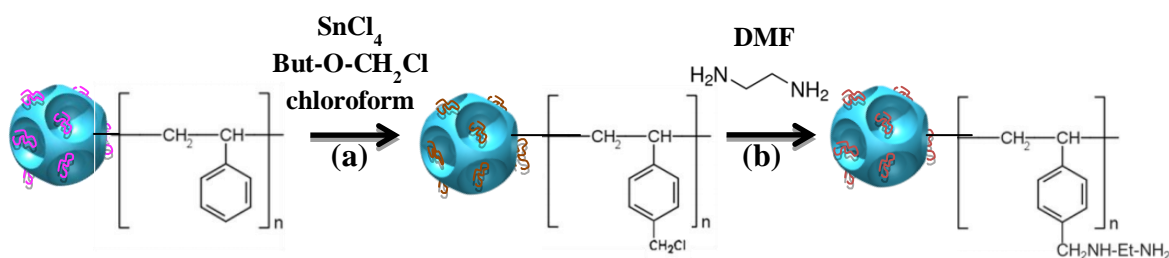


Figure 46: TEM images of the DDS clusters obtained after the regrowth of the silica cores and the dissolution of the PS satellites. The red arrows highlight some by-products, which result from the presence of multi-silica clusters in the precursor batch of PS/silica dodecapods.

4. Stage IV: Chemical modification of the PS residue at the bottom of the dimples

Previous studies reported the presence of a residual PS bump at the bottom of each dimple. These are undissolved PS chains which result from the copolymerization with the methacryloxymethyl grafts and these are therefore covalently bounded to the silica seed surface [11,31]. Chomette *et al.* estimated that their number average and weight average molar masses are $\overline{M}_n = 540\,000$ g/mol and $\overline{M}_w = 980\,000$ g/mol, respectively, and that each PS bump is made of 28 ± 12 PS chains.

Because these PS bumps aren't naturally sticky to gold nanoparticles, a chemical modification of these PS macromolecules is required. Chomette *et al.* optimized successfully a chemical pathway to specifically functionalize the styrene repeat units by electrophilic aromatic substitution of the phenyl ring (Scheme 3): chloromethylation and then amination which was preferred to thiolation which appeared trickier [32,31].



Scheme 3: Functionalization of the residual PS by (a) chloromethylation and then (b) amination.

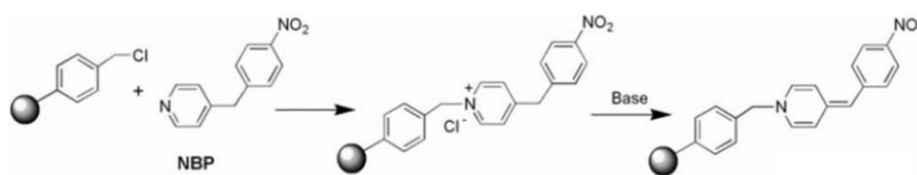
4.1 Chloromethylation of the PS residue

The chloromethylation reaction of the PS macromolecules was carried out in the presence of a Lewis acid SnCl_4 used as a catalyst and a butyl chloromethyl ether as a chloromethyl reagent. This reaction is based on a Friedel-Crafts reaction, as to say, an electrophilic substitution of the $=\text{C}-\text{H}$ bond of benzene ring by $-\text{CH}_2\text{Cl}$ groups. Moreover, several conditions must be fulfilled: (i) the reaction should occur in a good solvent of PS and (ii) the reagents and solvents involved in the reaction must be inert with regard to the silica core. Therefore, butyl chloromethyl ether, SnCl_4 and chloroform appeared to be a suitable reactive system (Protocol 8). The chloromethylating agent was preliminarily prepared according to a specific protocol using butyl alcohol, paraformaldehyde and gaseous HCl at low temperature (5°C) [33,34].

Protocol 8: Chloromethylation of the PS macromolecules on the DDS clusters.

The DDS clusters obtained after the PS dissolution step (Protocol 7) are centrifuged and redispersed 3 times in 20 mL chloroform. Subsequently, 20 mL of the DDS clusters (1.8×10^{15} part./L) redispersed in chloroform, are added in a flask with 5 mL of butyl chloromethyl ether 3 M in chloroform (large excess) and 0.3 mL of SnCl_4 . The temperature is set at 45°C and the mixture is stirred overnight. Finally, the solution is washed one time in ethanol, three times in HCl solution (4 wt.% in water) and three times in water/ethanol (50/50 wt.%). Finally, the DDS clusters are redispersed in 20 mL of DMF. For each washing step, the particles are centrifuged at 12,000 g during 10 min.

To check the success of the chloromethylation of the PS residue a colorimetric test, based on the reaction between nitrobenzyl pyridine (NBP) and chloromethyl groups was performed (Scheme 4) according to Protocol 9 [35].



Scheme 4: Reaction of the nitrobenzyl pyridine (NBP) molecule with a chloromethylated phenyl group

Protocol 9: Colorimetric test highlighting the presence of chloromethyl groups.

One mL of the DDS clusters dispersion in DMF (corresponding to 2×10^{12} particles) is introduced in a 10-mL flask. Two mL of 0.05 M NBP (Sigma Aldrich) and 15 μL of TEA (Aldrich) are added. The temperature is increased to 90°C and the mixture is stirred for 30 min. Finally the dispersion is transferred into a falcon tube and centrifuged at 12 000 g for 10 min and observed with the eye.

A color change is observed, after the reaction. Indeed, the chloromethylated particles exhibited a noticeable pink/purple color (Figure 47) which is consistent with the results obtained for Merrifield-resin with NBP reported by Galindo *et al.* [35].



Figure 47: Picture of the NBP assay on chloromethylated DDS clusters.

4.2 Amination of the chloromethylated PS residue

The substitution of the chloromethylated PS chains was performed by ethylene diamine in DMF. A large excess of ethylene diamine is required in order to prevent the cross linking of the PS through the reaction of both primary amino groups of ethylene diamine with chloromethyl groups. Indeed, the addition of a low amount of ethylene diamine with regard to the chloromethylated species can lead to the diamine to serve as a bridging molecule inducing a lower number of primary amines and the cross-linking of the macromolecules making them less capable to be extended in good solvents (Protocol 10).

Protocol 10: Amination of the chloromethylated PS macromolecules.

The chloromethylated dimples particles ($3.6 \cdot 10^{13}$ particles) obtained after the chloromethylation reaction (Protocol 8), are centrifuged and redispersed in 20 mL DMF. The dimples particles are introduced in a flask equipped with a condenser and a magnetic stirrer. Three mL of ethylene diamine (large excess) are introduced, and the temperature is set at 90°C and stirred overnight. The particles are then, washed by centrifugation and redispersed in ethanol, and then washed 2 times in water. Finally the solution is acidified using few drops of HCl then the particles are centrifuged and redispersed in 20 mL Milli-Q® water.

No specific characterization was performed at the end of this stage to check its success which is indeed indirectly confirmed by that of the stage of the site-specific gold adsorption (*cf.* Chapter III).

5. Conclusion

In this chapter, we have first described how we revisited again the successive stages of: (i) synthesis of highly size-monodisperse batches of silica seeds, (ii) seeded-growth emulsion polymerization of styrene for getting dodecapod-like silica/PS clusters, (iii) emulsion polymerization, (iv) regrowth of the silica cores and subsequent development of the dimples by dissolution of the PS satellites and (v) specific functionalization of the residual PS macromolecules for grafting amino groups along the anchored PS macromolecules. These chemical groups are expected to allow the site-specific adsorption of gold nanoparticles and seed-mediated growth to get large gold satellites (*cf.* Chapter III).

We also contributed to highlight the robustness of the PS/silica dodecapod synthesis with an initial average morphology yield of 50 %, and a quite size polydisperse PS satellites on the dodecapods. Therefore, we studied the influence of the SDS-to-NP30 mass ratio, the total concentration of the surfactant, and the styrene concentration. By increasing the initial number of PS nuclei, we were able to increase the morphology yield of dodecapods to 75%.

Several types of by-products remain in our dodecapod batches such as: (i) multi-silica clusters, which may arise from the destabilization of the silica seeds with their age and (ii) clusters with less than twelve PS satellites, which stemmed from an uncomplete geometrical refinement. A purification step by gradient density centrifugation could be envisaged, but it would be very tricky because of the low contrast of apparent density between the targeted dodecapods and the by-products.

Lastly, the DDS clusters obtained from this study and used for the forthcoming experiments described in the next chapters display the following geometrical features:

Table 5: Summary of the dimensions of the functional DDS clusters used for the forthcoming experiments

	Batch #10	Batch #11
Total diameter (nm)	175	175
Depth of the dimple (nm)	43	38
External diameter of the dimples (nm)	81	78
Purity in DDS clusters (%)	75	73

6. References

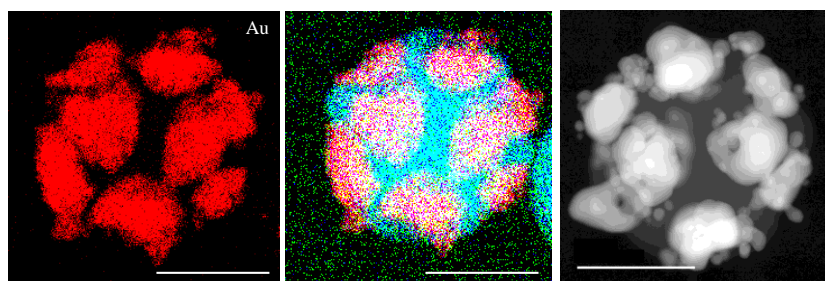
- [1] S. Reculosa, “Thèse de l’Université Bordeaux I: Synthèse de matériaux d’architecture contrôlée à base de silice colloïdale,” 2004.
- [2] A. Perro, “Thèse de l’Université Bordeaux I: Synthèse et valorisation de particules colloïdales de morphologie et de fonctionnalité de surface contrôlées,” 2006.
- [3] D. Nguyen, “Thèse de l’Université Bordeaux I: Etude de la nucléation contrôlée de latex polymère à la surface de nanoparticules d’oxyde pour l’élaboration de colloïdes hybrides structurés,” 2008.
- [4] A. Désert, “Thèse de l’Université Bordeaux 1: Colloïdes hybrides silice/polystyrène de morphologie contrôlée,” 2011.
- [5] S. Reculosa, C. Mingotaud, E. Bourgeat-Lami, E. Duguet, and S. Ravaine, “Synthesis of daisy-shaped and multipod-like silica/polystyrene nanocomposites,” *Nano Lett.*, vol. 4, no. 9, pp. 1677–1682, 2004.
- [6] A. Perro, S. Reculosa, E. Bourgeat-Lami, E. Duguet, and S. Ravaine, “Synthesis of hybrid colloidal particles: From snowman-like to raspberry-like morphologies,” *Colloids Surfaces A Physicochem. Eng. Asp.*, vol. 284–285, pp. 78–83, 2006.
- [7] A. Perro, E. Duguet, O. Lambert, J.-C. Taveau, E. Bourgeat-Lami, and S. Ravaine, “A chemical synthetic route towards colloidal molecules,” *Angew. Chemie Int. Ed.*, vol. 48, no. 2, pp. 361–365, 2009.
- [8] J.-C. Taveau, D. Nguyen, A. Perro, S. Ravaine, E. Duguet, and O. Lambert, “New insights into the nucleation and growth of polystyrene nodules on silica nanoparticles by 3D cryo-electron tomography,” *Soft Matter*, vol. 4, no. 2, pp. 311–315, 2008.
- [9] A. Désert, I. Chaduc, S. Fouilloux, J.-C. Taveau, O. Lambert, M. Lansalot, E. Bourgeat-Lami, A. Thill, O. Spalla, S. Ravaine, and E. Duguet, “High-yield preparation of polystyrene/silica clusters of controlled morphology,” *Polym. Chem.*, vol. 3, no. 5, pp. 1130–1132, 2012.
- [10] A. Désert, J. Morele, J.-C. Taveau, O. Lambert, M. Lansalot, E. Bourgeat-Lami, A. Thill, O. Spalla, L. Belloni, S. Ravaine, and E. Duguet, “Multipod-like silica/polystyrene clusters,” *Nanoscale*, vol. 8, no. 10, pp. 5454–5469, 2016.
- [11] A. Désert, C. Hubert, Z. Fu, L. Moulet, J. Majimel, P. Barboteau, A. Thill, M. Lansalot, E. Bourgeat-Lami, E. Duguet, and S. Ravaine, “Synthesis and site-specific functionalization of tetravalent, hexavalent, and dodecavalent silica particles,” *Angew. Chemie Int. Ed.*, vol. 52, no. 42, pp. 11068–11072, 2013.
- [12] C. Chomette, “Thèse de l’université de Bordeaux: Design and synthesis of plasmonic meta-atoms from patchy particles,” 2015.
- [13] C. Chomette, M. Tréguer-Delapierre, N. B. Schade, V. N. Manoharan, O. Lambert, J.-C. Taveau, S. Ravaine, and E. Duguet, “Colloidal alchemy: Conversion of polystyrene nanoclusters into gold,” *ChemNanoMat*, vol. 3, no. 3, pp. 160–163, 2017.
- [14] K. D. Hartlen, A. P. T. Athanasopoulos, and V. Kitaev, “Facile preparation of highly monodisperse small silica spheres (15 to >200 nm) suitable for colloidal templating and formation of ordered arrays,” *Langmuir*, vol. 24, no. 5, pp. 1714–1720, 2008.
- [15] W. Stöber, A. Fink, and E. Bohn, “Controlled growth of monodisperse silica spheres in the micron size range,” *J. Colloid Interface Sci.*, vol. 26, no. 1, pp. 62–69, 1968.
- [16] A. Perro, D. Nguyen, S. Ravaine, E. Bourgeat-Lami, O. Lambert, J.-C. Taveau, and E. Duguet, “Planar submicronic silica–polystyrene particles obtained by substrate-directed shaping,” *J.*

- Mater. Chem.*, vol. 19, no. 24, pp. 4225–4230, 2009.
- [17] E. Bourgeat-Lami, M. Insulaire, S. Reculosa, A. Perro, S. Ravaine, and E. Duguet, “Nucleation of polystyrene latex particles in the presence of γ -methacryloxypropyl-trimethoxysilane: functionalized silica particles,” *J. Nanosci. Nanotechnol.*, vol. 6, pp. 432–444, 2006.
- [18] A. Thill, A. Désert, S. Fouilloux, J.-C. Taveau, O. Lambert, M. Lansalot, E. Bourgeat-Lami, O. Spalla, L. Belloni, S. Ravaine, and E. Duguet, “Spheres growing on a sphere: A model to predict the morphology yields of colloidal molecules obtained through a heterogeneous nucleation route,” *Langmuir*, vol. 28, no. 31, pp. 11575–11583, 2012.
- [19] B. V. Derjaguin and Landau L., “Theory of the stability of strongly charged lyophobic sols and of the adhesion of strongly charged particles in solution of electrolytes,” *ActaPhysico Chem. URSS*, no. 14, p. 633, 1941.
- [20] E. J. W. Verwey, “Theory of the stability of lyophobic colloids,” *J. Phys. Colloid Chem.*, vol. 51, no. 3, pp. 631–636, 1947.
- [21] D. Radziuk, D. Grigoriev, W. Zhang, D. Su, H. Möhwald, and D. Shchukin, “Ultrasound-assisted fusion of preformed gold nanoparticles,” *J. Phys. Chem. C*, vol. 114, no. 4, pp. 1835–1843, 2010.
- [22] Z. Zhong, F. Chen, A. S. Subramanian, J. Lin, J. Highfield, and A. Gedanken, “Assembly of Au colloids into linear and spherical aggregates and effect of ultrasound irradiation on structure,” *J. Mater. Chem.*, vol. 16, no. 5, pp. 489–495, 2006.
- [23] C. H. Bernard Ng and W. Y. Fan, “Colloidal beading: Sonication-induced stringing of selenium particles,” *Langmuir*, vol. 30, no. 25, pp. 7313–7318, 2014.
- [24] K. S. Suslick, “The chemical effects of ultrasound,” *Sci. Am.*, vol. 260, p. 80–86, 1989.
- [25] K. S. Suslick and G. J. Price, “Applications of ultrasound to materials chemistry,” *Annu. Rev. Mater. Sci.*, vol. 29, no. 1, pp. 295–326, 1999.
- [26] S. J. Doktycz and K. S. Suslick, “Interparticle collisions driven by ultrasound,” *Science*, vol. 247, no. 4946, pp. 1067–1069, 1990.
- [27] T. Prozorov, R. Prozorov, and K. S. Suslick, “High velocity interparticle collisions driven by ultrasound,” *J. Am. Chem. Soc.*, vol. 126, no. 43, pp. 13890–13891, 2004.
- [28] N. Mandzy, E. Grulke, and T. Druffel, “Breakage of TiO₂ agglomerates in electrostatically stabilized aqueous dispersions,” *Powder Technol.*, vol. 160, no. 2, pp. 121–126, 2005.
- [29] M. Ibisate, Z. Zou, and Y. Xia, “Arresting, fixing, and separating dimers composed of uniform silica colloidal spheres,” *Adv. Funct. Mater.*, vol. 16, no. 12, pp. 1627–1632, 2006.
- [30] H.-P. Boehm, “The chemistry of silica. Solubility, polymerization, colloid and surface properties, and biochemistry,” *Angew. Chemie*, vol. 92, no. 4, p. 328, 1980.
- [31] C. Chomette, E. Duguet, S. Mornet, E. Yammine, V. N. Manoharan, N. B. Schade, C. Hubert, S. Ravaine, A. Perro, and M. Treguer-Delapierre, “Templated growth of gold satellites on dimpled silica cores,” *Faraday Discuss.*, vol. 191, pp. 105–116, 2016.
- [32] G. D. Jones, “Chloromethylation of polystyrene,” *Ind. Eng. Chem.*, vol. 44, no. 11, pp. 2686–2693, 1952.
- [33] A. Warshawsky and A. Deshe, “Halomethyl octyl ethers: Convenient halomethylation reagents,” *J. Polym. Sci. Polym. Chem. Ed.*, vol. 23, no. 6, pp. 1839–1841, 2003.
- [34] C. Lü, B. Gao, Q. Liu, and C. Qi, “Preparation of two kinds of chloromethylated polystyrene particle using 1,4-bis(chloromethoxy)butane as chloromethylation reagent,” *Colloid Polym.*

Sci., vol. 286, no. 5, pp. 553–561, 2008.

- [35] F. Galindo, B. Altava, M. I. Burguete, R. Gavara, and S. V Luis, “A Sensitive Colorimetric Method for the Study of Polystyrene Merrifield Resins and Chloromethylated Macroporous Monolithic Polymers,” *J. Comb. Chem.*, vol. 6, no. 6, pp. 859–861, 2004.

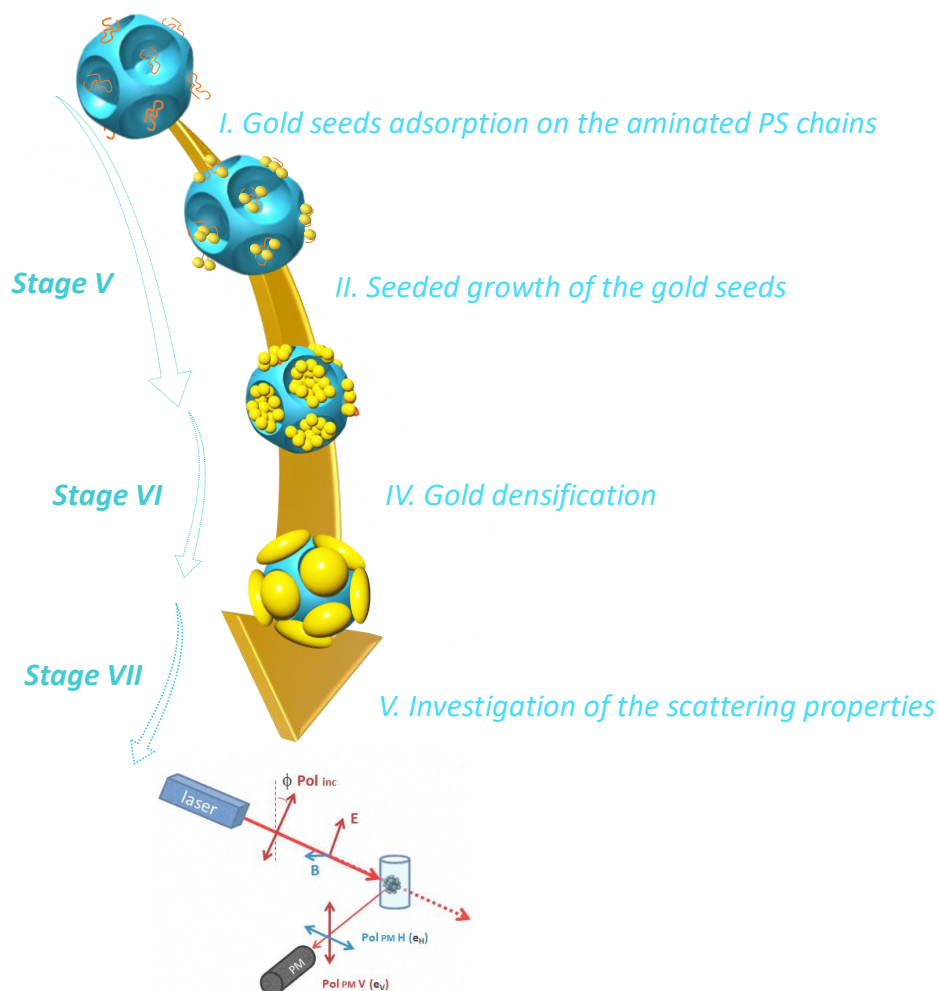
Chapter III :
Synthesis of gold
dodecahedral clusters and
optical investigations



EDX and STEM pictures of Au dodecahedral clusters, scale bars: 100 nm

The objectives in this chapter were to grow gold satellites within the twelve dimples of the silica clusters to get the gold dodecahedral clusters (GDC) and to measure their magnetic and electric responses in the visible / near-IR spectral ranges. The synthetic pathway includes the site-specific adsorption of seeds, their growth, and their densification as shown on the Scheme 5 [1].

In the following sections, we describe the experimental procedure that we developed for the successful synthesis of the plasmonic nanoclusters in high yield. The procedure is inspired by a protocol previously developed by Chomette *et al.* [2]. We optimized the synthesis process of the GDC. The multipolar optical response of the engineered GDC was analyzed across the whole visible range by using polarization resolved static light scattering at variable angle and was compared to the one of the gold raspberry-like NPs'.



Scheme 5: Five-stage synthetic strategy to fabricate the GDC

1. Stage V: Seeded growth of gold seeds on aminated PS chains

1.1 Synthesis of the gold seeds

Tiny gold seeds were synthesized by the Duff's method [3]. In brief, tetrakis(hydroxymethyl)phosphonium chloride (THPC) was added in a reacting medium with an excess of NaOH to produce: (i) a capping agent: THPO (Figure 48,III), (ii) a reducing agent: formaldehyde and H₂. HAuCl₄ was then added to the medium leading to the reduction of Au³⁺ into Au⁰ and the subsequent formation of tiny gold seeds (Protocol 1).

Protocol 11: Synthesis of 1-3 nm tiny gold seeds

In a 500-mL round bottom flask, 227.5 mL of milliQ water, 7.5 mL of an aqueous solution of NaOH (0.2 M) and 5 mL of THPC aqueous solution (120 μL in 10 mL) were introduced. The solution is homogenized for 15 min. Subsequently, 10 mL of HAuCl₄ (25 mM) was quickly injected into the mixture under stirring. The solution was left to stir for 30 min. Finally, the solution was stored protected from light at 4°C

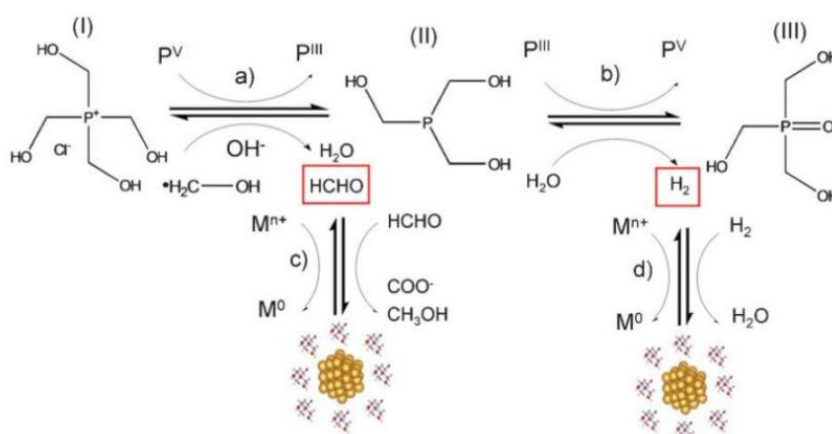


Figure 48: Mechanism describing the role of THPC in the formation of gold seeds: (I) THPC is converted into (III) THPO, producing formaldehyde and H₂, both serving as reducing agents [3].

A typical color change from yellow to brownish was observed during the formation of the seeds. The colloidal suspension of the gold seeds was characterized by UV-Vis absorption spectroscopy (Figure 49). The absorption spectrum exhibits a shoulder around 500 nm, which is characteristic of gold seeds of small size [3].

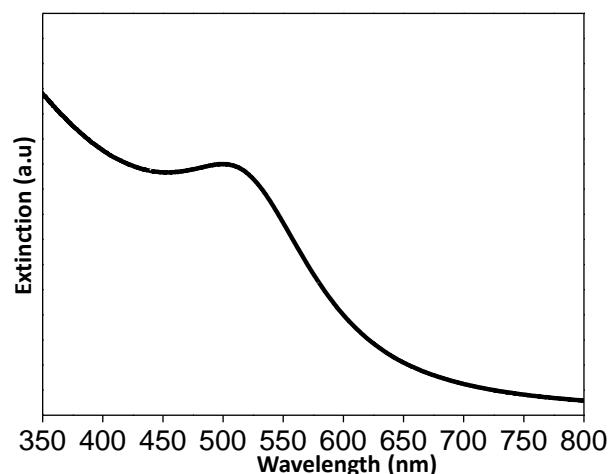


Figure 49: UV-visible extinction spectrum of the tiny gold seeds suspension in water

1.2 Adsorption of gold seeds on the aminated PS chains

Subsequently, the tiny gold seeds were introduced in a suspension of DDS clusters with aminated PS chains in order to promote their adsorption onto the bottom of the dimples (Protocol 12).

Protocol 12: Adsorption of gold duff seeds onto the aminated PS residues

2 mL of the aminated DDS clusters (corresponding to $3.7 \cdot 10^{12}$ NPs) obtained after Protocol 11 are mixed with 8 mL of the gold seeds dispersion and stirred overnight on a roller mixer. Finally, the dispersion is washed 3 times by centrifugation at 6,000 g during 10 min to remove all the excess of gold seeds and redispersed in 10 mL of milliQ water.

Figure 50 shows TEM images of the DDS clusters before and after gold seeds adsorption. It emphasizes the successful regioselective chemical functionalization of the dimples and the specific passivation of the DDS particles.

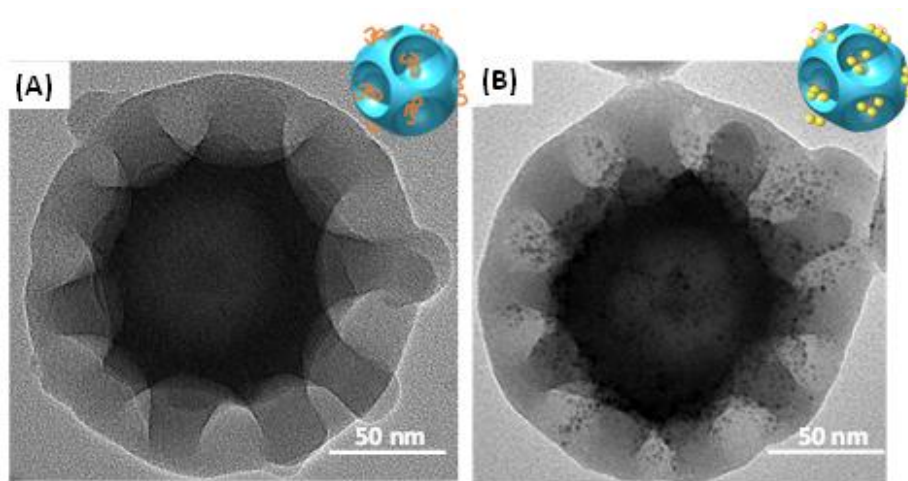
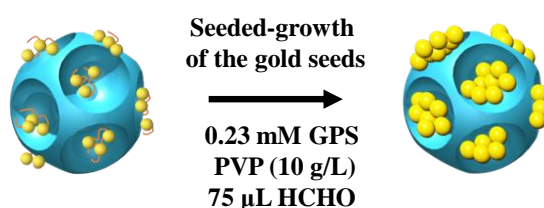


Figure 50: TEM images of the DDS clusters: (A) before and (B) after gold seeds adsorption.

1.3 Growth of the gold satellites from the attached seeds

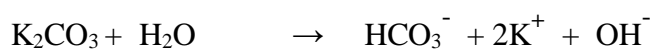
1.3.1 Principle of the seeded-growth method

The growth of the gold seeds was performed using a gold precursor solution made of $\text{Au}(\text{OH})_4^-$ and formaldehyde as reducing agent (Protocol 14; Scheme 6).



Scheme 6: General strategy to synthesize GDC by seeded-growth method

The gold precursor was prepared following the Oldenburg's method by mixing an aqueous solution of HAuCl_4 and K_2CO_3 (Protocol 13) [4]. The hydrolysis of HAuCl_4 occurs with time and form gold ion complexes ($[\text{AuCl}_x(\text{OH})_{4-x}]^-$, $x = 0-4$). Typically:



This solution is commonly called a gold plating solution (GPS). Contrary to AuCl_4^- , these gold ion complexes favor the formation of a continuous coating onto the silica particles [5-10]. It was reported that this coating route is pH-dependent as shown in Figure 51.

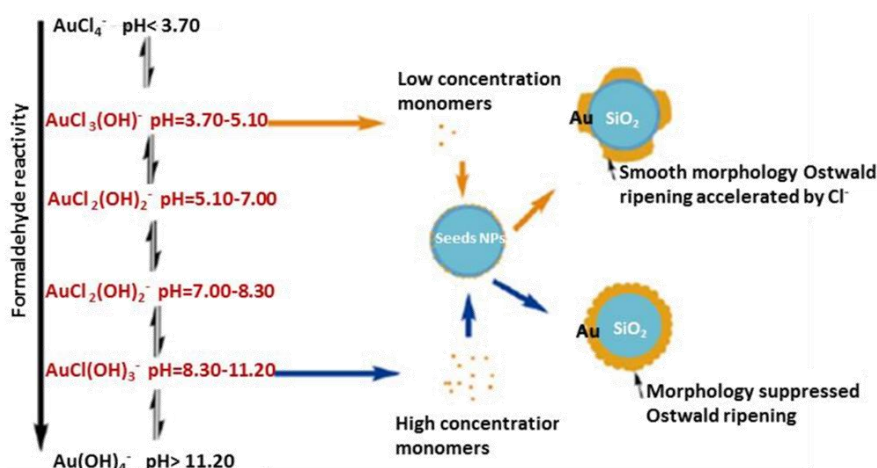


Figure 51: Influence of the: (i) pH solution used during the growth step on the gold shell morphology and (ii) formaldehyde reactivity with the gold precursor nature [5].

Protocol 13: Preparation of the GPS

100 mL of an aqueous solution containing 0.4 g/L of HAuCl_4 (99.9 %) and 1.25 g/L of K_2CO_3 was prepared and stirred for 3 h. A color change from yellow to colorless was observed. The solution was stored in the dark at 4°C.

Protocol 14: Seeded-growth of the tiny seeds anchored to the aminated dimples

For each regrowth, 1 mL of the dispersion of aminated DDS clusters (corresponding to $5 \cdot 10^{10}$ NPs) decorated by the gold seeds produced following Protocol 12 is introduced in a falcon tube. Subsequently, 10 mL of PVP solution (10 g/L; 29,000 g/mol) are added followed by the introduction of 0.23 mM of GPS (2 mM) produced according to Protocol 13. A volume of milliQ water is added to the suspension in order to have a final volume of 13 mL (including all the reactants). After homogenization an amount of formaldehyde solution (37 % in water) corresponding to 50 μL per mL of GPS is introduced. The reaction is left stirring overnight on a roller mixer. The NPs are washed by three cycles of centrifugation at 3,000 g for 10 min. If and additional regrowth is required, the GDC are redispersed in 1 mL of milliQ water, and Protocol 15 is repeated again. After the regrowth completion, the colloidal suspension of GDC is washed by three cycles of centrifugation at 3,000 g for 10 min, and redispersed in 13 mL PVP in milliQ water (10 g/L).

After the growth of the tiny gold seeds, TEM characterization allowed us to observe a partial dissolution of the clusters (Figure 52). In order to limit the silica dissolution, several investigations of: (i) the effect of the pH of the reaction media; (ii) the impact of the age of the GPS solution on the silica particles stability were carried out. It may be noted that an extra way was also investigated but unsuccessfully: it consisted in reinforcing the chemical stability of the silica core just after its regrowth (Chapter II, stage III) by a thermal treatment at 90°C in glycerol.

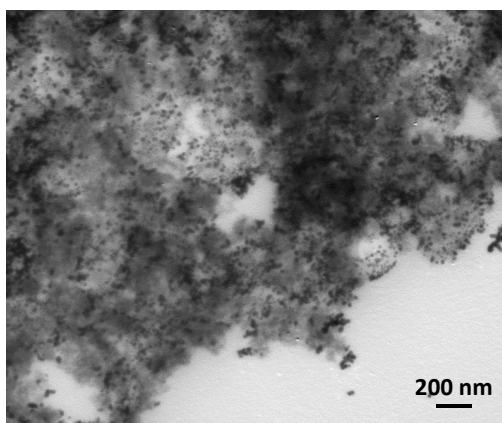


Figure 52: TEM image of the DDS clusters after the growth of the gold seeds

1.3.1.1. Influence of the pH of the reaction medium

The silica dissolution could be explained by a change of the pH of the reaction medium and/or a change of the ionic strength during the growth stage (Figure 53A) [11]. Several reports have shown that the stability of silica particles is pH-dependent. For example, Brady and Walther demonstrated that the dissolution of silica was favored in basic medium due to a drastic increase of the negatively-charged surface species $\equiv\text{Si}-\text{O}^-$ [12]. The authors claimed that the deprotonation of the surface hydroxyl groups would lead to highly polarized interatomic Si–O bonds promoting the detachment of Si into the solution. In acid medium, the dissolution of silica is well known to increase with the activity of protons at $0 < \text{pH} < 3$ [13-15]. The adsorption of the protons onto the silica would lead to the polarization of Si–O bonds and the subsequent detachment of the Si atom from the metal oxide. El Mourabi *et al.* carried out stability studies of silica in different acidic media (HCl, H₂SO₄, H₃PO₄) of similar ionic strengths [16]. They showed that the addition of an acid in the colloidal suspension of silica led to the interaction of the protons with the bridging oxygen of the metal oxide surface. This interaction would break the Si–O bond yielding to the formation of silanol Si–OH groups and, subsequently, a “gel” made of (SiOH₂)_n. The authors reported that the counter ion of the acidic species has a nucleophilic character and compensates the positive charge created on the silicon to obtain a system of Si–OH/Si–Nu (Figure 53C). This mechanism is consistent with previous studies which reported that sodium fluoride can play the role of catalyst in the sol-gel process [17].

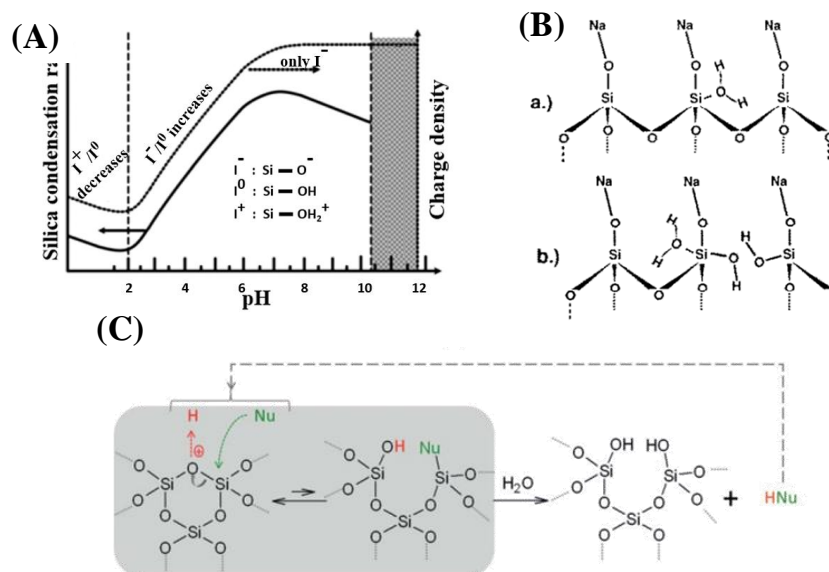


Figure 53: (A) Effects of pH value on the silica condensation rate, charge properties and charge density on the surface of the silica species [18]; (B) Schematic illustration of the dissolution process [19]: in (I) deionized water and (II) an electrolyte-bearing solution with Na⁺ ion as an example; (C) hydrolysis and condensation reversible mechanism involving nucleophilic species [16].

In our experimental conditions, the growth stage of the tiny seeds anchored on the aminated PS chains occurs at pH 8 which is in the domain of stability of the silica. Therefore, the phenomenon of dissolution observed upon the growth stage is surprising.

1.3.1.2 Influence of the gold precursor age to the growth step

A set of experiments was implemented to investigate the influence of the GPS age on the dissolution process of the silica. The experiments were performed with a "fresh" solution of GPS (2 days) and aged ones (2, 3 and 4 weeks). Figure 54 shows the typical TEM images of the clusters after the growth of the gold seeds.

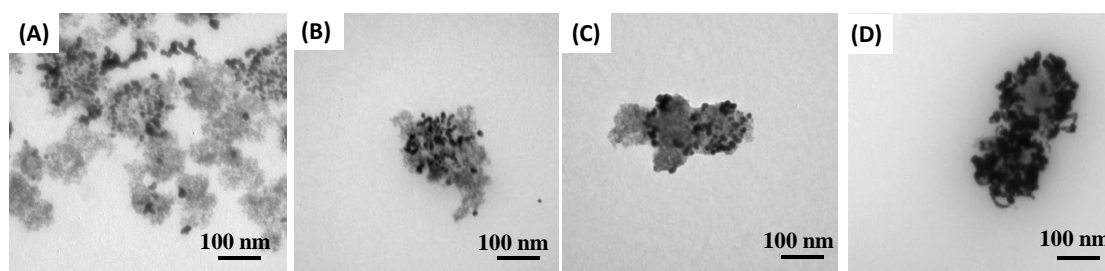


Figure 54: TEM images of the GDC obtained after the growth of the gold seeds using: (A) a fresh GPS solution; and aged ones: (B) 2 weeks; (C) 3 weeks and (D) 4 weeks.

By comparing thoroughly the results obtained from the different runs, we found that the use of a fresh GPS solution led to irreproducible results and to the dissolution of silica. This latter was considerably reduced using an aged solution of GPS. The older the solution, the greater the silica stability. This could be assigned to the complicated complex (AuCl_x(OH)_{4-x}) chemistry or a variation of pH of the GPS solution with time [20]. This

second hypothesis was discarded since no modification of the pH of the GPS solution was recorded over a period of one month (pH = 9.5). We can suppose that, in the fresh solution, the amount and/or activity of the metal counter ions (Cl^- and K^+) may be high, whereas, in contrast, in an aged solution, it is reduced. In the experimental conditions of the Protocol 3, complexes $[\text{AuCl}_x(\text{OH})_{4-x}]$ with $x = 0 - 4$ as well as free Cl^- and K^+ ions are formed in the solution. The counter-ions may adsorb on the silica surface and favor the silica dissolution. The dissolution of natural silica systems, in alkali and alkaline earth metal chloride solutions, was investigated by several groups [21-23]. The quartz silica dissolution can be promoted in contact with an increase of alkali and/or polyelectrolyte concentration. Theoretical investigations showed that some cations could directly interact with the silica surface leading to the formation of a coordinated complex. This latter would disturb the surface structures leading to the Si-O-Si linkage, as illustrated in Figure 6B. Thus, the presence of adsorbed cations on the silica quartz surface produces a steric effect allowing water to have a direct access to the Si-O-Si bonds. Experimentally, Dugger *et al.* evidenced the adsorption strengths of cations onto a silica gel surface at 35°C [24]. They reported that the adsorption strength follows the following trend $\text{NaCl} \approx \text{KCl} > \text{LiCl} > \text{MgCl}_2 > \text{H}_2\text{O}$. Thus, a faster dissolution rate was observed for sodium and potassium electrolyte solutions in comparison to magnesium chloride. The dissolution process is of course temperature dependent [19].

In summary, we believe that the dissolution process of the DDS clusters observed upon the growth of the gold seeds may be assigned to the adsorption of the counter-ions present in the GPS solution on the DDS surface. It would be interesting to carry out extensive studies by NMR or mass spectroscopy to get better understanding of the dissolution process as function of the age of the metal precursor solution. Knowledge of the role of the counter-ions is essential to the reproducibility and the scale-up of the controlled synthesis of the metal/silica clusters.

In the following study, a 4 weeks old GPS solution was systematically used to grow the gold seeds.

1.3.2 Investigation of the DDS clusters concentration

Figure 55A-B show that gold particles are located within the dimples of the DDS, after the addition of 0.23 mM of GPS to regrow the gold seeds. However, lot of free gold NPs could also be observed under these conditions. By increasing the number of silica particles in the reaction medium, typically from 5.10^{10} GDC to $3.6.10^{11}$ GDC, we obtained no by-

products (Figure 55C). Regardless of the amount of GPS, TEM images showed well-defined DDS clusters with regularly distributed dark and bright regions, corresponding to the gold satellites and bare convex portions of the silica core, respectively.

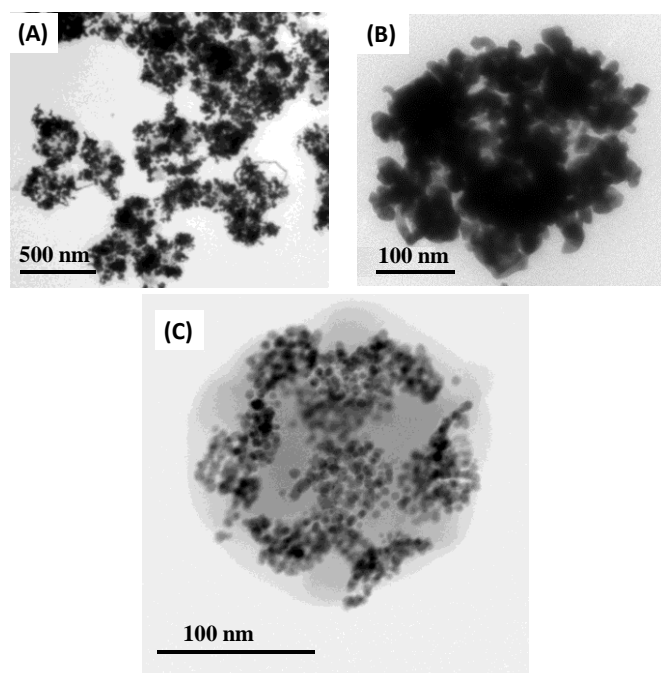
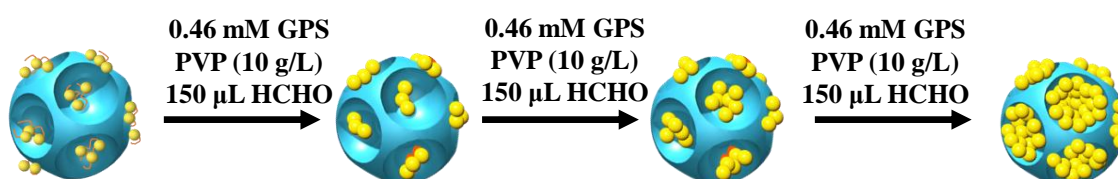


Figure 55: Typical TEM images of GDC obtained by performing the gold growth with 0.23 mM of GPS and an aliquot of: (A) and (B) 5.10^{10} GDC and (C) $3.6.10^{11}$ GDC

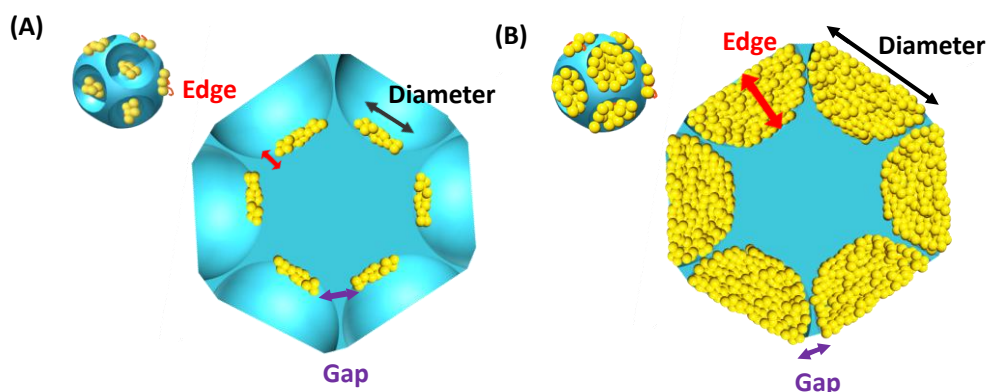
1.3.3 Investigation of the gold precursor concentration on the synthesis of GDC

The seed mediated growth was carried out using a maximum concentration of 0.46 mM of GPS per regrowth cycle, in order to avoid any homogeneous nucleation of gold. Thus the gold satellites were gradually increased following Protocol 15, and the experimental conditions summarized in Table 6.



Scheme 7: General sketch of the multistep seeded-growth method

Upon increasing the amount of gold precursor, step by step, the gold satellites are expected to increase in size (Scheme 8).



Scheme 8: Cross-section view of GDC upon increasing the amount of gold precursor during the growth of the gold seeds

Protocol 15: Seeded-growth of the tiny seeds anchored to the aminated PS chains following the optimized conditions

For each regrowth, 1 mL of the dispersion of aminated DDS clusters (corresponding to $3.6 \cdot 10^{11}$ NPs) decorated by the gold seeds produced following Protocol 12 is introduced in a falcon tube. Subsequently, 9 mL of PVP solution (10 g/L; 29,000 g/mol) are added followed by the introduction of a volume of GPS (2 mM) produced according to the Protocol 13. A volume of milliQ water is added to the suspension in order to have a final volume of 13 mL (including all the reactants). After homogenization an amount of formaldehyde solution (37 % in water) corresponding to 50 μ L per mL of GPS is introduced. The reaction is left stirring overnight on a roller mixer. The colloidal suspension is washed by three cycles of centrifugation at 3,000 g for 10 min. If an additional regrowth is required, the GDC are redispersed in 1 mL of milliQ water, and Protocol 15 is repeated again. After the regrowth completion, the GDC are washed by three cycles of centrifugation at 3,000 g for 10 min, and redispersed in 13 mL PVP in milliQ water (10 g/L), in order to have a suspension of GDC with a typical concentration of $3 \cdot 10^{13}$ part/L.

Table 6: Experimental conditions for the growth of the gold satellites

Batch	Number of gold seeds adsorbed DDS	1st regrowth			2nd regrowth			3rd regrowth		
		[GPS] _f (mM)	V _{PVP} (10 mL)	V _{HCHO} (μ L)	[GPS] _f (mM)	V _{PVP} (10 mL)	V _{HCHO} (μ L)	[GPS] _f (mM)	V _{PVP} (10 mL)	V _{HCHO} (μ L)
GDC-1	$3.6 \cdot 10^{11}$	0.23	9	75						
GDC-2		0.46	9	150						
GDC-3		0.46	9	200	0.15	9	50			
GDC-4		0.46	9	150	0.46	9	150			
GDC-5		0.46	9	150	0.46	9	150	0.3	9	100
GDC-6		0.46	9	150	0.46	9	150	0.46	9	150

The TEM images of the GDC obtained upon increasing the amount of gold precursor are shown in Figure 56. The gold satellites increase in size and maintain a shape that conforms the dimple's surface. The diameter of the gold satellites as a function of the amount of the

metallic precursor was evaluated by performing images analysis over 100 satellites per batch (Table 7). It should be noted, that the measured values of the diameters correspond to the 2D projection of the satellites, which depends on the orientation of the GDC on TEM grid. For the greatest volume of the plating solution used, the gold satellites reached an average diameter of 81 nm and an inter-satellite gap of 12 nm.

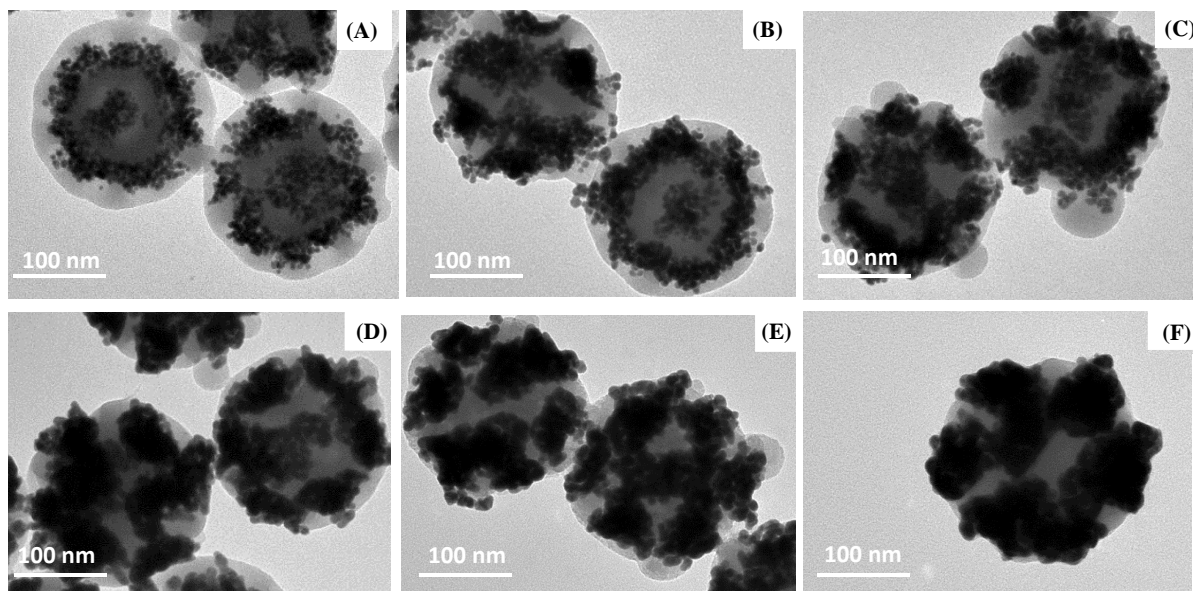


Figure 56: TEM images of the GDC upon increasing the GPS amount: (A) GDC-1; (B) GDC-2; (C) GDC-3 ; (D) GDC-4; (E) GDC-5; (F) GDC-6

The optical properties of these GDC were investigated with a conventional UV-Vis absorption spectrophotometer. Figure 57A shows the extinction spectra of the aqueous solutions of the DDS clusters before and after the growth step. Before the growth step, the extinction spectrum is consistent with plasmonic resonances of tiny gold seeds of few nm. After the growth, a red shift of the plasmon band is observed due to the increase in size of the seeds (Table 7). The larger the gold satellites, the more red-shifted the plasmon band (Figure 57). The observed progressive broadening of the plasmon band can be attributed to the size polydispersity of the gold satellites and the coupling of (i) the gold particles within a dimple or (ii) the gold satellites.

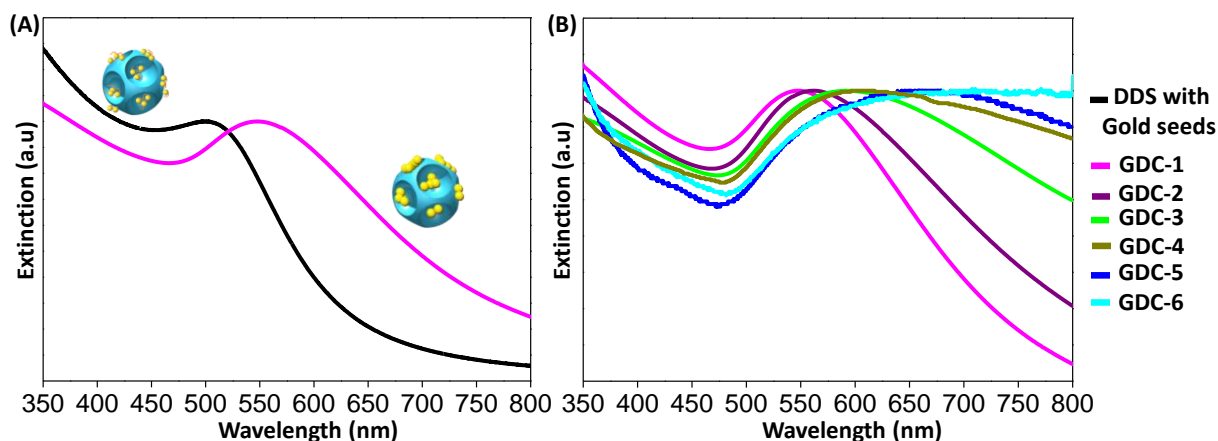


Figure 57: Variation of the UV-Visible extinction spectra of the: (A) of the GDC before and after the gold growth (GDC-4); (B) GDC when increasing the amount of GPS, after successive regrowth cycles.

Table 7: Evolution of the satellites size, and maximum of the plasmon band λ_{\max} of GDC suspension, upon increasing the amount of GPS added to the reaction medium

Batch name	GDC-1	GDC-2	GDC-3	GDC-4	GDC-5	GDC-6
[GPS] _{Total} (mM)	0.22	0.46	0.60	0.92	1.22	1.40
Diameter of the satellites (nm)	50	58	64	70	75	81
In-between satellites gap	20	18	16	12	10	7
λ_{\max} (nm)	547	560	590	620	660	720-800

1.3.4 Characteristics of the GDC after the seeded-growth of gold particles

Two batches (GDC-1 and GDC-4) were characterized more accurately by STEM (Scanning transmission electron microscopy) and EDX (Energy-dispersive X-ray Spectroscopy) (Figure 58). In both cases, the images highlight the well-defined patterns of gold, symmetrically arranged within the 12 dimples.

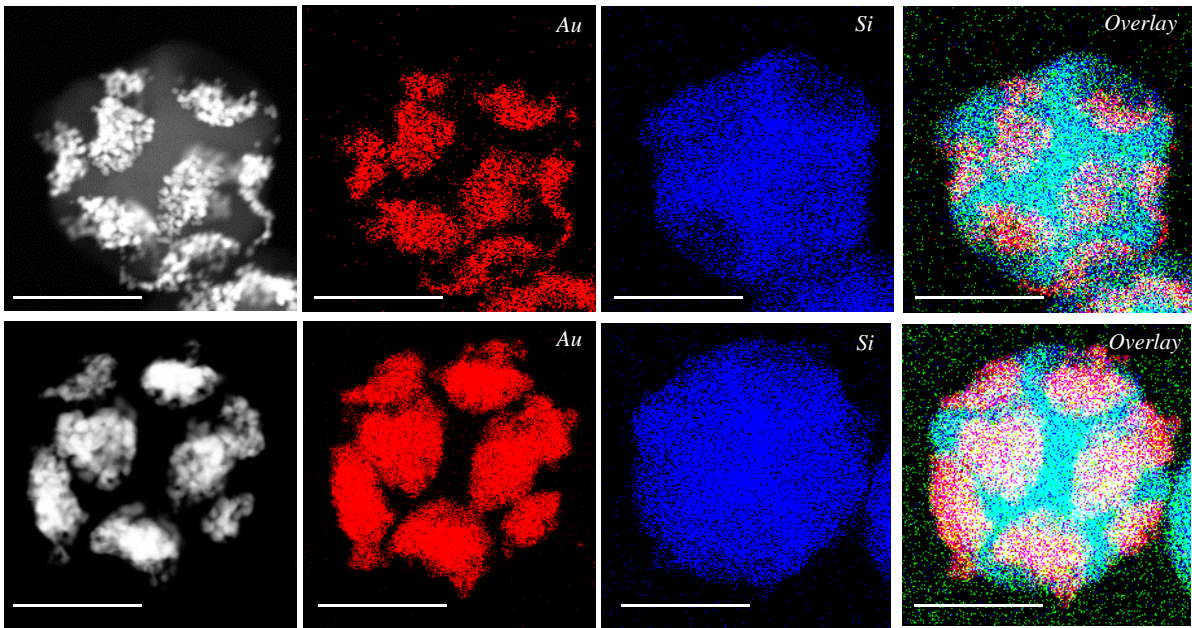


Figure 58: Typical scanning transmission electron micrographs and EDX mapping of the: (upper) GDC-1) and (bottom) GDC-4. Scale bars: 100 nm

Whatever the amount of the gold precursor, the twelve gold deposits consist of agglomerates of gold NPs (Figure 59).

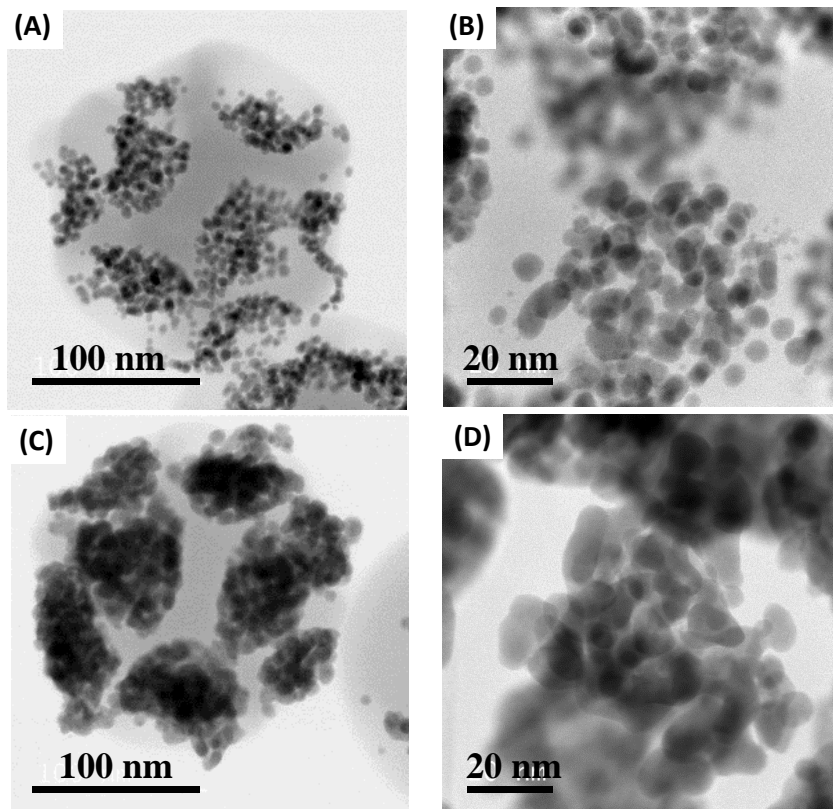
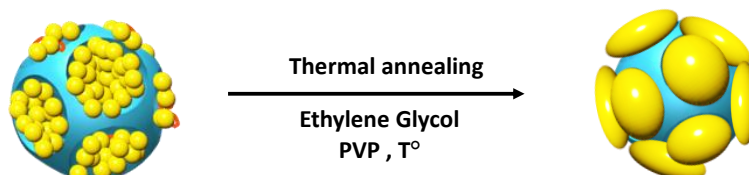


Figure 59: TEM images of: (A), (C) a single GDC-1 and GDC-4; (C) (D) High magnification image of the dimples of GDC-1 and GDC-4.

2. Stage VI: densification of the gold satellites of the GDC clusters

In order to densify the gold agglomerates within each dimple into a dense gold satellite, we performed thermal annealing of the solution GDC-4 in ethylene glycol (Table 6). This procedure is a well-known procedure to densify metallic NPs [25,26].



Scheme 9: Strategy to obtain an optimized GDC with dense gold satellites

Protocol 16: Thermal treatment of the GDC.

2 mL of GDC-4 ($4.5 \cdot 10^{10}$ NPs) obtained after successive growth of the gold seeds using 6 mL of GPS are transferred into 20 mL of ethylene glycol by centrifugation. Subsequently, the dispersion is heated at a given temperature, under reflux and moderated agitation. Finally the suspension is allowed to cool down, then diluted into 20 mL acetone and washed once by centrifugation (2,000 g; 15 min), and then twice in 2 mL of water and PVP (10 g/L).

2.1 Investigation of the thermal annealing on the densification of the satellites

Representative TEM images of GDC-4 before and after a 10 min annealing treatment at 200°C are shown in Figure 60. The coalescence of the gold NPs into dense satellites is clearly observed. Figure 61 shows the optical changes observed upon thermal annealing. Starting from the original purple colloidal dispersions with its dominant plasmon resonance at around 600 nm, the main plasmonic band first slightly shifts to the blue and narrows upon annealing treatment. Similar spectral observations were reported by the group of Halas *et al.* in the case of silica@gold core-shell nanostructures [27]. For longer annealing treatment, the plasmon resonance peak decreases in intensity, and almost vanishes completely after 1h30.

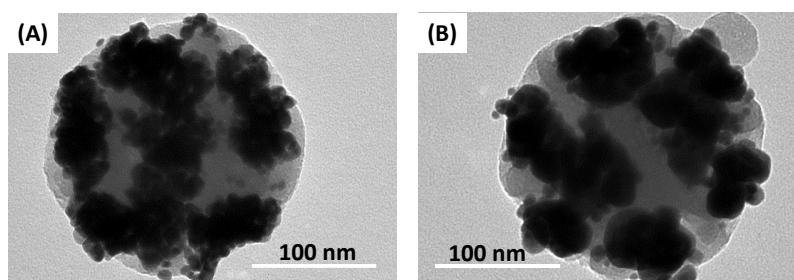


Figure 60: Typical TEM images of the GDC-4 before (A) and after (B) a 10 min thermal treatment at 200°C.

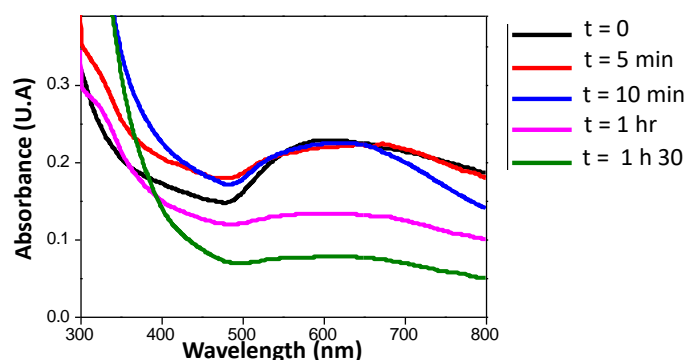


Figure 61: Evolution of the UV absorption spectra of the GDC-4 as the function of the thermal treatment ($T = 200^\circ\text{C}$) duration.

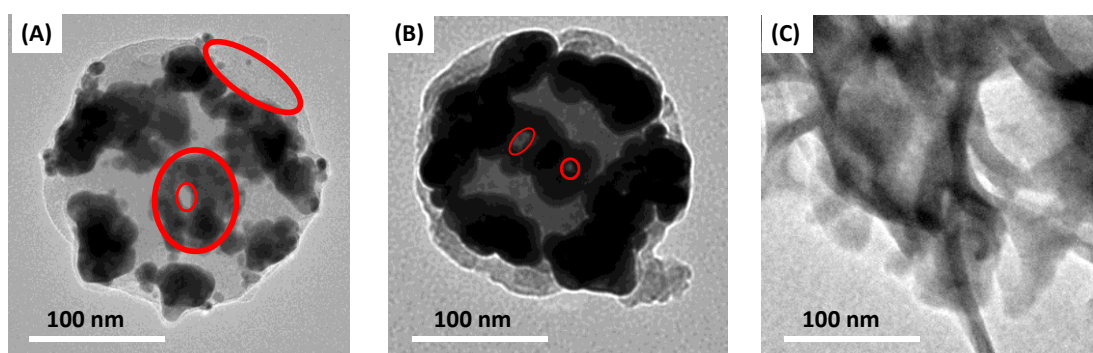


Figure 62: TEM images of GDC-4 after an annealing treatment at 200°C of: (A)-(B) 30 min; (C) 1h30.

This extinction decreases is due to the detachment of the gold particles from the DDS particles (Figure 62A-B). Thus, rather than undergoing gradual densification of the satellites, a mixture of DDS and gold particles was formed (Figure 62C).

In order to optimize the annealing treatment conditions, experiments were carried out at 160°C and 110°C . The results obtained under these conditions are shown in Figure 63 and Figure 64. Similar variation of the optical properties was observed at short annealing times, *i.e.* a progressive blue-shift and narrowing of the plasmon band.

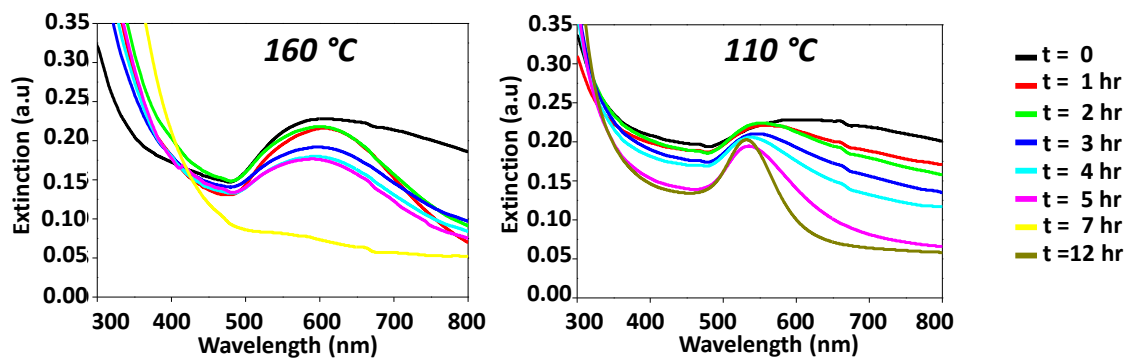


Figure 63: Evolution of the extinction UV-Vis spectra of GDC-4 suspension as a function of the thermal annealing duration at (A) $T = 160^\circ\text{C}$; (B) $T = 110^\circ\text{C}$.

The micrographs of the transformation pathway under these conditions are shown in Figure 64. The densification of the gold satellites is more effective at 160°C than at 110°C after 1 h. At longer times, for both temperatures, the size of the satellites decreases, indicating their dissolution or the detachment of gold NPs.

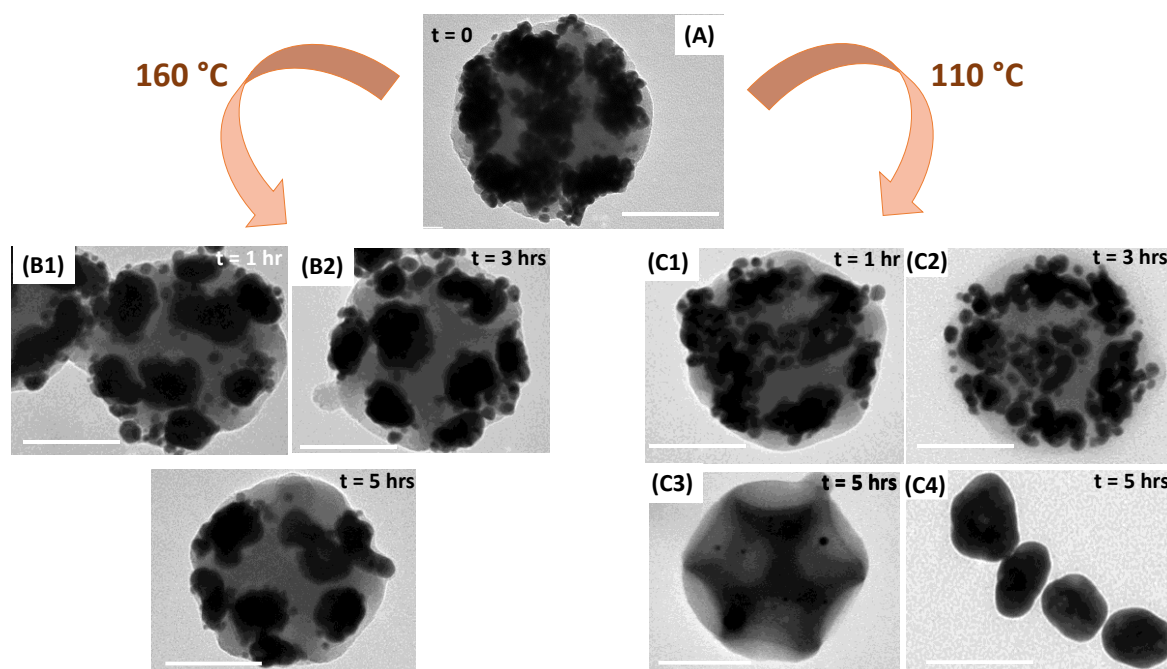


Figure 64: TEM images of GDC-4: (A) before thermal annealing; after thermal annealing at: (A) 160 °C or (C) 110 °C (C). The annealing duration is indicated on each image. Scale bar: 100 nm

In summary, the densification of the gold satellites within the dimples is a tricky and challenging step. Several mechanisms are involved during the thermal annealing: the diffusion of the gold particles as well as their coalescence. Thermal annealing at 200°C for 10 min are the optimal conditions for the densification of gold NPs in the dimples.

2.2 Characteristics of the GDC after densification

STEM, HR-TEM and EDX images of a single GDC obtained before and after 10 min of thermal annealing at 200°C are shown on Figure 65. They clearly evidenced the densification of the gold within the dimples.

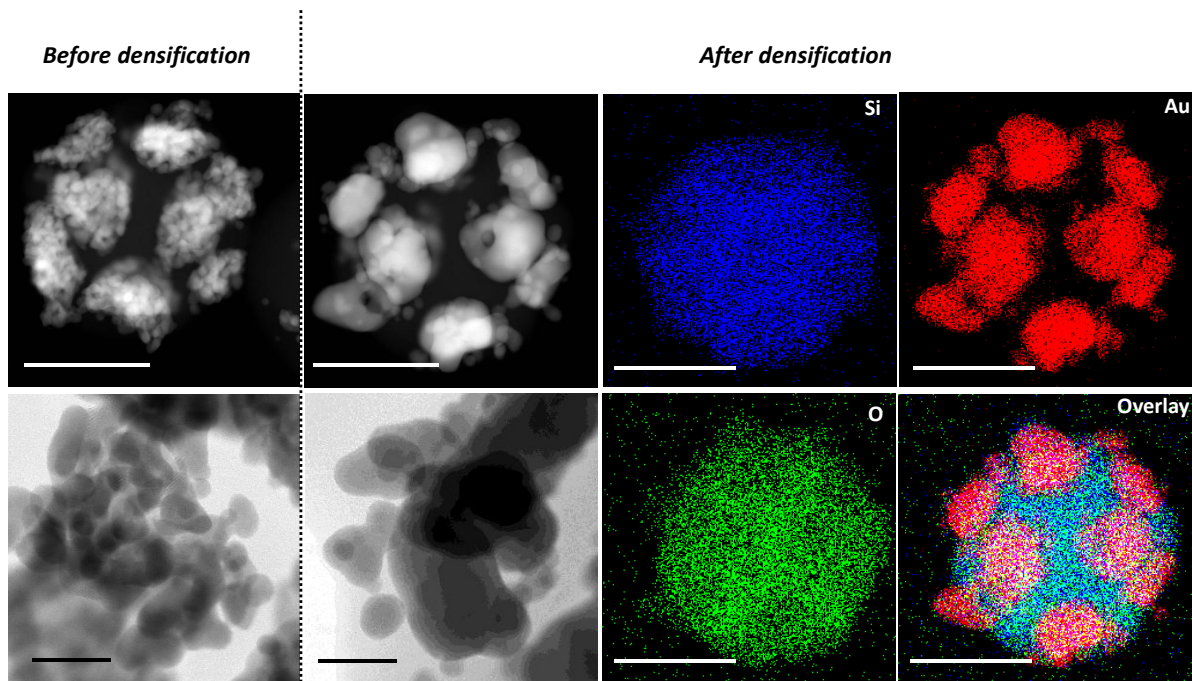


Figure 65: Typical scanning transmission electron images and EDX mapping of GDC-4: before and after the densification at 200 °C during 10 min (scale bars: 100 nm) and corresponding zooms on a satellite (scale bars: 20 nm).

The final GDC-4 are made of satellites of 65 nm and a gap of 17 nm. Figure 66 shows SEM of a typical batch of isotropic gold satellites. They can be synthesized in large amount with a high purity.

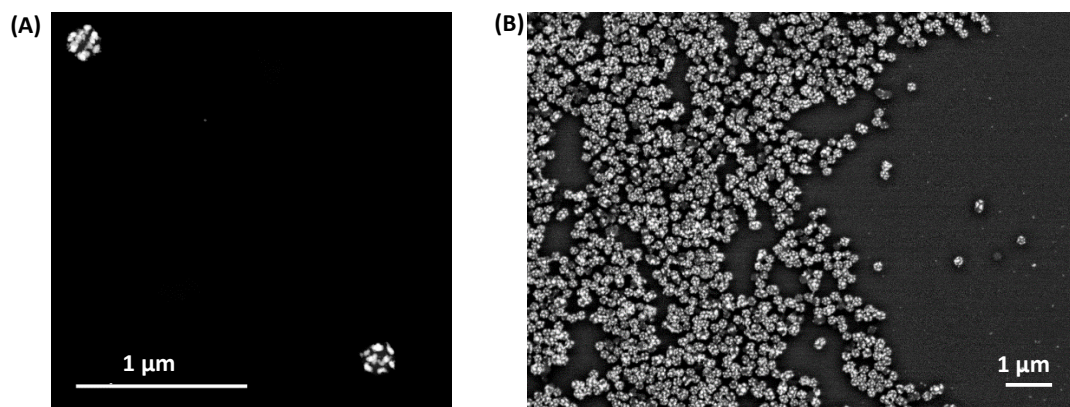


Figure 66: (A) STEM image and (B) SEM image of the GDC-4 after densification of the gold satellites.

2.3 Extension of the densification for GDC with increasing satellites size

The densification procedure was extended to different batches of clusters containing gold satellites of different size i.e. obtained upon the addition of 0.92 mM, 1.22 mM and 1.40 mM GPS, denoted as GDC-4, GDC-5 and GDC-6, respectively. Systematically one observed a narrowing of the main absorption band of the different colloidal suspension after the densification process (Figure 67).

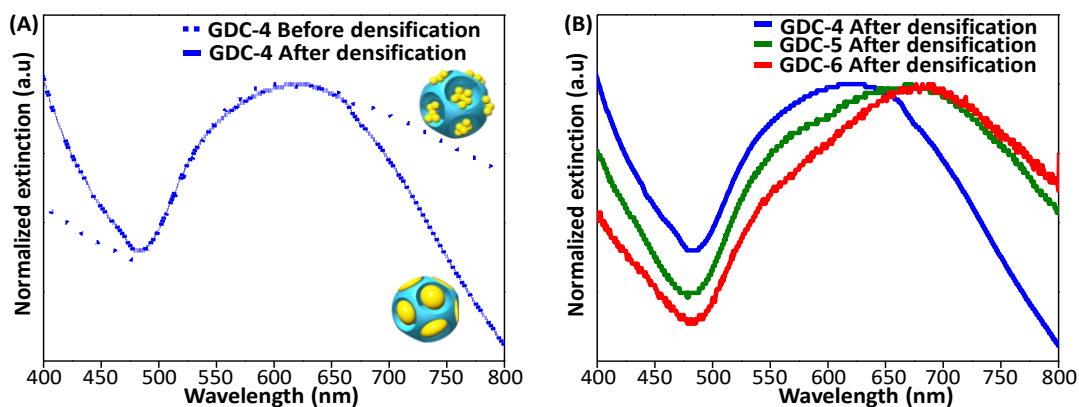


Figure 67: Extinction UV-Vis spectra of GDC (A) before and (B) after densification of the gold satellites with increasing amount of GPS.

3. Stage VII: investigation of the magnetic and electric responses of the GDC by static light scattering

3.1 Static light scattering principle

Following a method previously described, the scattering properties of GDC in suspension were investigated across the whole visible spectrum by a polarization resolved light scattering setup (Figure 68) [28,29].

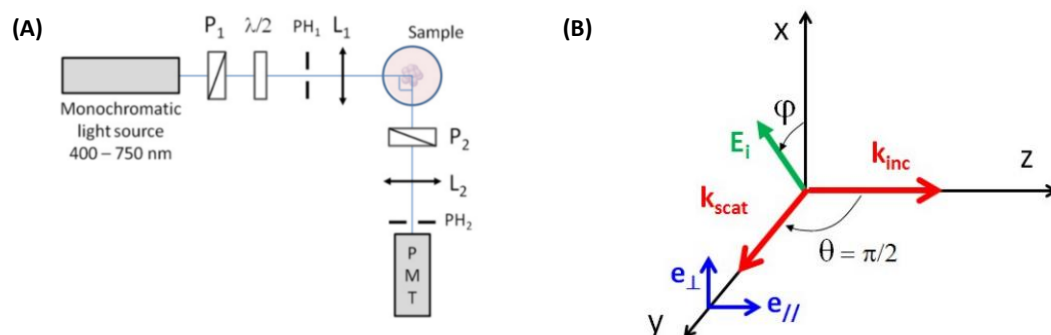


Figure 68: Schematic view of: (A) light scattering setup and (B) the light scattering geometry

In this setup, a monochromatic light beam is delivered by a supercontinuum white source. This light propagating along z can be linearly polarized in the (x,y) plane at angle ϕ from the x axis perpendicular to the scattering plane (y,z) (Figure 68). This polarization is induced by a first Glan-Taylor polarizer mounted on a rotation stage to rotate the incident polarization by a ϕ angle. Therefore, when the polarized light is sent to a particle, the light will be scattered all around the direction. Thus, the photomultiplier tube coupled with a photon counting unit at a fixed scattering angle $\theta = 90^\circ$ enables to collect specifically the scattering intensities I_\perp or I_\parallel for different ϕ angles. This investigation is monitored across the whole visible spectrum. The

polarization of the scattered light was analyzed by a Glan-Taylor polarizer set perpendicular or parallel to the scattering plane to collect the I_{\perp} or $I_{//}$ signals, respectively.

Thus, the scattering intensity I_{\perp} or $I_{//}$ can be defined as:

$$I_{\perp S} = I_0(\lambda)N_{DDP} \frac{|S_1(\theta=90^\circ)|^2}{k^2} \delta\Omega g(\lambda, \delta\Omega) \cos^2 \varphi = A_{\perp}(\lambda) \cos^2 \varphi$$

Equation 12

$$I_{//S} = I_0(\lambda)N_{DDP} \frac{|S_2(\theta=90^\circ)|^2}{k^2} \delta\Omega g(\lambda, \delta\Omega) \sin^2 \varphi = A_{//}(\lambda) \sin^2 \varphi$$

Equation 13

where $I_0(\lambda)$ is the spectral irradiance of the incident beam, N_{DDP} is the number of GDC in the scattering volume, and $\delta\Omega$ is the solid angle of the detection window, $g(\lambda, \delta\Omega)$ is an unknown function that accounts for the spectral sensitivity of the detector and optical transmission or reflection of all optical elements. At $\theta = 90^\circ$, S1 contains the radiation of the electric dipole and S2 the radiations of the magnetic dipole and the electric quadrupole [29].

Considering the ratio of the axial to transverse scattering $A_{//} / A_{\perp}$ all the unknown functions in Equation 12 and Equation 13 can be eliminated, providing an estimate of the strength of the magnetic dipole MD relative to electric dipole ED:

$$A_{//} / A_{\perp} = \frac{|S_2(\theta=90^\circ)|^2}{|S_1(\theta=90^\circ)|^2} = \frac{MD+EQ}{ED} \approx \frac{MD}{ED}$$

Equation 14

Thus, the parallel MD+EQ scattering cross-sections can be extracted by normalizing the data with a reference dispersion of calibrated silica NPs ($D_{SiO_2} = 95$ nm) in water [28]:

$$\sigma_{//}^{MD+EQ}(\theta = \varphi = 90^\circ) = \frac{|S_2(\theta=90^\circ)|^2}{k^2} = K \frac{A_{//}(\lambda)}{A_{ref}(\lambda)} \sigma_{ref}^{\theta=90^\circ; \varphi=0}(\lambda)$$

Equation 15

where $\sigma_{ref}^{\theta=90^\circ; \varphi=0}$ is the scattering cross section of a silica particle in water at scattering angles $\theta = \pi/2$, $\varphi = 0$ (calculated from the Mie theory and scales as $1/\lambda^4$), and $K = N_{ref} / N_{DDP}$ is the concentration ratio. The GDC and silica signals were collected in the same experimental conditions so that the quantities I_0 , $\delta\Omega$, and $g(\lambda, \delta\Omega)$ are the same for GDC and for the reference.

3.2 Influence of the satellites size of GDC and their densification in their scattering properties

The scattering intensities $I_{\perp}(\lambda)$ and $I_{//}(\lambda)$ versus the angle φ of the incident polarization, of GDC-6 are illustrated in Figure 69, at $\lambda = 640.5$ nm. They are fitted for each wavelength to $B + A_{\perp} \cos^2\varphi$ and $B + A_{//} \sin^2\varphi$ functions, respectively. The background signal B , identical for the two functions, does not exceed a few percent (2 to 5% across the wavelength range) of the amplitude A_{\perp} , hence confirming the isotropic response of the GDC.

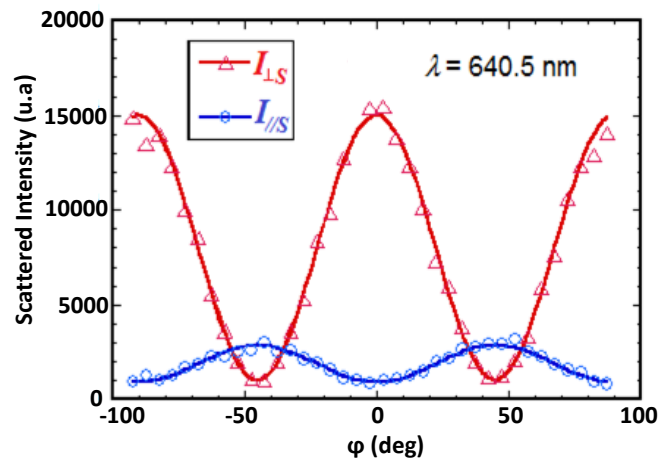


Figure 69: Signal scattered along the two output polarization channels I_{\perp} and $I_{//}$, perpendicular and parallel to the scattering plane, respectively. The solid lines are a fit to the $\cos^2\varphi$ and $\sin^2\varphi$ functions, respectively.

The scattering intensity $A_{//} / A_{\perp}$, which is an indicator of the MD/ED ratio is plotted vs. wavelength for all GDC in Figure 70. It exhibits for all samples a broad maximum in the visible range. The maximum red-shifts and increases upon increasing the amount of GPS solution from ~5% to ~9% for non-condensed GDC. Densification of the satellites at constant amount of gold further increases the maxima from ~9% to ~14%.

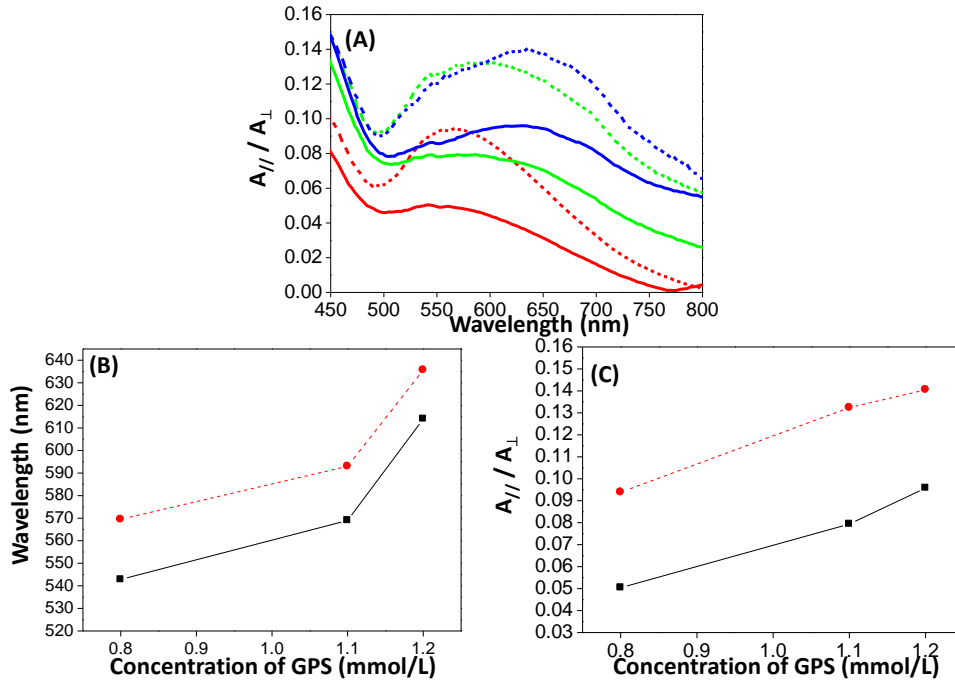


Figure 70: (A) Ratio of axial to transverse scattering $A_{//} / A_{\perp}$ vs. wavelength of the GDC obtained after the addition of 0.92 mmol/L (red curves); 1.22 mmol/L (green curves) and 1.40 mmol/L of GPS (blue curves); and before (solid line) and after densification (dash line); (B) Plot of the wavelength of the maximal $A_{//} / A_{\perp}$ versus the GPS concentration (C) plot of the the $A_{//} / A_{\perp}$ maximum value versus the GPS concentration for GDC-4, GDC-5 and GDC-6 before (solid line) and after densification (dash line).

For comparison, the data measured on gold raspberries made of a silica core of 100 nm and gold satellites of 30 nm are shown in Figure 71 (red curve) [28]. It reveals an improvement of the ratio from 4.2% for gold raspberries (disordered plasmonic clusters) to 14% for GDC-3 (gold icosahedral clusters of similar size).

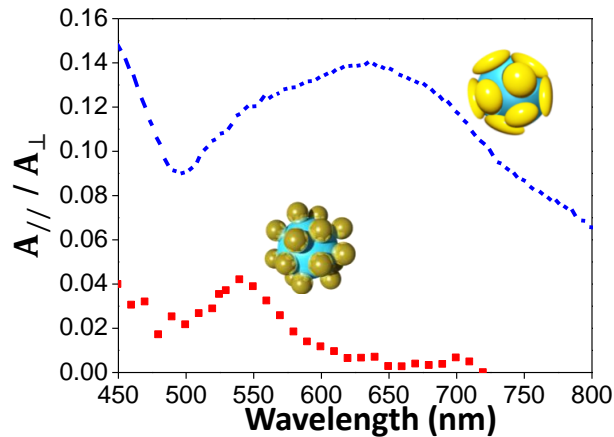


Figure 71: Comparison of the $A_{//} / A_{\perp}$ ratio of the GDC-6 and the gold raspberries made of a silica core (100 nm) of and 26 gold satellites of 30 nm.

The normalized cross sections $\sigma_{//}^{MD+EQ}(\theta = \varphi = \pi/2)$ of the 3 batches of GDC are shown in Figure 72. The three curves exhibit a clear resonance which red-shifts and broadens with increasing gold amount.

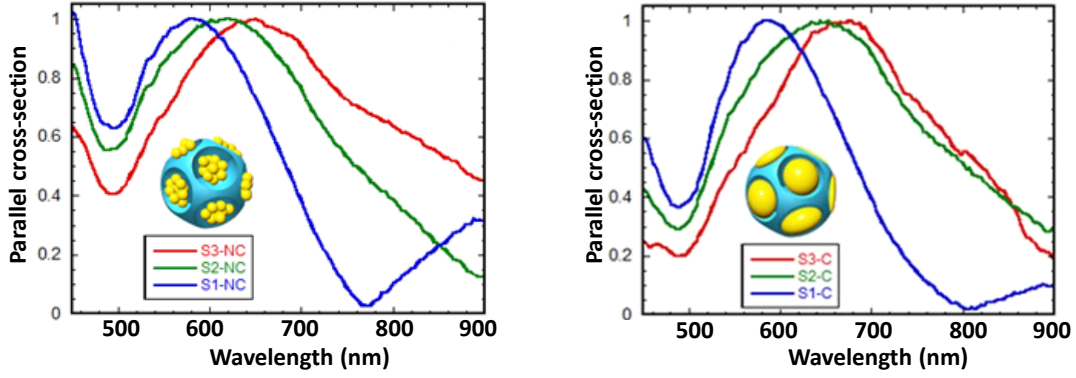


Figure 72: Parallel scattering cross-section $\sigma_{\parallel}^{MD+EQ}$ of the samples: GDC-4 (blue curve), GDC-5 (green curve) and GDC-6 (red curve) before (left) and after (right) densification.

3.3. Numerical investigations

In the previous section, the condensed GDC have proven to generate a magnetic-to-electric dipole ratio which is three times higher than gold raspberries of similar size. This is a clear success of the new morphology. Numerical investigations were carried out to compute the scattering properties of the GDC by using two different structural models: Generalized Multi-particle Mie (GMM) theory, GDC before densification and finite element method (FEM) for GDC after densification.

3.3.1 Numerical investigations of the GDC before densification

The simulated GDC are shown in the inset of Figure 73A. Twelve satellite spheres of radius R_{sat} are partially filled with spherical gold NPs of radius R_{Au} inside the volume of a truncation sphere of radius R_{trunc} . These volumes are filled with non-intersecting gold nanospheres of radius $R_{Au} = 5$ nm with a volume fraction set to 40%. The volume of the aggregates, controlled by R_{trunc} , is given as a percentage of the volume of the full satellite sphere $4/3\pi.R_{sat}^3$. Increasing the amount of gold from GDC-4 to GDC-6 may be produced by increasing R_{trunc} (bigger agglomerate) and/or increasing R_{Au} (higher volume fraction of gold within each agglomerate). Figure 73 shows that the experimental values of the magnetic-to-electric ratio A_{\perp}/A_{\parallel} shown in Figure 70A (dashed lines) are very well reproduced by the model of aggregates of gold NPs of radius 5 nm. Increasing the amount of gold in the model either by increasing the volume of the aggregate (via R_{trunc}) or the size of the gold NPs (R_{Au}) enhances the magnetic response as observed experimentally. However, the experimental red-shift observed upon increasing the amount of gold is only reproduced by increasing the size of the gold NPs within the aggregates, which in turn reduces their average separation. This effect is consistent with the well-known plasmon ruler law stating that the resonance wavelength of

a set of gold NPs red-shifts as the separation of the NPs is reduced[30]. This observation indicates that the size, and not just the number, of the gold grains increases upon successive regrowth steps.

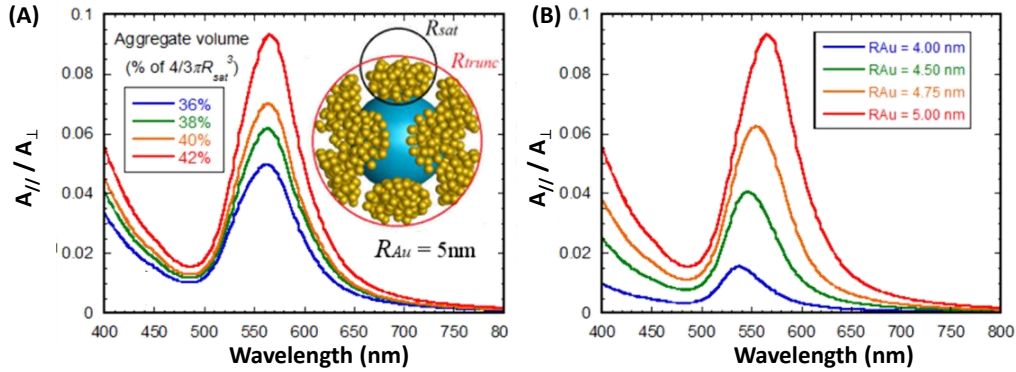


Figure 73: Plot of the computed magnetic to electric estimator A_{\perp}/A_{\parallel} vs. wavelength: (A) for different volumes of gold aggregates in non-condensed GDC; (B) at constant aggregate size, but for different radii R_{Au} .

3.3.2 Numerical investigations of the GDC after densification

Four systems were considered, one for each volume of gold considered in the non-condensed case shown in Figure 73A. The gold dimples are obtained by keeping the intersections of a core-sphere of radius R'_{trunc} with satellite spheres of radius R_{sat} . Of course R'_{trunc} is not equal to R_{trunc} as it sets so as to conserve the volume of gold in the system. Figure 74A shows an illustration of the computed GDC (inset), and it illustrates how A_{\perp}/A_{\parallel} evolves as a function of wavelength. We see a clear increase in the amplitude of this magnetic-to-electric ratio as well as a red-shift in the resonance wavelength compared to the non-condensed case (Figure 73A), in accordance with the experimental observations.

The experimental behavior is qualitatively reproduced and we may discuss the reasons for which differences still remain, namely that the maximum value of A_{\perp}/A_{\parallel} ($\sim 0.10-0.14$) is significantly lower compared to the numerical case (~ 1) and the red-shift is not as large. The densification process actually dewets the gold such that the shape does not necessarily conform to the same shape—intersection of two spheres resulting in a lens-like shape—as that which we simulate. This means that each satellite will take on a shape that is different to the lens shape and is probably more spheroidal. In the end, the simulated patches are thinner than the experimental ones resulting in larger aspect ratios which are known to resonate at higher wavelengths compared to smaller aspect ratios [31]. Furthermore, the lens-shape is actually sharp along the edges, which will result in larger local fields than in the experimental case. Consequently, the capacitive effect is increased between satellites, which produce larger

polarization currents and result in a larger magnetic dipole moment, hence the higher values of the magnetic-to-electric scattering ratio.

As shown by Figure 74B, densification drastically increases the amplitude of the scattering-cross sections of all multipoles present, but the magnetic dipole is the resonance for which the effect is the most dramatic. This reveals the positive role of densification of the magneto-optical properties of such systems. Furthermore, we see that the magnetic resonance of the condensed system converges toward that of the ideal GDC (Figure 24). The peak reaches a scattering cross-section of 10^5 nm^2 at a wavelength of 715 nm for the ideal case, while the theoretical GDC reaches $\sim 2 \times 10^4 \text{ nm}^2$ at a wavelength close to 707 nm.

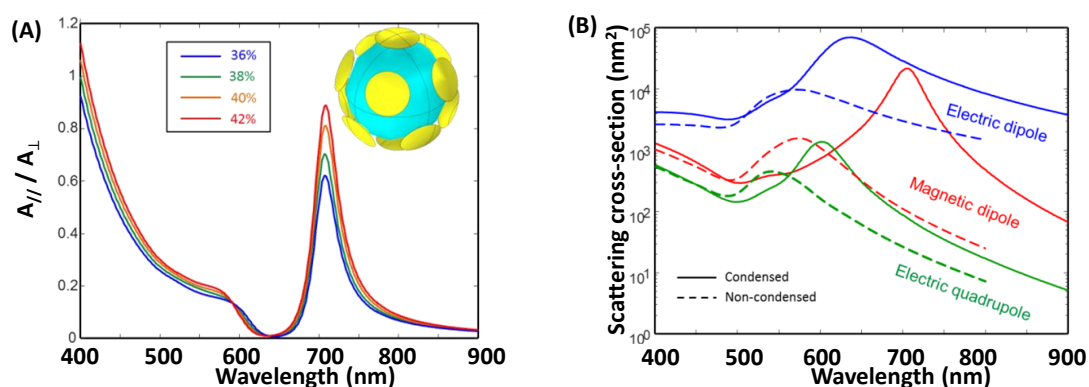


Figure 74: (A) Plot of the computed magnetic to electric estimator A_{\perp}/A_{\parallel} vs. wavelength: (A) for different volumes of gold aggregates in condensed GDC. The inset represents a typical model of the GDC used in the finite element simulation. (b) Simulated scattering cross-sections of the electric (blue) and magnetic dipoles (red) as well as the electric quadrupole (green) in both the non-condensed (dashed line) and condensed (continuous line) cases.

4. Conclusion

In this chapter, we have detailed an efficient protocol for the fabrication of gold dodecapods by seeded growth method. We optimized each step of the synthesis of these nano-objects. Dissolution of the clusters happened during the growth of the gold seeds by using a “fresh” solution of gold precursor (GPS). The dissolution of the nanoclusters is GPS age dependent. We observed that the older the GPS age, the more stable the clusters were. This dissolution was assigned to the reaction in between the counter ions of the gold precursor and the silica. By optimizing the experimental procedure, step by step, we could synthesize gold dodecapods in large amount with a high purity.

We demonstrated that these nano-objects have unique plasmonic properties which can be modulated by the satellites size, and their in-between gap. These gold dodecapods exhibit, in particular, an high magnetic response[32]. The magnetic-to-electric polarization ratio is more

than three times higher than the reference value measured on “conventional” gold raspberries of similar size [28]. This experimental result shows that the regular organization of the satellites around the core is more efficient than a random distribution for the generation of a magnetic current. Controlling the uniform separation of the satellites in a regular distribution warrants a constant satellite-to-satellites interaction and therefore a sharper resonance.

We noticed the presence of few small size gold particles in between the 12 satellites. Those small particles may affect the scattering properties of the gold dodecapods. Thus, we implemented some preliminary tests to etch those tiny particles using KI as an oxidizing agent by tuning the concentration of the oxidative agent from 10 mM to 70 mM (Figure 75) [32-35]. 30 mM of KI represents the conditions to remove most of the tiny particles.

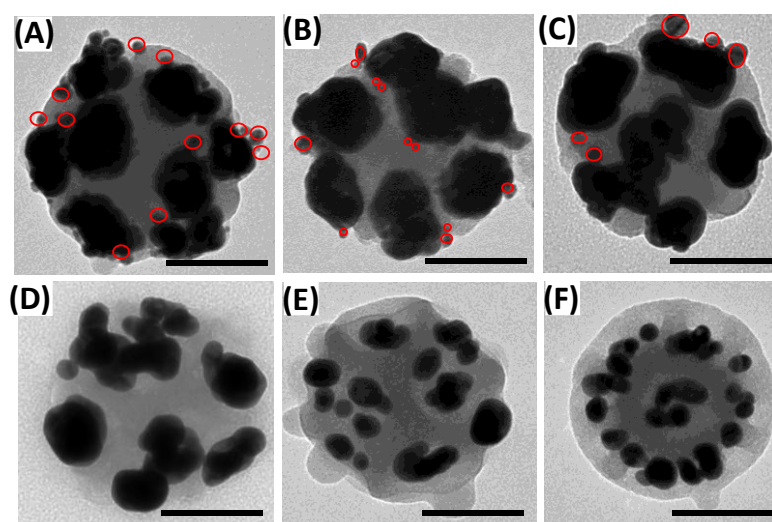


Figure 75: TEM images of the gold dodecapods after etching by KI with a concentration of: (A) 10 mM; (B) 20 mM, (C) 30 mM, (D) 40 mM, (E) 50 mM, and (F) 70 mM.

Further work will definitely have to explore the best conditions to the synthesis of gold dodecahedral clusters without tiny imperfections in between the satellites.

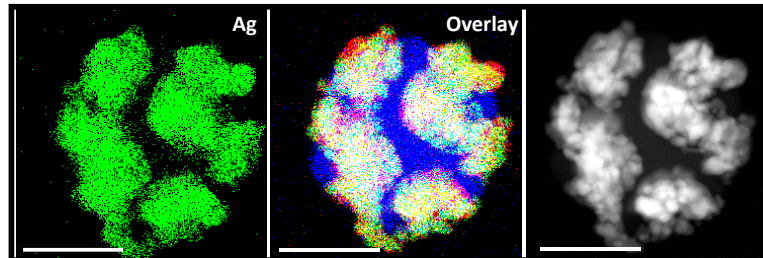
5. References

- [1] C. Chomette, M. Tréguer-Delapierre, N. B. Schade, V. N. Manoharan, O. Lambert, J.-C. Taveau, S. Ravaine, and E. Duguet, “Colloidal Alchemy: Conversion of Polystyrene Nanoclusters into Gold,” *ChemNanoMat*, vol. 3, no. 3, pp. 160–163, 2017.
- [2] C. Chomette, “Thèse de l’université de Bordeaux: Design and synthesis of plasmonic meta-atoms from patchy particles,” 2015.
- [3] D. G. Duff, A. Baiker, and P. P. Edwards, “A new hydrosol of gold clusters. 1. Formation and particle size variation,” *Langmuir*, vol. 9, no. 9, pp. 2301–2309, 1993.
- [4] S. J. Oldenburg, R. D. Averitt, S. L. Westcott, and N. J. Halas, “Nanoengineering of optical resonances,” *Chem. Phys. Lett.*, vol. 288, no. 2, pp. 243–247, 1998.
- [5] Z. Liang, Y. Liu, S. S. Ng, X. Li, L. Lai, S. Luo, and S. Liu, “The effect of pH value on the

- formation of gold nanoshells,” *J. Nanoparticle Res.*, vol. 13, no. 8, pp. 3301–3311, 2011.
- [6] X. W. Lou, C. Yuan, E. Rhoades, Q. Zhang, and L. A. Archer, “Encapsulation and Ostwald Ripening of Au and Au–Cl Complex Nanostructures in Silica Shells,” *Adv. Funct. Mater.*, vol. 16, no. 13, pp. 1679–1684, 2006.
- [7] S.-E Park; M.-Y Park; P.-K Han; S.-W Lee, “The Effect of pH-adjusted Gold Colloids on the Formation of Gold Clusters over APTMS-coated Silica Cores,” *Bull. Korean Chem. Soc.*, vol. 27, no. 9, pp. 1341–1345, 2006.
- [8] S. L. Westcott, S. J. Oldenburg, T. R. Lee, and N. J. Halas, “Formation and Adsorption of Clusters of Gold Nanoparticles onto Functionalized Silica Nanoparticle Surfaces,” *Langmuir*, vol. 14, no. 19, pp. 5396–5401, 1998.
- [9] M. R. Rasch, K. V Sokolov, and B. A. Korgel, “Limitations on the Optical Tunability of Small Diameter Gold Nanoshells,” *Langmuir*, vol. 25, no. 19, pp. 11777–11785, 2009.
- [10] B. J. Jankiewicz, D. Jamiola, J. Choma, and M. Jaroniec, “Silica–metal core–shell nanostructures,” *Adv. Colloid Interface Sci.*, vol. 170, no. 1, pp. 28–47, 2012.
- [11] S.-H. Wu, C.-Y. Mou, and H.-P. Lin, “Synthesis of mesoporous silica nanoparticles,” *Chem. Soc. Rev.*, vol. 42, no. 9, pp. 3862–3875, 2013.
- [12] J. V. Brady, P. V., Walther, “Controls on silicate dissolution rates in neutral and basic pH solutions at 25°C,” *Geochim. Cosmochim. Acta*, vol. 53, no. 11, p. 2823, 1989.
- [13] S. H. Chan, “A review on solubility and polymerization of silica,” *Geothermics*, vol. 18, no. 1, pp. 49–56, 1989.
- [14] T. M. Seward, “Determination of the first ionization constant of silicic acid from quartz solubility in borate buffer solutions to 350°C,” *Geochim. Cosmochim. Acta*, vol. 38, no. 11, pp. 1651–1664, 1974.
- [15] A. C. Makrides, M. Turner, and J. Slaughter, “Condensation of silica from supersaturated silicic acid solutions,” *J. Colloid Interface Sci.*, vol. 73, no. 2, pp. 345–367, 1980.
- [16] S. El Mourabit, M. Guillot, G. Toquer, J. Cambedouzou, F. Goettmann, and A. Grandjean, “Stability of mesoporous silica under acidic conditions,” *RSC Adv.*, vol. 2, no. 29, pp. 10916–10924, 2012.
- [17] C. Boissière, A. Larbot, C. Bourgaux, E. Prouzet, and C. A. Bunton, “A Study of the Assembly Mechanism of the Mesoporous MSU-X Silica Two-Step Synthesis,” *Chem. Mater.*, vol. 13, no. 10, pp. 3580–3586, 2001.
- [18] H.-P. Boehm, “The Chemistry of Silica. Solubility, Polymerization, Colloid and Surface Properties, and Biochemistry,” *Angew. Chemie*, vol. 92, no. 4, p. 328, 1980.
- [19] P. M. Dove and D. A. Crerar, “Kinetics of quartz dissolution in electrolyte solutions using a hydrothermal mixed flow reactor,” *Geochim. Cosmochim. Acta*, vol. 54, no. 4, pp. 955–969, 1990.
- [20] L. I. U. Shunying, L. Zhongshi, G. A. O. Feng, Y. U. Jiahui, L. U. O. Shufang, C. J. N., and L. U. Guoquan, “A Facile Approach to the Synthesis of Gold Nanoshells with Near Infrared Responsive Properties,” *Chinese J. Chem.*, vol. 27, no. 6, pp. 1079–1085, 2009.
- [21] J. D. Rimstidt and H. L. Barnes, “The kinetics of silica-water reactions,” *Geochim. Cosmochim. Acta*, vol. 44, no. 11, pp. 1683–1699, 1980.
- [22] A. Lasaga, “Chemical kinetics of water-rock interactions,” *J. Geophys. Res.*, vol. 89, pp. 4009–4025, 2018.

- [23] H. Kamiya, K. Shimokata, “The role of salts in the dissolution of powdered quartz,” in *Proceedings of International Symposium of Water-rock Interaction (eds. J. Cadek and T. Paces)*, 1976.
- [24] D. L. Dugger, J. H. Stanton, B. N. Irby, B. L. McConnell, W. W. Cummings, and R. W. Maatman, “The Exchange of Twenty Metal Ions with the Weakly Acidic Silanol Group of Silica Gel 1,2,” *J. Phys. Chem.*, vol. 68, no. 4, pp. 757–760, 1964.
- [25] G. Casillas, J. J. Velázquez-Salazar, and M. Jose-Yacaman, “A New Mechanism of Stabilization of Large Decahedral Nanoparticles,” *J. Phys. Chem. C*, vol. 116, no. 15, pp. 8844–8848, 2012.
- [26] Y. Wang, Y. Wang, X. Zheng, É. Ducrot, M.-G. Lee, G.-R. Yi, M. Weck, and D. J. Pine, “Synthetic Strategies Toward DNA-Coated Colloids that Crystallize,” *J. Am. Chem. Soc.*, vol. 137, no. 33, pp. 10760–10766, 2015.
- [27] C. Radloff and N. J. Halas, “Enhanced thermal stability of silica-encapsulated metal nanoshells,” *Appl. Phys. Lett.*, vol. 79, no. 5, pp. 674–676, 2001.
- [28] V. Ponsinet, P. Barois, S. M. Gali, P. Richetti, J. B. Salmon, A. Vallecchi, M. Albani, A. Le Beulze, S. Gomez-Grana, E. Duguet, S. Mornet, and M. Treguer-Delapierre, “Resonant isotropic optical magnetism of plasmonic nanoclusters in visible light,” *Phys. Rev. B*, vol. 92, no. 22, p. 220414, 2015.
- [29] N. L. Sharma, “Nondipole Optical Scattering from Liquids and Nanoparticles,” *Phys. Rev. Lett.*, vol. 98, no. 21, p. 217402, 2007.
- [30] S. Gomez-Graña, M. Treguer-Delapierre, E. Duguet, J. B. Salmon, J. Leng, V. Kravets, A. N. Grigorenko, A. Peyyety, V. Ponsinet, P. Richetti, A. Baron, D. Torrent-Marti, and P. Barois, “Isotropic 3D optical magnetism in visible light in a self-assembled metamaterial,” in *proceeding of the 10th International Congress on Advanced Electromagnetic Materials in Microwaves and Optics (Metamaterial)*, 2016, pp. 52–54.
- [31] V. Amendola, O. M. Bakr, and F. Stellacci, “A Study of the Surface Plasmon Resonance of Silver Nanoparticles by the Discrete Dipole Approximation Method: Effect of Shape, Size, Structure, and Assembly,” *Plasmonics*, vol. 5, no. 1, pp. 85–97, 2010.
- [32] C. R. Simovski and S. A. Tretyakov, “Model of isotropic resonant magnetism in the visible range based on core-shell clusters,” *Phys. Rev. B*, vol. 79, no. 4, p. 45111, 2009.
- [33] Y.-J. Lee, N. B. Schade, L. Sun, J. A. Fan, D. R. Bae, M. M. Mariscal, G. Lee, F. Capasso, S. Sacanna, V. N. Manoharan, and G.-R. Yi, “Ultraspherical, Highly Spherical Monocrystalline Gold Particles for Precision Plasmonics,” *ACS Nano*, vol. 7, no. 12, pp. 11064–11070, 2013.
- [34] B. Tang, S. Xu, J. An, B. Zhao, W. Xu, and J. R. Lombardi, “Kinetic effects of halide ions on the morphological evolution of silver nanoplates,” *Phys. Chem. Chem. Phys.*, vol. 11, no. 44, pp. 10286–10292, 2009.
- [35] S. S. Konyratbekova, A. Baikonurova, G. A. Ussoltseva, C. Erust, and A. Akcil, “Thermodynamic and kinetic of iodine–iodide leaching in gold hydrometallurgy,” *Trans. Nonferrous Met. Soc. China*, vol. 25, no. 11, pp. 3774–3783, 2015.
- [36] L. Chen, F. Ji, Y. Xu, L. He, Y. Mi, F. Bao, B. Sun, X. Zhang, and Q. Zhang, “High-yield seedless synthesis of triangular gold nanoplates through oxidative etching,” *Nano Lett.*, vol. 14, no. 12, pp. 7201–7206, 2014.

Chapter IV :
Extension to silver
dodecahedral clusters

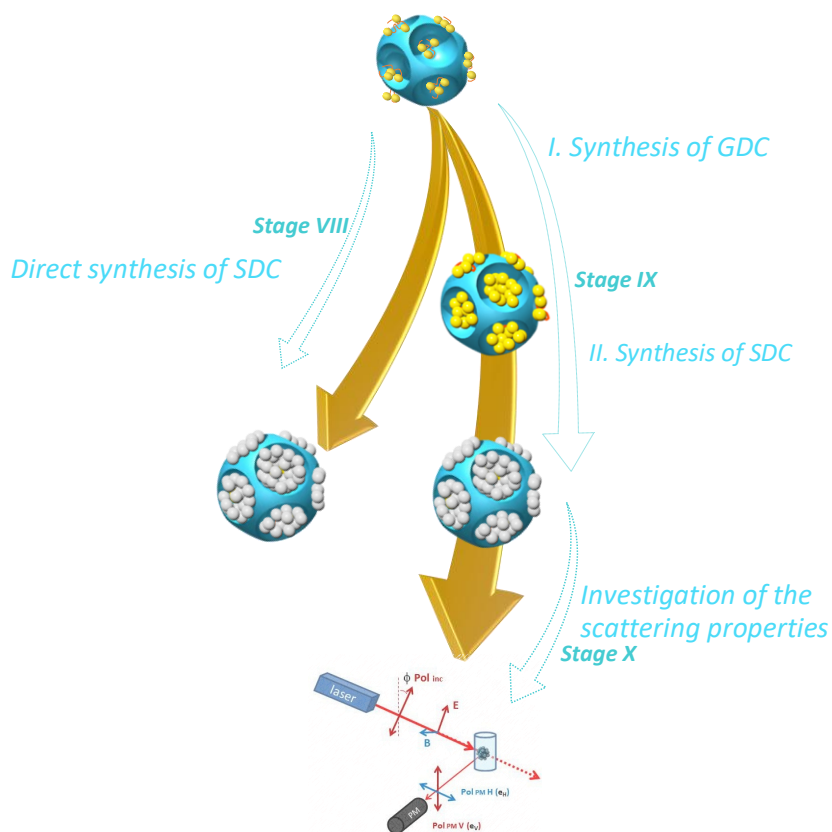


EDX (left and center) and STEM (right) images of SDC (Scale bars: 100 nm)

This chapter deals with the extension of our synthesis strategy to SDC in order to increase the strength of the magnetic response of the nanoresonators at visible light frequencies.

Previous works from our group already reported that raspberry-like nanoclusters made of a random arrangement of silver satellites exhibit a magnetic response at unprecedented level. Their magnetic efficiency was 5.4 times higher than gold raspberries [1,2].

In the present work, our objective for the synthesis of the silver dodecahedral clusters (SDC) was to use a similar strategy than the one adopted in chapter III: adsorption of silver seeds on the functional dodecahedral dimples, regioselective growth of the seeds and densification of the satellites. Unfortunately, the adsorption of silver seeds onto the aminated PS wasn't as efficient as for gold seeds: the adsorption wasn't site-specific and some dimples appeared silver-free. Therefore, we decided to induce the growth of silver satellites via a heterogeneous nucleation approach, *i.e.* from preformed tiny gold seeds anchored onto the dimples. Since silver and gold have a similar crystalline structure (lattice symmetry and lattice constant $a = 0.408$ nm for Au versus 0.409 nm for Ag), the epitaxial overgrowth of silver on gold is expected to do not induce significant interfacial stress and may yield to SDC. The synthesis route adopted is sketched in Scheme 10.



Scheme 10: Strategy to synthesize SDC

1. Stage VIII: Direct silver growth from tiny gold seeds adsorbed within the dimples of the dodecahedral clusters

The seed-mediated growth was initiated using a well-known procedure based on the use of silver nitrate as metal precursor and formaldehyde as a reducing agent. . Experiments were performed following the Protocol 17 (SDC-1 experimental conditions).

Protocol 17: Silver growth on gold seeds anchored on the dimples of the dodecahedral clusters

Typically, 1 mL of the gold seeds adsorbed dodecahedral clusters was centrifuged and redispersed in 13 mL of a PVP solution (10g/L in water) by a typical centrifugation in order to get a gold seeds dodecahedral suspension with a concentration of $2.8 \cdot 10^{13}$ Part./L.

Subsequently, 200 μ L of gold seeds adsorbed dodecahedral clusters were added in a 5 mL flask. A 2 mM aqueous solution of silver salt in water was prepared (2 mM) and a typical volume of the silver salt solution corresponding to the concentration indicated in Table 8, was added to the medium and was homogenized; subsequently 30 μ L of HCHO were added. Before the silver salt addition, a given volume of milliQ[®] water was added to the medium, in order to have a final volume of the reaction medium of 1.5 mL (including the overall reactant volume). The mixture was left to stir overnight.

Table 8: Experimental conditions for the silver growth onto gold seeds adsorbed dodecahedral clusters.

	SDC-1	SDC-2	SDC-3
Number of the gold dodecahedra (ptcs)	$5.6 \cdot 10^9$	$5.6 \cdot 10^9$	$2 \cdot 10^{10}$
[Silver Precursor] mmol/L	1.4	0,7	0,7
Silver precursor type	AgNO ₃	Ag ₂ SO ₄	Ag ₂ SO ₄
V _{HCHO} (μ L)	30	30	30

Under these experimental conditions, the homogeneous nucleation of silver was favored: a large amount of free silver particles was observed in the reaction medium (Figure 76A). Others experiments based on Halas *et al.* were performed adding ammonium hydroxide (NH₄OH) after the addition of the reducing agent in order to promote a pH change and the reduction of Ag⁺ onto gold seeds [3]. However, those experiments failed to promote the heterogeneous nucleation of silver within the dimples.

By using silver sulfate instead of silver nitrate as metallic precursor (SDC-2 experimental conditions), the silver growth occurred more specifically within the dimples. Figure 76B shows typical TEM images of the as-obtained clusters. But, after the growth, the silver structures exhibited quite complex shape. Moreover, all the dimples were not filled with

silver. There was a loss of Ag atoms since free silver nanoparticles were formed in the dispersion. In order to promote the heterogeneous nucleation, the concentration ratio of the dimpled silica nanoparticles to silver precursor was adjusted ($2 \cdot 10^{10}$ dodecahedral clusters instead of $5.6 \cdot 10^9$ dodecahedral clusters). In the experimental conditions of the batch SDC-3, all the dimples were filled with silver. But, the silver satellites were highly irregular in size.

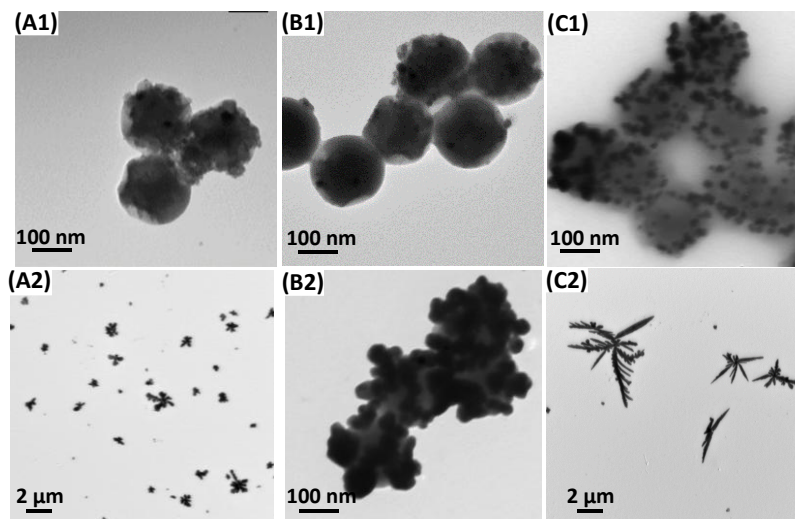


Figure 76: Typical TEM images of the SDC obtained after the silver growth onto gold seeds adsorbed on the dimples: (A) SDC-1 was synthesized using AgNO_3 as silver precursor (B) SDC-2 was synthesized using Ag_2SO_4 as silver precursor and using $5.6 \cdot 10^9$ dodecahedral clusters (C) SDC-3 was synthesized using Ag_2SO_4 as silver precursor and using $2 \cdot 10^{10}$ dodecahedral clusters.

2. Stage IX: Silver growth from tiny gold seeds adsorbed within the dimples of the dodecahedral clusters after a preliminary growth of gold

We tested different approaches in an effort to generate SDC with spheroidal shape satellites. The most robust approach was to monitor a preliminary growth of gold seeds leading to an increase of the concentration and the size of the gold particles anchored onto the dimples. Subsequently, the silver growth was carried out (Scheme 11).



Scheme 11 : Illustration of the strategy to promote the growth of silver within the dimples' surface.

The growth of the gold seeds was performed by using 0.6 mM of GPS in the experimental conditions of the Protocol 15. Under these conditions, the gold growth was confined within the dimples as already demonstrated in Chapter III. Then, the silver growth was induced following the experimental conditions of the Protocol 17 (SDC-4). Figure 77A-B show the

representative TEM images of the clusters obtained before and after the silver regrowth. The satellite size increases after the silver precursor addition indicating that the silver reduction/deposition dominates the growth process rather than the formation of free silver particles. The silver satellites were highly faceted and hanged over the dimples. By adjusting the concentration ratio of the GDC to the silver precursor (Table 9, SDC-5 and SDC-6), one could modulate the overall size of the satellites and generate more spheroidal silver satellites. Under these overall experimental conditions, some free silver particles were also formed in lower amount and could be easily removed by a centrifugation step due to their small size.

Protocol 18: Seeded growth of silver salt on GDC

A typical volume of the GDC suspension, obtained after a gold regrowth using a given concentration of GPS (Protocol 15) was added in a 5 mL flask. 500 μ L of silver salts (Ag_2SO_4 , 2 mM) were added into the medium and the mixture was homogenized. Subsequently 30 μ L of HCHO were added. Before the silver salt addition, a given volume of milliQ[®] water was added to the medium, in order to have a final volume of the reaction media of 1.5 mL (including the overall reactant volume). The mixture was left to stir overnight.

Table 9: Experimental conditions followed for the set SDC-4, SDC-5 and SDC-6.

Batch name	SDC-4	SDC-5	SDC-6
Number of the gold dodecahedra (ptcs)	$5.6 \cdot 10^9$	$2 \cdot 10^{10}$	$2.2 \cdot 10^{10}$
[Silver Precursor] mmol/L	0.7	0.7	0.7
V_{HCHO} (μ L)	30	30	30

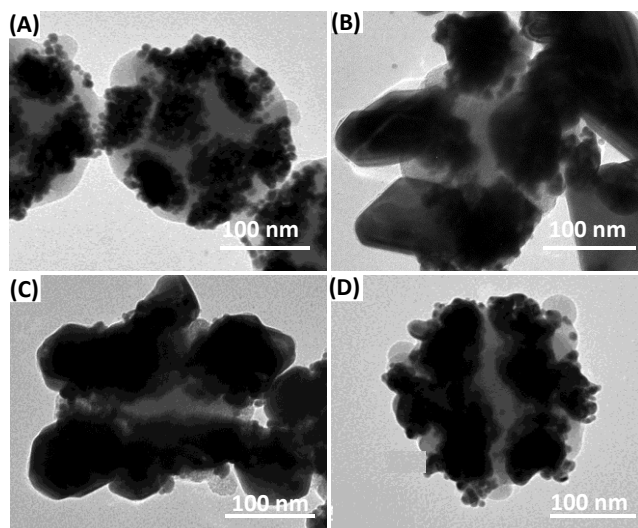


Figure 77: Representative TEM images of GDC before (A) and after silver deposition (B)-(D). The size of the silver satellite could be modulated by changing the concentration ratio of clusters to silver precursor (B) SDC-4 (C) SDC-5 (D) SDC-6 experimental conditions

The deposition of silver on the golden dimples was clearly evidenced by HR-TEM and STEM, and EDX analysis. Figure 78 highlights the silver deposition and its homogeneous repartition within each dimple. In the experimental conditions of the SDC-6 batch, the composition of the silver-gold satellites was 25/75.

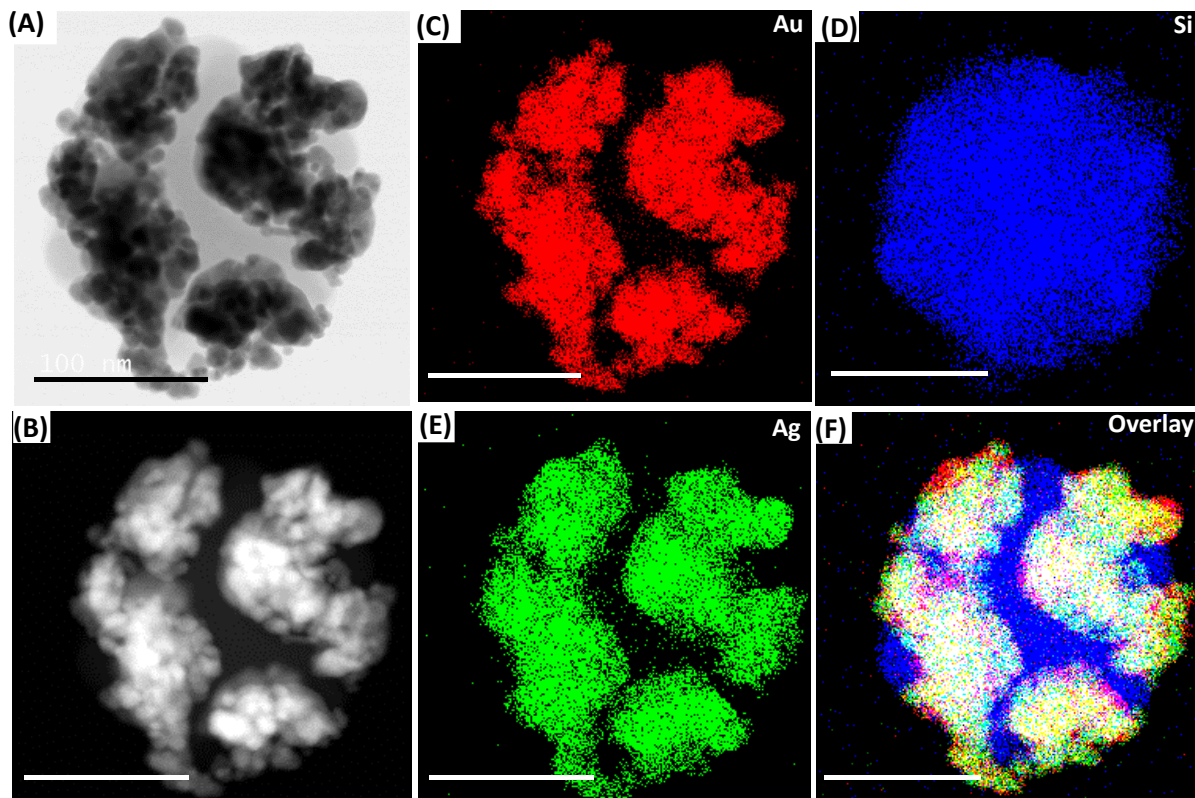


Figure 78: HR-TEM, STEM and EDX images (obtained by following the SDC-6 experimental conditions);
Scale bars: 100 nm

Figure 79 shows the UV-Vis extinction spectra of the as-synthesized GDC before and after the silver growth. The initial GDC have a surface plasmon resonance around 600 nm. After the silver deposition, the plasmon band shifted to 520 nm, indicating the effective silver deposition process on the gold seeds. This observation is in agreement with previous reported studies for bimetallic NPs richer in gold [4].

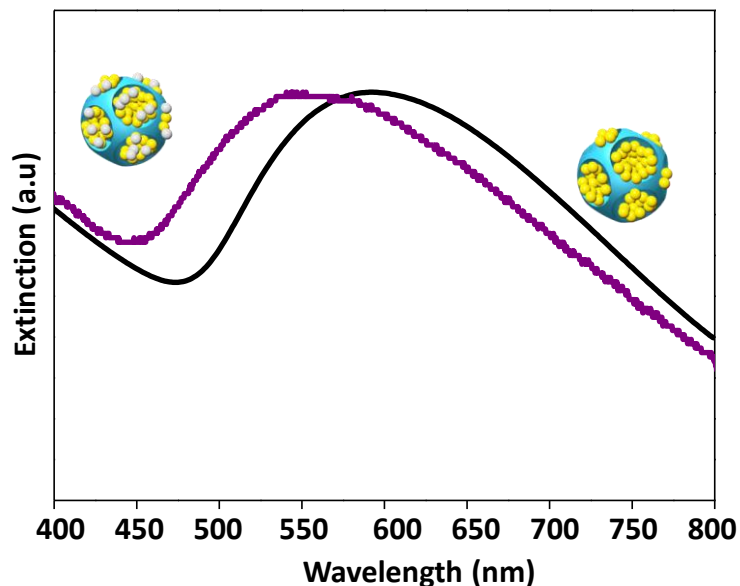


Figure 79: UV-Vis spectra of the GDC before (black curve) and after silver deposition (SDC-6; purple curve). The composition of the satellites was $\text{Au}_{75}\text{Ag}_{25}$.

In order to allow the diffusion between silver and gold in the heterostructure and to form alloyed satellites, the colloidal suspension of the SDC was annealed in ethylene glycol. However, a destabilization of the satellites was observed after the thermal treatment: the detachment of the gold and silver particles from the DDS and a mixture of DDS and plasmonic particles was formed.

3. Stage X: Control of the composition of the silver-gold satellites

The composition of the silver-gold satellites can be controlled by tuning the concentration of gold precursor during the synthesis of the GDC. The experimental conditions were adjusted in order to promote the silver deposition in the dimples (Table 3). This is why the concentration ratio of the silica clusters to the silver precursor varied from one batch to another one. For example, the preliminary synthesis of the GDC with 0.5 mM of GPS gave, after the silver deposition, $\text{Au}_{50}\text{Ag}_{50}$ nanostructures (SDC-7 experimental conditions).

Table 10: Experimental conditions followed for the batches SDC-7 and SDC-8.

Batch name	SDC-7	SDC-8
Number of the gold dodecahedra (ptcs)	$1.4 \cdot 10^{10}$	$5.6 \cdot 10^9$
[Silver Precursor] mmol/L	0.7	0.7
V_{HCHO} (μL)	30	30

Figure 80 and Figure 81 show images of the GDC, before and after the silver growth performed under the experimental conditions SDC-7. The deposition of silver is homogeneous into the golden dimples. The typical dimension is 82 nm for the satellites and 13 nm for the in-between satellites gap.

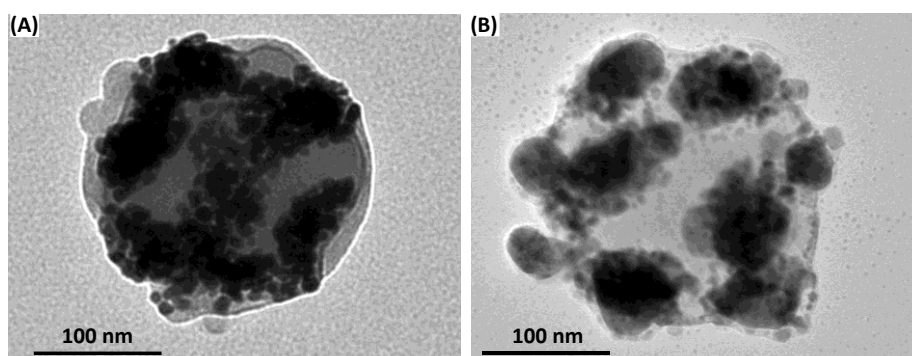


Figure 80: TEM images of the GDC: (A) before and (B) after the silver deposition (SDC-7 experimental conditions).

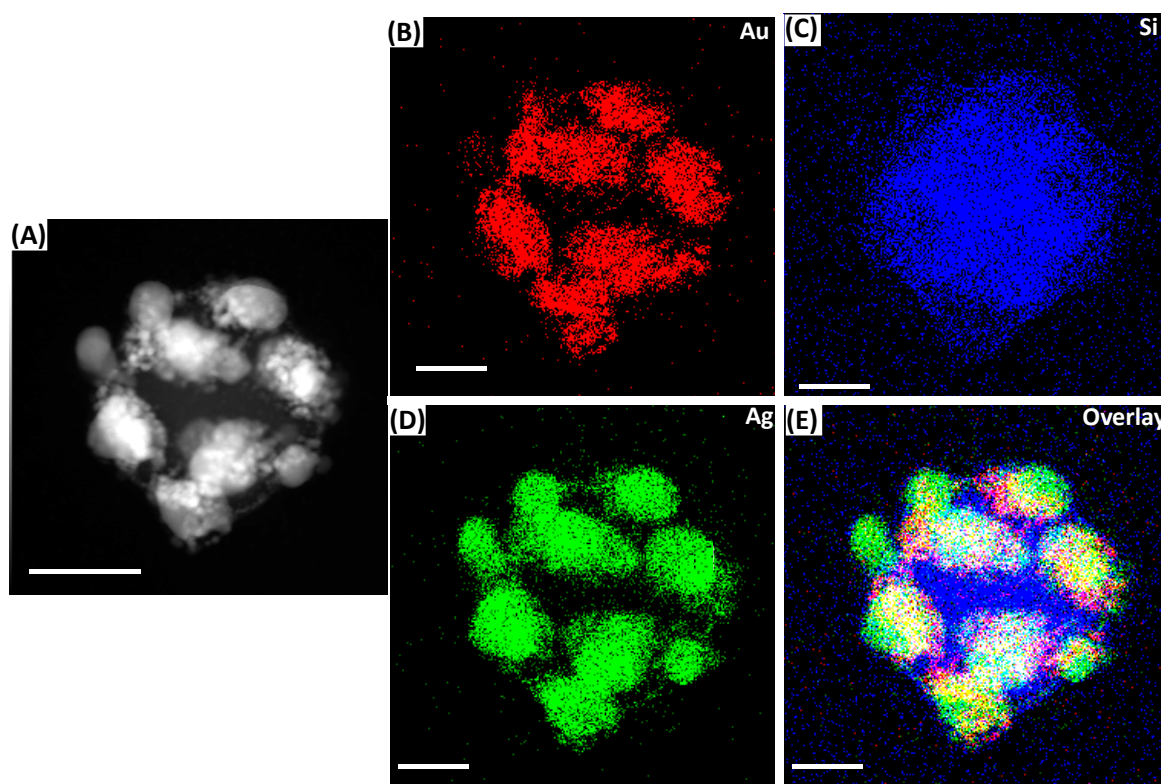


Figure 81: STEM and EDX images of the $\text{Au}_{50}\text{Ag}_{50}$ dodecahedral clusters (SDC-7). Scale bars: 100 nm

For lower concentration of gold precursor during the growth process of silver, the silver-gold satellites showed significantly different features. In a typical synthesis, the concentration of gold in the dimples were reduced, using 0.3 mM of GPS (Protocol 15). Silver-gold satellites were grown using SDC-8 experimental conditions (Table 10), the satellites hanged

over the dimples. The deposition of silver onto GDC synthesized using smaller GPS concentration, clearly resulted in anisotropic satellites (Figure 82).

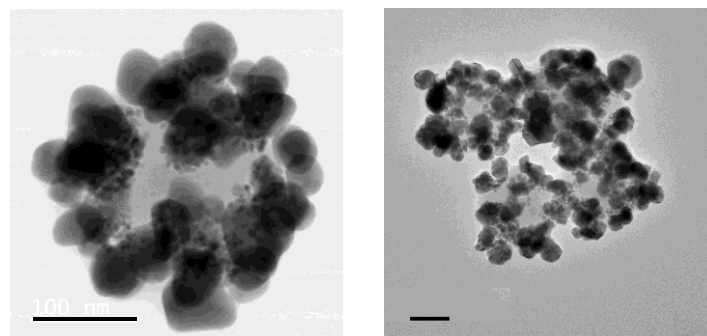
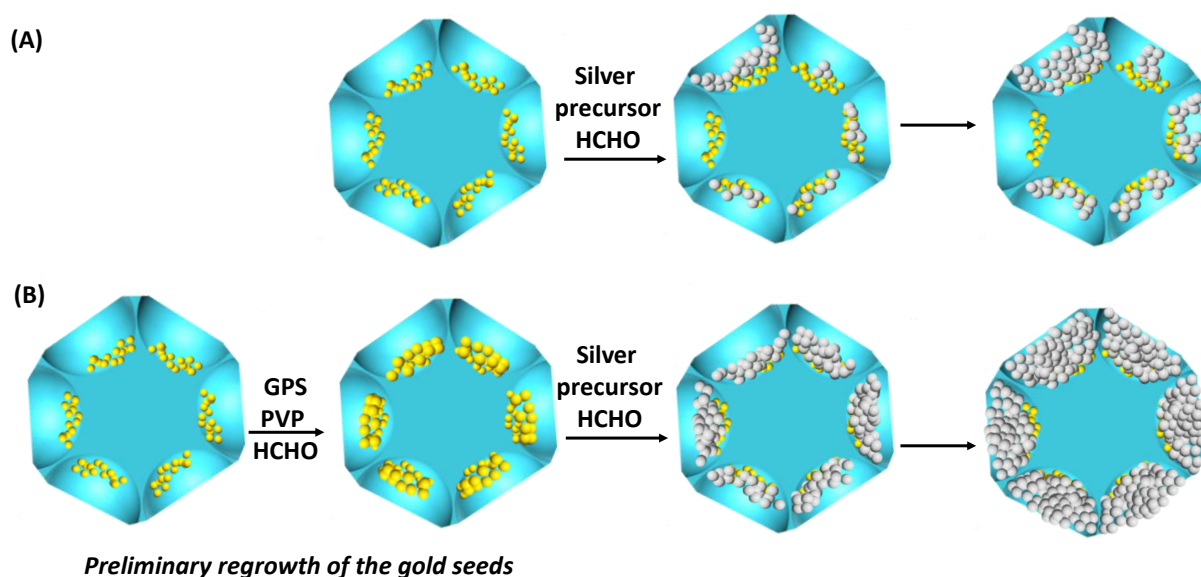


Figure 82: HR-TEM of the batch SDC-8. (Scale bars: 100 nm).

These overall experiments revealed that the size and the amount of gold particles was the key parameter for confining the silver growth within the dimples. A large amount of gold seeds may lead to a fast reduction and deposition of the Ag and a low amount of free Ag NPs (Scheme 12B). With low amount of gold seeds, the reduction rate of silver may be greatly reduced. Consequently, the deposition of silver on the dimples may occur in an inhomogeneous way and a lot of silver may be lost (Scheme 12A).



Scheme 12: Sketch illustrating the silver deposition onto golden dimples: (A) on tiny gold seeds and (B) on larger ones

Subsequently, the SDC-7 batch was characterized by UV-visible extinction spectroscopy. Its spectrum highlights one peak at 550 nm and another one in the blue region of the spectra at 425 nm, confirming the presence of both gold and silver.

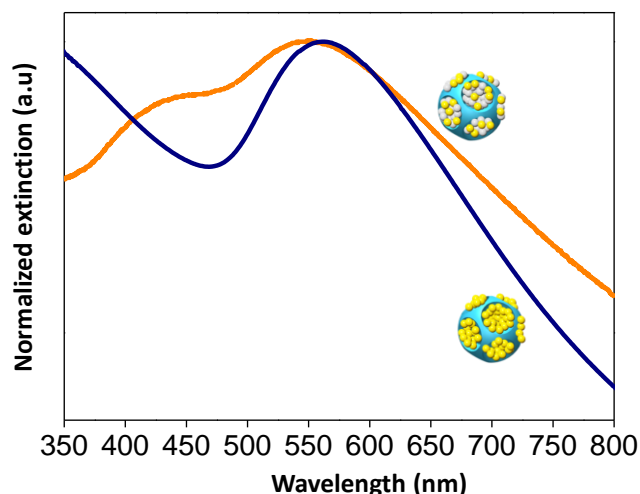


Figure 83: Extinction spectra of the GDC: before (blue curve) and after silver regrowth (batch SDC-7; orange curve).

4. Investigation of the magnetic and electric responses of the silver dodecahedral clusters from static light scattering

The scattering properties of the SDC were studied by polarization resolved static light scattering. Figure 85 illustrates the scattering intensity $A_{//} / A_{\perp}$ for the $Ag_{25}Au_{75}$ and $Ag_{50}Au_{50}$ samples. Each sample exhibits a broad maximum in the visible range. The maximum increases and blue-shift upon increasing the amount of silver. The data measured on silver raspberries of similar size are also shown in Figure 84 for comparison. The scattering intensity $A_{//} / A_{\perp}$ for SDC-7 is found 1.4 times higher than the one measured for silver raspberries. Furthermore, the scattering efficiency was 2.5 times higher than the value measured from GDC-6 of similar morphology (Figure 70A).

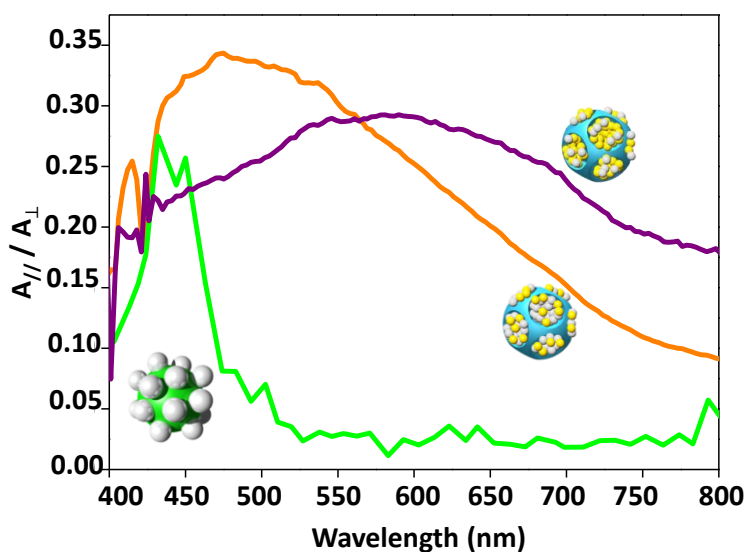


Figure 84: Comparison of the scattering efficiency of silver raspberries [2] (green curve) and SDC clusters of different compositions $\text{Ag}_{25}\text{Au}_{75}$ (SDC-6; purple curve) and $\text{Ag}_{50}\text{Au}_{50}$ (SDC-7; orange curve).

These results confirm that changing gold for silver reduces the optical losses and strongly enhances the scattering efficiencies of the plasmonic raspberries. The observed optical properties were compared to numerical investigations, using GMM theory and taking into account the SDC characteristics (size and composition) as an input. The simulated data (Figure 85) are consistent with the experimental ones. The clusters with the characteristics corresponding to the experimental conditions SD-6 and SD-7 have a strong scattering efficiency between 500 nm and 650 nm, and between 450 nm and 700 nm, respectively.

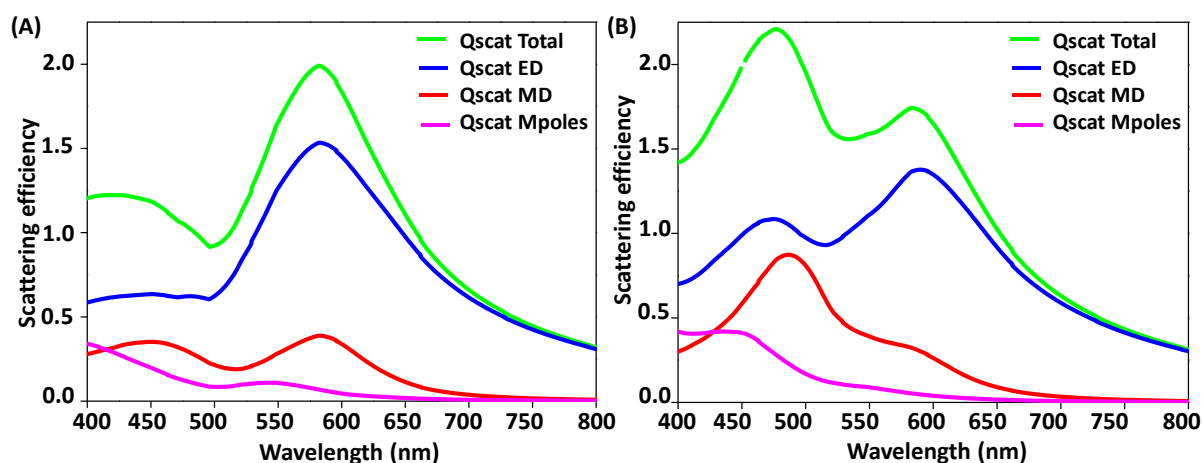


Figure 85: Numerical simulation of the scattering efficiencies of the SDC with the characteristic corresponding to the experimental conditions: (A) SDC-6 and (B) SDC-7.

5. Conclusion

In this chapter, we have developed an efficient protocol for the fabrication of SDC. The strategy is based on the deposition of silver onto golden dimpled clusters. This strategy enables to tune the $\text{Ag}_x\text{Au}_{1-x}$ composition of the satellites by adjusting the concentration ratio between the gold dodecahedral clusters to the silver precursor. The SDC can be produced on a large scale.

These clusters exhibit unique plasmonic properties. The scattering efficiencies of the $\text{Ag}_{25}\text{Au}_{75}$ and $\text{Ag}_{50}\text{Au}_{50}$ dodecahedra were investigated by SLS measurements and compared with simulations. The results confirmed that SDC exhibit a magnetic response stronger (35%) than the gold based ones (14%). Moreover, the magnetic to electric polarization ratio

measured on these new silver and gold clusters is higher than the one measured on plasmonic raspberries with silver satellites of similar size (27%).

6. References

- [1] V. Ponsinet, P. Barois, S. M. Gali, P. Richetti, J. B. Salmon, A. Vallecchi, M. Albani, A. Le Beulze, S. Gomez-Grana, E. Duguet, S. Mornet, and M. Treguer-Delapierre, “Resonant isotropic optical magnetism of plasmonic nanoclusters in visible light,” *Phys. Rev. B*, vol. 92, no. 22, p. 220414, 2015.
- [2] S. Gomez-Grana, A. Le Beulze, M. Treguer-Delapierre, S. Mornet, E. Duguet, E. Grana, E. Cloutet, G. Hadziioannou, J. Leng, J.-B. Salmon, V. G. Kravets, A. N. Grigorenko, N. A. Peyyety, V. Ponsinet, P. Richetti, A. Baron, D. Torrent, and P. Barois, “Hierarchical self-assembly of a bulk metamaterial enables isotropic magnetic permeability at optical frequencies,” *Mater. Horizons*, vol. 3, no. 6, pp. 596–601, 2016.
- [3] J. B. Jackson and N. J. Halas, “Silver nanoshells: Variations in morphologies and optical properties,” *J. Phys. Chem. B*, vol. 105, no. 14, pp. 2743–2746, 2001.
- [4] K. Mallik, M. Mandal, N. Pradhan, and T. Pal, “Seed mediated formation of bimetallic nanoparticles by UV irradiation: A photochemical approach for the preparation of ‘core–shell’ type structures,” *Nano Lett.*, vol. 1, no. 6, pp. 319–322, 2001.

Conclusions
and future work

The main objective of this thesis was to fabricate new metallodielectric nanoresonators, with the aim to optimize the magnetic response of raspberry-like nanoparticles in the visible range [1,2]. Guided by numerical simulations we focused our work on the design of Platonic solids made of a silica core and surrounded by twelve plasmonic satellites. To fulfill this goal, we used functional silica particles with 12 dimples as a scaffold and we developed a seeded growth approach to grow gold or silver at the bottom of the silica dimples. In the first chapter, an extensive state-of-the-art confirmed that our strategy is original.

In the second chapter, we more deeply investigated the multi-step synthesis of the dodecapods-like silica/PS clusters proposed by Désert *et al.* [3]. We studied the influence of the SDS-to-NP30 mass ratio, the total concentration of the surfactant, and the styrene concentration. We were able to increase the morphology yield of dodecapods up to 75%. However, several types of by-products remained in the dodecapod batches such as multi-silica clusters and clusters with less than twelve PS satellites. A purification step by gradient density centrifugation could be envisaged, but it would be very tricky because of the low contrast of apparent density between the targeted dodecapods and the by-products. Subsequently, functionalized DDS clusters were synthesized by the regrowth of the silica core, the subsequent development of the dimples by dissolution of the PS satellites and the specific functionalization of the residual PS macromolecules.

In the third chapter, the gold dodecapods were synthesized by a seed-mediated growth approach. The satellite size and the in-between gap were controlled by the amount of the gold plating solution used during the growth stages. We observed that some dissolution of the silica templates could occur during the gold growth step. This phenomenon seemed to be dependent on the age of the gold plating solution. We suppose that such dissolution arises from the presence of counter-ions in the medium, which may interact directly with the silica oxide surface as a coordinated complex, disturbing the surface structures and leading to silica dissolution. [4] We found the experimental conditions to confine the gold growth strictly within the dimples. An additional densification step of the gold aggregates by thermal annealing treatment in ethylene glycol was implemented. The bottom-up approach developed allowed to synthesize nano-clusters made of 12 gold patches located at the center of the faces of a dodecahedron.

In the fourth chapter, the synthesis of gold dodecapods was extended to silver-gold dodecahedral ones. As a first attempt, gold seeds were previously adsorbed onto the

functional silica templates and silver nitrate was used as a precursor in order to promote the growth of silver. Several parameters were investigated: the pH of the solution, the reducing agent concentration, and the silica particles to silver precursor ratio. However, those studies failed as a regioselective deposition of silver was not observed specifically on the dimples. Silver-gold dodecahedral clusters were successfully obtained after: (i) a preliminary growth stage of gold yielding to increase the gold aggregates size; (ii) changing the silver precursor from silver nitrate to silver sulfate (iii) adjusting the appropriate concentration ratio of the dimpled-silica nanoparticles to silver precursor. By tuning the concentration in the starting gold dodecapods, the composition of the satellites can be controlled. Clusters with satellites made of 25 % and 50 % of silver were synthesized.

The magnetic response of the as-obtained plasmonic dodecahedral clusters were investigated by polarized light scattering spectroscopy. The magnetism observed arises from circulating currents that come from the angular momentum of the orbiting electron. This magnetism response originates from second-order spatial dispersion and is only valid in the case of divergent-free solutions (when the divergence of the electric field is null). The GDC clusters exhibited a magnetic response three times higher than the value measure on gold raspberries of similar size made of a large number of metallic satellites randomly distributed around the dielectric core. We observed that the densification of the gold aggregates confined the dimples into homogeneous domains was an important step and led to a drastic increase of the magnetic response comparing to the non-condensed ones. The magnetic resonance of the condensed system converges toward that of the ideal dodecapod. Thus, by precisely controlling the number, the size, the position of the satellites, and their in-between gap we were able to optimize the magnetic response of metallodielectric nanoresonators. Changing the composition of the GDC toward silver-gold ones allowed to reduce the optical losses and strongly enhance the magnetic response of the dodecapods. The magnetic response of the silver-gold dodecahedral cluster was optimized for clusters made of $\text{Ag}_{50}\text{Au}_{50}$ satellites. These overall results validate the superiority of the dodecapod structure over the disordered distribution of a large number of satellites in the raspberry model. The well-defined positions of the satellites offer a better control of the collective electromagnetic coupling which determines the strength of the circular plasmonic currents generating the magnetization.

Since the bottom-up approach developed here allowed the synthesis of the plasmonic dodecahedral clusters in high yield, the fabrication of optical functional devices of large area was implemented. The fabrication of 2D metasurfaces and 3D materials by the assembly of

the plasmonic dodecahedral clusters were performed in collaboration with G. Drisko from ICMCB and the J. Leng and coworkers from the Laboratory of Future (LOF, Pessac), respectively.

Attempts to fabricate a 2D homogeneous metasurface were performed by the dip-coating technique, which is based on the vertical dipping of a substrate into a suspension at a constant speed. We investigated the influence of the concentration of the GDC suspension, the nature of the solvent, the withdrawal speed, and temperature, on the packing density of the nanoresonators and the thickness of the deposited layer. A monolayer of the GDC was obtained (Figure 86), even if the packing density of the nanoclusters needs to be further improved.

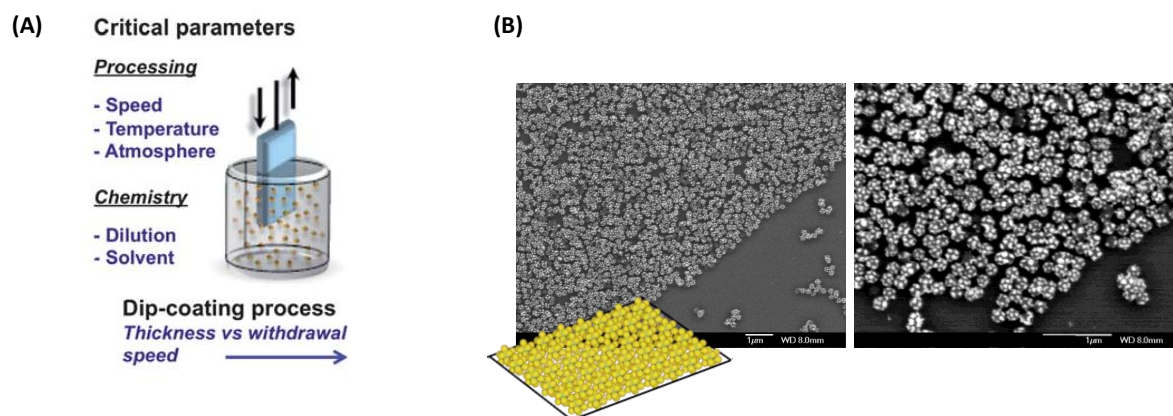


Figure 86: (A) Sketch of a dip coating setup[5]; (B) Typical SEM images of the fabricated GDC metasurface.

The fabrication of a dense 3D material was achieved by microfluidic assisted evaporation of gold dodecapods. This technique allows the concentration of a colloidal suspension into micro-channels to shape-up a three-dimensional material made of densely packed nanoparticles [6]. During the process, the colloidal suspension flowed in a micro-channel. The selective permeability of an integrated membrane induced the extraction of the solvent from the micro-channel (Figure 87A). Figure 87B shows a 3D material obtained from gold dodecapods.

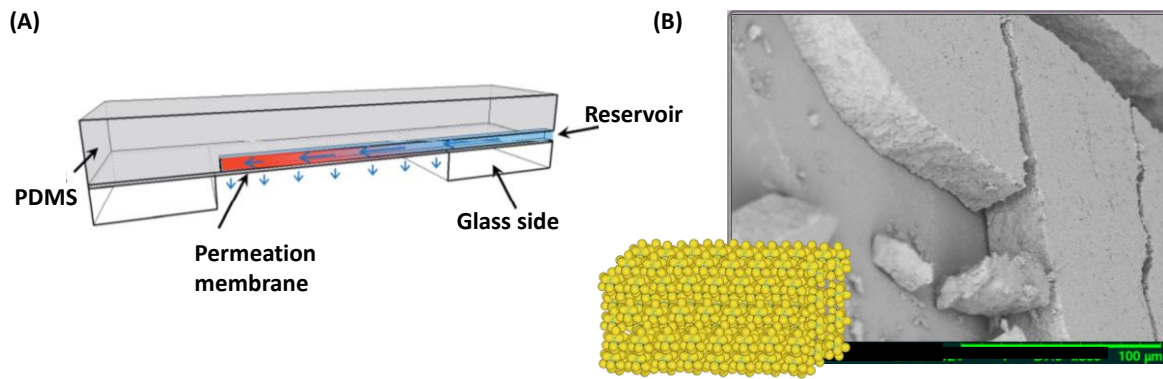


Figure 87: (A) Sketch of the microfluidic evaporation setup; (B) Typical SEM image of the bulk material based on GDC.

Their optical properties, analyzed by variable-angle spectroscopic ellipsometry, are currently in progress. The first investigations evidenced the nonconventional magnetic response of these materials (*i.e.* relative magnetic permeability lower than one). But, the comprehensive study of the electromagnetic processes at the origin of their optical properties is still under investigation.

To finish with, the use of highly symmetrical plasmonic clusters as building blocks for engineering materials that exhibit artificial optical magnetism in the visible range has been validated in this study. They have shown to be promising in terms of performances but they still suffer from high level of losses in visible light and IR range. This problem can be overcome by changing the plasmonic clusters by silicon nanospheres or copper oxide ones with a well-controlled size and crystallinity. Numerical simulations reported that crystalline silicon nanoresonators can be highly efficient (10 times higher than the plasmonic clusters) [7]. Unfortunately, the synthesis of silicon nanospheres of well-controlled size is challenging due to its propensity to oxidize to silica.

References

- [1] V. Ponsinet, P. Barois, S. M. Gali, P. Richetti, J. B. Salmon, A. Vallecchi, M. Albani, A. Le Beulze, S. Gomez-Grana, E. Duguet, S. Mornet, and M. Treguer-Delapierre, "Resonant isotropic optical magnetism of plasmonic nanoclusters in visible light," *Phys. Rev. B*, vol. 92, no. 22, p. 220414, 2015.
- [2] S. Gomez-Grana, A. Le Beulze, M. Treguer-Delapierre, S. Mornet, E. Duguet, E. Grana, E. Cloutet, G. Hadziioannou, J. Leng, J.-B. Salmon, V. G. Kravets, A. N. Grigorenko, N. A. Peyyety, V. Ponsinet, P. Richetti, A. Baron, D. Torrent, and P. Barois, "Hierarchical self-assembly of a bulk metamaterial enables isotropic magnetic permeability at optical frequencies," *Mater. Horizons*, vol. 3, no. 6, pp. 596–601, 2016.

- [3] A. Désert, J. Morele, J.-C. Taveau, O. Lambert, M. Lansalot, E. Bourgeat-Lami, A. Thill, O. Spalla, L. Belloni, S. Ravaine, and E. Duguet, “Multipod-like silica/polystyrene clusters,” *Nanoscale*, vol. 8, no. 10, pp. 5454–5469, 2016.
- [4] P. M. Dove and D. A. Crerar, “Kinetics of quartz dissolution in electrolyte solutions using a hydrothermal mixed flow reactor,” *Geochim. Cosmochim. Acta*, vol. 54, no. 4, pp. 955–969, 1990.
- [5] D. Grosso, “How to exploit the full potential of the dip-coating process to better control film formation,” *J. Mater. Chem.*, vol. 21, no. 43, pp. 17033–17038, 2011.
- [6] J. Angly, A. Iazzolino, J.-B. Salmon, J. Leng, S. P. Chandran, V. Ponsinet, A. Désert, A. Le Beulze, S. Mornet, M. Tréguer-Delapierre, and M. A. Correa-Duarte, “Microfluidic-induced growth and shape-up of three-dimensional extended arrays of densely packed nanoparticles,” *ACS Nano*, vol. 7, no. 8, pp. 6465–6477, 2013.
- [7] M. L. De Marco, S. Semlali, B. A. Korgel, P. Barois, G. L. Drisko, and C. Aymonier, “Silicon-based dielectric metamaterials: Focus on the current synthetic challenges,” *Angew. Chemie Int. Ed.*, vol. 57, no. 17, pp. 4478–4498, 2017.

Titre : Synthèse et design de nanorésonateurs optiques actifs dans le visible

Résumé : L'étude et la réalisation de métamatériaux auto-assemblés possédant une réponse magnétique aux fréquences optiques font l'objet d'un champ de recherche très actif depuis plusieurs années. De nombreux calculs théoriques ont prédit qu'un arrangement dense de briques élémentaires plasmoniques, « les méta-atomes », conduirait à des matériaux à indice négatif actifs dans le domaine du visible. Il a été démontré qu'un nano-objet ayant un cœur de silice décoré de 12 nanoparticules d'or sphériques permettrait d'optimiser le phénomène de magnétisme optique. Ma thèse repose sur l'élaboration de ces objets à partir de particules colloïdales, parfaitement symétriques, constituées d'un cœur de silice et 12 nodules de polystyrène. Ces nodules de PS pouvant être éliminés ultérieurement par dissolution. Ces objets ont permis de fabriquer des particules de silices décorées d'un nombre précis de « patches » ou de « fossettes ». Ces objets ont été formés en grande quantité. Nous sommes parvenus à rendre les cavités de surface des particules à fossettes collantes pour des germes d'or de 2-3 nm de diamètre et initier leur croissance. Les mesures de propriétés optiques de ces dodécapodes dorés ont reflété le couplage intense existant entre les nanoparticules plasmoniques autour du cœur diélectrique. La possibilité de faire croître de l'argent à la surface des germes d'or permet de générer des nanorésonateurs avec des modes magnétiques optiques encore plus intenses que ceux observés pour les systèmes à base d'or.

Mots clés : Nanorésonateurs, synthèse colloïdale, métamatériaux, plasmonique

Title : Synthesis and design of optical nanoresonators for the visible wavelengths

Abstract: Over the last decade, the field of self-assembled metamaterials exhibiting unusual properties such as a magnetic response in the visible range represents a challenging and attracting area. Many simulations reported that a dense arrangement of specific plasmonic sub-units called “meta-atoms”, may lead to a material with a negative refractive index. It was reported by computational modelling that a dodecapod clusters made of a central dielectric core and surrounded by a controlled number of satellites (12 satellites, here) with a specific size can exhibited some interesting properties. Here, the purpose was to fabricate such clusters from colloidal particles, which are perfectly symmetrical, made of a silica core and 12 polystyrene nodules. Subsequently, those polystyrene nodules can be dissolved to get silica particles with a specific number of “patches” or “dimples”. Those objects were synthesized in a large quantity. We were able to make those dimples sticky to tiny gold seed of 2-3 nm size and to grow then for a specific size. Optical measurements reported the strong magnetic coupling in-between the plasmonic nanoparticles around the dielectric core. We also reported that growing silver on tiny gold seeds generates stronger magnetic responses than those observed from gold clusters.

Keywords: Nanoresonators, colloidal synthesis, metamaterial, plasmonic;